A Multifaceted Analysis of Diurnal Streamflow Patterns Through the Application of Advanced Analytical Tools

A thesis submitted in fulfillment of the partial requirements for the degree

of

Doctor of Philosophy in Engineering

by

Muhammad Waqas Sarwar

Division of Health, Engineering & Computing and Science

THE UNIVERSITY OF
WAIKATO
Te Whare Wānanga o Waikato

2023

Abstract

Understanding the complex dynamics of water flow within a catchment is fundamental to effective water resource management. This understanding involves robust knowledge of the catchment's hydrological and physiographical features. It requires a profound grasp of the spatiotemporal variability in a catchment's climatic and hydrological patterns. Within this context, this thesis started with a comprehensive review of the historical and current literature on diurnal fluctuations in groundwater. The review touched upon several different aspects of the phenomenon, ranging from discussing the mechanisms of the origin of these signals, their role in the catchment's water balance, their link with groundwater and with the transpiration activities of the vegetation, and in the end, the importance of studying these catchments in revealing characteristics of a catchment.

Potential gaps in the analysis of diurnal fluctuations are identified by exploring the literature., which motivated the compilation of this thesis. Firstly, the relationship between diurnal fluctuation and the potential evapotranspiration of riparian plants is investigated in relation to its effect on catchment reservoir storage. A novel method of estimating evapotranspiration (ET) rates is devised by establishing a relationship between diurnal streamflow changes and the catchment's riparian source area. The method reasonably estimated riparian evapotranspiration (ET) and linked the riparian area's dynamics with the diurnal patterns in stream flow by assuming a linear relationship between saturated riparian reservoirs and outflow. This analysis provided a much-needed understanding of the behaviour of the diurnal signals in a catchment and its relationship with the physical features of the catchment.

Further, this analysis deeply studied the concept of time delay associated with the transpiration activities of riparian plants and catchments' response regarding diurnal fluctuation. Additionally, the

seasonal evolution of ET estimates and the time lag revealed the tight coupling between stream response and active vegetation zones, with more significant and rapid fluctuation in colder months than warmer ones. In conclusion, the method provided an elaborate understanding of the complex interplay between riparian zones, groundwater dynamics, and streamflow patterns, contributing to a more profound understanding of catchment hydrology.

Another significant thesis objective was to develop advanced automated techniques for detecting and analysing diurnal fluctuations to provide fast and reliable observations of diurnal fluctuations from a large dataset. Manually identifying this scarce phenomenon in an extensive multi-year dataset is time-consuming and one of the biggest reasons for minimal, large-sample studies concerning diurnal streamflow fluctuations. This is addressed by forming an automated process of diurnal fluctuation extraction with the application of the wavelet transform.

The capabilities of both types of wavelet transformation, the discrete wavelet transform (DWT) and continuous wavelet transform (CWT) are tested to reveal time-frequency information of diurnal signals. A detailed workflow is developed to choose the best wavelet for detrending a streamflow series to obtain diurnal fluctuation. The detrending performance of the DWT process is compared against the traditional time-based detrending methods like the moving average. It confirms the superiority of wavelet transform in optimal detrending of observed streamflow data series. The CWT presented many different plots and revealed exciting features in the diurnal patterns in streamflow. The CWT information is then used to develop an algorithm for extracting diurnal episodes from extensive streamflow records. The extraction process captured an adequate number of diurnal episodes, which matched well with the manual identifications. Overall, the automated technique addressed the limitations posed by manual identification and contributed significantly to the advancement of time-frequency dynamics of diurnal fluctuations.

Finally, with the knowledge of diurnal fluctuation gained in the first research objective and with the capabilities of the wavelet transform, a large sample study is carried out using streamflow records from different New Zealand catchments. Various dataset sources from streamflow records, snow

cover maps, and digital elevation rasters are used to calculate different catchment characteristics. The analysis showed that characteristics like catchment shape and size strongly correlate with diurnal amplitude. The diurnal lag also showed patterns of change with the catchment parameters. It is revealed that the correlation between catchment size and diurnal amplitude becomes weaker in larger catchments due to the diverse and heterogeneous nature of environmental processes within these regions.

This research significantly contributes to a deeper understanding of the temporal patterns of streamflow, providing valuable insights for hydrological modeling and water resource management. By integrating field observations, advanced analytical methods, and regional context, this work advances the understanding of diurnal streamflow dynamics.

Acknowledgments

First and foremost, I extend my sincere gratitude to Almighty Allah, whose blessings and guidance have been the foundation of my journey. Without His help, none of this would have been possible.

I am deeply thankful to my wife, parents, and siblings whose unwavering support and constant prayers have strengthened me. Their encouragement propelled me forward during the challenging phases of my research, and their belief in my capabilities fueled my determination.

Secondly, upon submitting this thesis, I thank my supervisors, Dr Ali Shokri and Associate Professor David Campbell. Their consistent support, excellent supervision, and valuable insights have shaped my academic endeavours. From the inception of my research to the finalization of my thesis, their expertise has been a guiding light.

I am also grateful to the School of Engineering, Division of Health, Engineering, Computing and Science, and the University of Waikato for providing me with a supportive and constructive environment to do the research.

Dedication

I dedicate this thesis to my wife and my daughter, Eisha. I cannot express enough gratitude to my wife for enduring this research period with me. She single-handedly took on the responsibility of caring for our sick daughter. Despite all the tribulations, my daughter's smiles were the biggest encouragement that motivated me to complete this work.

Table of Contents

List of Figures

List of Tables

Chapter 1. Introduction

Understanding the complex dynamics of water flows within a catchment is fundamental to effective water resource management. This understanding involves robust knowledge of the catchment features and different climatic and hydrological patterns within the catchment. Analysing the spatiotemporal variability in the hydrological patterns and their climatic drivers can uncover critical insights into the behaviour of the catchment (H. K. McMillan et al., 2022).

Climate plays a crucial role in shaping hydrological behaviours, as changes in temperature and precipitation patterns directly influence the water cycle. Altered rainfall resulting from these climate shifts can disrupt the water balance of a catchment in several ways, affecting runoff, groundwater recharge, soil moisture, and ecosystems. (Chiew et al., 1995). Similarly, solar radiation directly controls the amount of water loss from the Earth's surface through evaporation and transpiration, affecting the soil moisture patterns in the ground and limiting the water availability to plants (Oliveira et al., 2011; Venturini et al., 2022).

Furthermore, human activities such as deforestation, urbanization, and agriculture can alter natural hydrological patterns, leading to water availability and quality changes. Changes in the plant cover on hillslopes can cause a change in the groundwater abstraction and affect streamflow patterns (Bren, 1997). Converting wasteland for agriculture and construction of dams can lead to reduced streamflow (Bibi et al., 2023). Urbanization can further change flow regimes by shortening groundwater travel times and reducing baseflow discharge (Schilling et al., 2012).

Hydrological patterns like precipitation, streamflow, and groundwater can serve as a valuable proxy for assessing the impact of both natural and human activities on catchment hydrology (Kirchner, 2009; McMillan et al., 2022), ultimately assisting in assessing the overall health and resilience of catchment hydrology under various conditions.

Diurnal fluctuations in groundwater and streamflow are critical hydrologic patterns that can reveal essential information on how catchment water systems may respond to daily and seasonal changes in environmental conditions (Gribovszki, Kalicz, Szilágyi, et al., 2008; Széles et al., 2018). Diurnal fluctuations in groundwater and streamflow refer to the daily variations in the groundwater table and streamflow discharge, respectively (Troxell, 1936; White, 1932). These fluctuations often exhibit a distinct diurnal pattern, including regular rising and falling flow rates over a day (Lundquist & Cayan, 2002).

Diurnal fluctuations in groundwater table and streamflow can provide valuable insight into the low-flow hydrologic processes of a catchment. For example, analysing the streamflow patterns during low-flow periods can be crucial for assessing the performance of water systems under drought conditions (Koch et al., 2018). The analysis can also help determine streamflow increases or decreases for water management decisions (Lundquist & Cayan, 2002). This underscores the importance of a more detailed study of diurnal cycles and their drivers, including snow melt, hillslope, and stream hydrology (Woelber et al., 2018).

1.1 Factors Influencing Diurnal Flow Cycles:

In order to fully understand the diurnal river flow fluctuation phenomenon, it is essential to consider the different environmental factors and mechanisms that play a role in the generation, propagation, and modulation of these daily hydrological patterns.

1.1.1 Evapotranspiration:

Evapotranspiration (ET) refers to the combined processes of water evaporation from the land surface and plant transpiration. ET constitutes a significant component of the overall water loss to the atmosphere, influencing the water balance in ecosystems and agricultural fields. ET rates fluctuate throughout the day, peaking during daylight hours and decreasing at night. These fluctuations in ET directly control the daily variations in the soil moisture. Soil moisture withdrawals through ET influence water availability for vegetation and produce daily or diurnal patterns in the groundwater and streamflow(Gribovszki et al., 2010).

Several studies have linked ET as the primary cause of diurnal fluctuations in groundwater levels and baseflow (Bond et al., 2002; Gribovszki, Kalicz, Szilágyi et al., 2008; Troxell, 1936; White, 1932), particularly in small-headwater catchments. Plants within a catchment, particularly along the riparian corridors immediately adjacent to the river, have root systems that extend into the capillary fringe zone. This allows them to extract groundwater and, in certain instances, draw water directly from the stream (Bond et al., 2002; Troxell, 1936). Černohous & Šach, (2008) observed that in a small experimental forest catchment, during rainless periods, the decrease in streamflow during the daytime compared to nighttime was primarily attributed to forest evapotranspiration.

The amount of water withdrawn by ET is a function of the type and density of vegetation, the depth of the groundwater, and prevailing atmospheric conditions (Shrestha, 2021; Van Camp et al., 2016). ET-induced diurnal signals show a distinct asymmetric pattern, with a decline in the daily streamflow during the day and a gradual rise during the night (Bren, 1997; Lundquist & Cayan, 2002). Moreover, the ET-induced fluctuations have been reported to vary between seasons, depending upon the amount of solar radiation, and tend to disappear at the onset of winter (Széles et al., 2018).

1.1.2 Snowmelt:

Snowmelt contributes to a substantial percentage of annual streamflow in mountainous alpine catchments. Snowmelt is also reported as a causal factor for diurnal fluctuations in streamflow (Kirchner et al., 2020). Snowmelt-dominated rivers exhibit sharp rises and gradual declines in discharge each day during the spring melt season (J. D. Lundquist & Cayan, 2002). Caine (1992) demonstrated that the amplitude and phase of the diurnal streamflow cycle in an alpine basin varied with the reduction in snow cover depth throughout the summer. Mutzner et al. (2015) observed a transition from a snowmelt-dominated diurnal cycle to an evapotranspiration-dominated cycle in an alpine catchment, suggesting that different processes can influence diurnal streamflow patterns.

1.1.3 Water Viscosity:

The changes in streamflow viscosity can also affect streamflow patterns. Water viscosity is influenced by factors such as temperature (Cuevas et al., 2010). In forested headwater catchments, the water temperature in the riparian zone can fluctuate throughout the day, leading to changes in viscosity (Schwab et al., 2016). Viscosity-driven diurnal variations are most noticeable when stream discharge is low, or the hydraulic radius is small, and (b) when the streamwater and the streambed undergo significant temperature fluctuations, especially in unshaded channels (J. D. Lundquist & Cayan, 2002). The daily viscosity-driven streamwater cycle exhibits a hydrograph shape similar to the asymmetric pattern induced by riparian ET, such that a gradual rise follows a rapid decrease in the morning and evening. However, in forested catchments with ample shading for the stream, the viscosity-driven diurnal fluctuation of the stream temperature is generally so slight that the mentioned effect is practically undetectable (Czikowsky & Fitzjarrald, 2004).

1.1.4 Human Activities:

Human activities such as water extraction for irrigation, industrial use, and domestic consumption can significantly impact diurnal flow cycles. During the daytime, when water demand is typically higher, substantial amounts of water are withdrawn from rivers and groundwater reserves. This

increased demand leads to noticeable reductions in streamflow and groundwater levels. For instance, agricultural practices often involve intensive irrigation during daylight hours, which can lead to marked diurnal fluctuations in local water bodies (Bouwer, 2002). In urban areas, water use peaks in the morning and evening, corresponding with domestic activities such as bathing, cooking, and gardening, further contributing to diurnal variations in water levels (Shiklomanov, 2000).

In addition to direct water extraction, human-induced alterations such as dam operations and reservoir management also play a role in modulating diurnal flow patterns. Hydropower plants, for example, often release water during periods of high electricity demand, typically during the day, causing fluctuations in downstream flow (Morovati et al., 2024). Similarly, recreational activities like swimming, fishing, and boating can affect water bodies, particularly in regions where such activities are concentrated at specific times of the day. These human interventions can lead to flow patterns that are distinctly different from those driven by natural environmental factors alone.

1.1.5 Uncertainty in Flow Measurements:

Understanding and managing the uncertainty in flow measurements is critical in the study of diurnal fluctuations in streamflow due to evapotranspiration. Various sources, such as instrument precision, calibration error, and human-related factors, such as reading or recording mistakes, introduce significant uncertainty (Horner et al., 2018). Instrumentation errors, in particular, can induce false diurnal fluctuations or mask real ones, leading to inaccurate assessments of evapotranspiration. For example, malfunctioning or poorly calibrated equipment and transient errors like electronic noise can create artificial patterns in the data (Hamilton & Moore, 2012).

The cumulative effect of these errors can introduce significant uncertainty in the measured flow data, which can, in turn, affect the interpretation of streamflow patterns and the estimation of evapotranspiration rates (H. McMillan et al., 2017).

1.2 Problem Statement:

1.2.1 ET Estimation and Diurnal Fluctuation:

In hydrological engineering, accurate evapotranspiration (ET) estimation is essential for determining water budgets, particularly in arid and agricultural regions. Various meteorological factors, such as solar radiation, vapour pressure deficit, temperature, and wind speed, affect ET rates (Allen et al., 2011; Khanmohammadi et al., 2017). The tight co-dependence of ET with meteorological and environmental variables introduces spatiotemporal variability in ET estimates and makes them location-specific. This variability poses challenges in accurately measuring ET, especially when extrapolating data over large areas (Allen et al., 2011).

A significant concern associated with the current ET measurement and estimation techniques is their potential disconnect from the diverse hydrological processes occurring within a catchment. These techniques may not directly link ET and these processes, creating a gap in our understanding of catchment hydrology. The total moisture content of a catchment and atmospheric drivers are not isolated variables. Instead, they are interconnected with catchment vegetation productivity in a cause-effect relationship (K. Chen et al., 2023). Exploring ET in the context of catchment hydrology gives us a deep understanding of how ET affects water flows within a catchment and how various catchment features respond to changes in atmospheric water demand (Haslinger et al., 2014).

For instance, hydrological methods like weighing lysimeters can measure ET quite reasonably when placed in locations of homogeneous vegetation and soil stratification, such as crop fields (Fenner et al., 2019). However, lysimeters may be inappropriate for large watersheds of varying terrain, soil type, and vegetation, as they provide plot-specific ET measurements and require significant installation effort (Moorhead et al., 2019).

Plant physiology methods like the sap flow method have limitations when vegetation across a large area is highly varied and unevenly distributed in species. Grasslands and other small-stemmed plants are also unsuitable for the sap flow method (Santos et al., 2021). Similarly, the ET measurements

from the gas chamber method are highly localized and plant-specific, challenging their extrapolations to a broader area (Stannard, 1988).

Micrometeorological methods like the eddy covariance (EC) method directly quantify water vapor's mass flux between the Earth's surface and the atmosphere by measuring the turbulent eddy intensity and variations in water vapour density (Allen et al., 2011). EC provides an efficient way of measuring ET using various instruments and is one of the popular current methods used worldwide to measure ET (Consoli, 2011). However, EC presents issues related to spatial representativeness due to its confinement to spatially uniform extensive areas, limiting its applicability in headwater catchments (Gelybó et al., 2013; Xiang et al., 2022).

Other meteorological methods estimate the reference or potential evapotranspiration (PET) using analytical models. PET represents a theoretical measure of the atmosphere's ability to absorb water through evaporation and transpiration. These analytical models are based on principles of energy balance and account for various meteorological and physical factors, including net radiation, ground heat flux, vapour pressure deficit, air temperature, and wind speed (Lu et al., 2005) . PET is also employed to estimate actual evapotranspiration (AET, referred to as ET in the manuscript) by applying variables such as crop coefficients (Yarami et al., 2011), stress factors (Peng et al., 2019), or non-linear relationships (Liu, 2022).

Some widely used PET models include the Penman-Monteith method (Allen, Richard ; Pereira, 1991; Monteith, 1965; Penman, 1948), Blenay-Cradel method (Blaney et al., 1952), and the priestly-Taylor method (Priestley & Taylor, 1972). The Penman method, in particular, is an analytical method that combines energy balance and aerodynamic principles, integrating meteorological variables such as net radiation, temperature, humidity, and wind speed to provide a theoretical estimate of PET.

One limitation of the Penman method is the energy closure issue. The Penman method assumes a complete energy balance between incoming and outgoing fluxes. However, factors like turbulent heat fluxes and storage changes in soil and vegetation canopy can disrupt this balance, leading to

biases in evapotranspiration (ET) estimates, especially for sub-daily measurements (Foken, 2008; Hao et al., 2018). With the advent of electronic, automated weather stations, weather data are increasingly reported for hourly or shorter periods. Therefore, in situations where calculations are computerised, the FAO Penman-Monteith equation can be applied on an hourly basis with good results. The FAO 56 report suggests adjustments in parameters like ground heat flux and the use of standardised sub-daily meteorological inputs to improve the method's robustness at finer temporal scales (Allen, Richard ; Pereira, 1991).

The performance of PET models can also vary depending on location and climatic conditions. For instance, the Priestley-Taylor method is considered a suitable alternative to the Penman-Monteith method in the Ilhéus-BA region (Pimentel et al., 2023). Moreover, these methods face limitations, including the lack of adequate meteorological input data, which may not be available for all regions (Yong et al., 2023). These limitations highlight the need for a more integrated approach to ET estimation that can account for the diverse hydrological processes within a catchment.

The analysis of diurnal fluctuations in groundwater and streamflow has provided a valuable alternative to estimate ET by evaluating its effects on the catchment's hydrological patterns. It has a long history going back to seminal work by White (1932). It is based on the principle that groundwater levels fluctuate during the day due to ET. Many variations of the White method have been developed. Boronina et al. 2005; Fahle & Dietrich, 2014; Gribovszki, Kalicz, Szilágyi, et al., 2008; Loheide II, 2008; Szilágyi et al., 2008), however, they are all based on the original White method.

Previous research on this crucial hydrological phenomenon of diurnal fluctuations has primarily occurred in isolation, often limited to observing and examining fluctuations in smaller catchments and with relatively short record lengths. Moreover, the relationship between diurnal fluctuations and catchment physical features is often neglected, limiting the comprehensive understanding of these phenomena. In summary, the potential of diurnal fluctuations for estimating ET needs more exploration, focusing on its relationships with catchment water and plants and systems.

1.2.2 Identification of Diurnal Fluctuations:

Given their sporadic and infrequent occurrence, analysing diurnal fluctuations has been challenging due to their limited detection. Consequently, there has been a growing need for the development of innovative analytical methods that can enable us to establish meaningful connections between diurnal streamflow characteristics and catchment features.

Current methods for studying diurnal fluctuations in streamflow and water table records typically involve manual identification of diurnal fluctuation episodes (Barnard et al., 2010; Fahle & Dietrich, 2014; Graham et al., 2012; Széles et al., 2018). In these approaches, analysts would visually examine time series data and identify patterns corresponding to diurnal fluctuations, often based on their prior knowledge and experience. This manual identification process is time-consuming and subjective, as it relies on human judgment to detect these fluctuations.

Recently, some time-frequency methods have been used to analyse the diurnal variation in the streamflow, including Fourier transform (FT) (Kovář & Bačinová, 2015; J. D. Lundquist & Cayan, 2002). However, FT has certain limitations, as it is restricted by a fixed window size, which may not adequately capture high-frequency and low-frequency information. Wavelet transforms potentially overcome these limitations by having a flexible window that can capture high-frequency and low-frequency information. (Sinha et al., 2003) However, it does not appear to have been applied to the analysis of daily fluctuations in stream flow. The wavelet transform can provide a unique tool for analysing diurnal fluctuations, improving our understanding of this hydrological phenomenon.

1.3 Thesis Motivation:

Studying and understanding diurnal fluctuations is essential for several reasons. First, they can provide valuable information about the hydrological pathways within catchments and surface-groundwater connectivity (Barnard et al., 2010). Second, diurnal fluctuations can serve as indicators of a catchment's vulnerability to climate change. Changes in the amplitude and duration of diurnal

variations can signal shifts in precipitation patterns, ET rates, and overall hydrological dynamics. (Lundquist & Dettinger, 2003).

In this thesis, diurnal streamflow patterns are explored in depth with a focus on their hydrological implications. Advanced analytical methods are developed to analyse diurnal patterns in long hydrological datasets. The analysis is presented in three interconnected chapters that collectively contribute to a deeper understanding of this hydrological phenomenon.

1.4 Aim and Objectives:

The thesis aims to address the existing research gap in the study of diurnal river discharge fluctuation phenomena by developing innovative analytical methods and conducting comprehensive analyses across various environmental and geographical settings.

The objectives of the thesis are as follows:

1. Investigate the relationship between diurnal streamflow fluctuations and ET for a small catchment and assess their impact on the riparian zone-stream connections.

2. Develop automated advanced analytical tools to study the spatiotemporal variability of daily streamflow patterns centred on wavelet analysis techniques.

3. Conduct a comprehensive data analysis to explore diurnal streamflow patterns across various catchment settings throughout NZ.

By achieving these objectives, this research seeks to improve our understanding of diurnal streamflow fluctuations and their connections with climatic systems and catchment features, thereby contributing to the advancement of hydrological science and environmental management.

1.5 Thesis Organization:

The thesis comprises five chapters, including the introduction. Chapters 2-4 have been written in the style of stand-alone journal articles for publication. Consequently, there is some duplication in the introductory comments and methods between the chapters. The first chapter provides a general literature review and introduction. Chapters 2, 3, and 4 each contain a stand-alone introduction, background literature review, materials and methods, results, and discussion sections. Chapters 2 and 3 are related to the first two Ph.D. research objectives, while chapter 4 is linked to objective 3. Chapter 5 concludes this thesis with a general discussion, summary, and recommendations for future work. In conclusion, each chapter contributes a unique perspective to the overarching goal of comprehensively understanding diurnal streamflow fluctuations, and overall, this research strives to advance our knowledge in this critical area of hydrology.

1.6 Brief Description of Chapters and Publication Details:

Chapter 2: Initial Analysis of Diurnal Fluctuations

Chapter 2 provides a detailed analysis of diurnal fluctuations in streamflow driven by riparian plant evaporation. By scrutinizing the existing literature and manual examination, a new method is devised to compare ET estimates and relate them to the riparian zones. This initial research enhances our understanding of diurnal fluctuations and sets up the subsequent chapters, where advanced analytical techniques are employed to analyse these fluctuations.

Journal Publication: Sarwar, M. W., Campbell, D. I., & Shokri, A. (2022). Riparian zone as a variable source area for the estimation of evapotranspiration through the analysis of daily fluctuations in streamflow. *Hydrological Processes*, *36*(10), e14708. https://doi.org/10.1002/hyp.14708

*Conference Presentation: "*Estimation of ET through signal processing of daily fluctuations in streamflow." NZ Hydrological Society Conference (2019), Rotorua, New Zealand.

Chapter 3: Application of Wavelet Transform

This chapter builds upon the insights gained from our initial analysis of the past methods of analysing diurnal fluctuation. It introduces the application of wavelet transform as a powerful tool for detecting and analysing diurnal episodes in long-term streamflow datasets. This mathematical framework allows us to dissect the temporal dynamics of diurnal fluctuations with unprecedented precision, offering a new perspective on their patterns and underlying drivers.

Submitted and under peer review

Chapter 4: Comparative Analysis of New Zealand Catchments

The fourth chapter extends the investigation into the spatiotemporal variability of diurnal fluctuations in different catchments in New Zealand. By comparing diurnal fluctuations across various catchment characteristics, we seek to discern regional variations and identify critical factors influencing diurnal streamflow dynamics. This comparative analysis not only broadens the scope of our research but also provides valuable insights for water resource management strategies tailored to specific physiographical contexts.

Will be submitted along with the thesis.

Chapter 2. Riparian Zone as A Variable Source Area for The Estimation of Evapotranspiration Through the Analysis of Daily Fluctuations in Streamflow

2.1 Abstract

Evapotranspiration is a significant component of the water balance of a catchment, and riparian zones play a critical role in the hydrological process. However, little is known about the influence of riparian zones on Evapotranspiration, especially at a catchment scale. A new method is developed to estimate the time series of riparian Evapotranspiration and variation of the active riparian area around the stream by analysing the streamflow response to diurnal Evapotranspiration. The daily fluctuations in the streamflow hydrograph are interpolated to reflect evapotranspiration losses. The PET calculated by FAO-56 is used as an accurate reference for validation. The new method is more straightforward and cost-effective compared to conventional techniques. In addition, the new approach estimates average Evapotranspiration across the entire riparian area rather than a point observation.

2.2 Introduction

For many decades, studying the impact of Evapotranspiration (ET) on the hydrological process of a catchment has been challenging (Gribovszki, Kalicz, Kucsara, et al., 2008; Loheide II, 2008; Troxell, 1936; Weisman, 1977) significantly impact water table and streamflow, especially in a heterogeneous environment with shallow water table-like riparian zones, where plant roots have immediate access to groundwater resources (Kellogg et al., 2008; Satchithanantham et al., 2017).

The riparian zone is often defined as part of the landscape along the boundaries of a water body (Rugenski et al., 2017). However, there is a diverse interpretation of the definition of the riparian zone in the literature. Sometimes, the riparian zone is defined as a fixed width from the stream network. For example, Reigner (1966) indicates that an area of up to 2 m from the stream is the riparian zone, as this area considerably impacts streamflow. Geisler (2016), on the other hand, suggests that the area adjacent to the stream with a slope of less than 25° is the riparian area. Figure 2.1 shows an interpretation of the riparian zone by Reigner (1966) and Geisler (2016). Still, these suggestions conflict with some experimental studies' findings that the riparian area shrinks gradually as the catchment dries out (Barnard et al., 2010; Bond et al., 2002; Graham et al., 2012; Tschinkel, 1963).

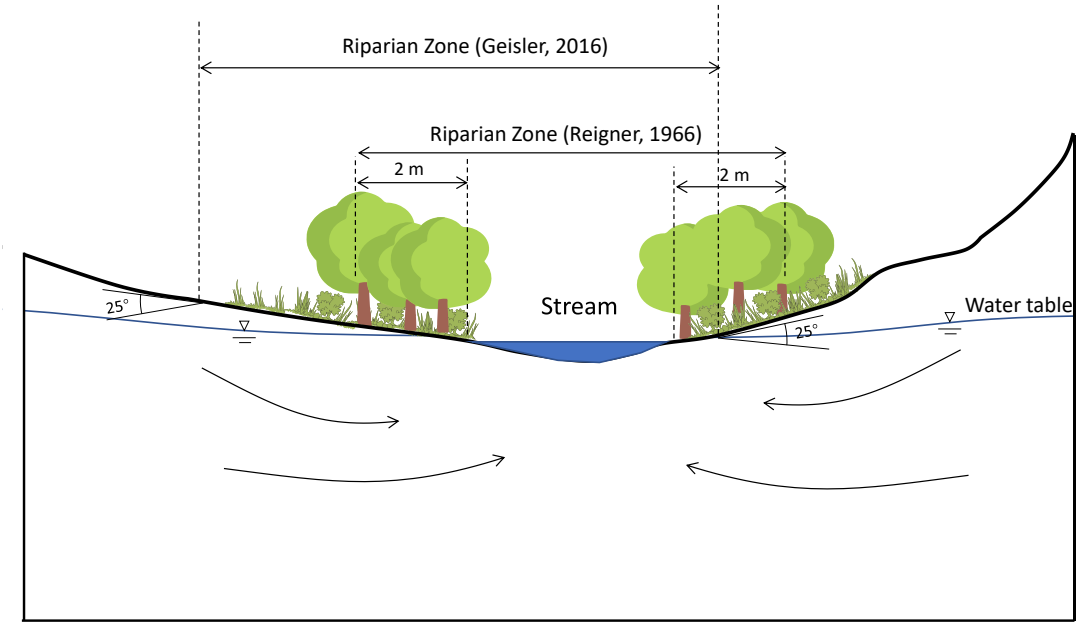

Figure 2.1 A schematic diagram of a riparian zone along the stream banks

Characteristics of the soil and vegetation in the riparian area are often different from the surrounding landscape due to their vicinity to the water resources. Consequently, the riparian zone substantially impacts streamflow more than the rest of the catchment (Johnson et al., 2013; Martí et al., 2000).

Considering that the riparian zone has water availability throughout the year, this zone is a critical region for the ET process, particularly during the dryer seasons (Johnson et al., 2013). Thus, studying the influence of ET on riparian zones and, consequently, on the water table and streamflow can reveal critical information on vegetation-stream interactions in catchments (Széles et al., 2018). Nevertheless, several challenges for estimating ET from riparian zones are indicated in the previous studies. For example, the narrow width of the riparian buffer around a stream is likely below the fetch requirements of the eddy covariance and Bowen ratio ET measurement techniques (Goodrich et al., 2000; Nachabe et al., 2005). Also, installing lysimeters in the vegetation corridor along streams is costly and only yields point measurements.

Alternatively, physiographical methods such as crop coefficients, sap flow, and leaf chamber systems are highly effective in determining ET rates using simple techniques at a relatively low cost

(Lascano et al., 2016). However, the physiographical methods are ineffective when there is a degree of non-homogeneity in the vegetation and soil types (Goodrich et al., 2000). In such cases, the reliability of these methods can be compromised, and alternative approaches or complementary data sources may be necessary to account for the complexity of the ecosystem.

On the other hand, the day and night variation in solar radiation leads to daily fluctuation in ET (Széles et al., 2018). These daily changes in ET cause a periodic depletion and replenishment of groundwater from riparian vegetation, which impacts the discharge and produces daily fluctuations in streamflow (Bond et al., 2002; Burt, 1979; Graham et al., 2012; Gribovszki et al., 2010; J. D. Lundquist & Cayan, 2002; Schwab et al., 2016). Often, diurnal fluctuations are characterized by a local maximum in the early morning followed by a local minimum in the afternoon (Gribovszki et al., 2010). The daily fluctuations in the water table, soil moisture, and streamflow in response to higher ET during the daytime show potential for estimation (Dolan et al., 1984; Troxell, 1936; White, 1932).

White (1932) was the first to establish a method for estimating ET from daily water table fluctuations. He used a uniform recovery rate over 24 hours to calculate the total volume of water evaporated due to diurnal water table fluctuations. To date, the White method has received extensive modifications (Fahle & Dietrich, 2014; Loheide II, 2008; Nachabe et al., 2005; Szilágyi et al., 2008). However, the high spatiotemporal variability of groundwater recharge and specific yield remain the primary challenge of the White method (Fahle & Dietrich, 2014).

The daily fluctuations in streamflow are also a practical and cost-effective way of characterizing catchment hydrological processes (J. D. Lundquist & Cayan, 2002; Széles et al., 2018). Some studies used the diel fluctuations in streamflow to estimate riparian zone ET (ET_r). Troxell (1936) and Boronina et al. (2005) estimated ET_r using a similar approach to the White method by assuming a constant recharge and computing the daily flow deficit caused by ET during a flood recession. (Loheide II, 2008), on the other hand, developed an empirical relation based on the rate of change of groundwater level during the periods of zero ET at night to include the change in recharge between

days and nights. Later, Cadol et al. (2012) modified an empirical relation for estimating ET from streamflow fluctuations by combining the empirical Equation developed by Loheide II (2008) with the daily streamflow deficit. However, uncertainties in identifying specific yields and groundwater recharge for each night made these methods less practicable (Fahle & Dietrich, 2014). In addition, some studies show that the riparian zone and vegetation in streams play a dominant role in producing and controlling the daily fluctuations in streamflow (Barnard et al., 2010; Bond et al., 2002; Graham et al., 2012).

Some studies also report a lag time (t_{lag}) between the maximum ET in the catchment and minimum streamflow at the outlet for each diurnal fluctuation. For example, the maximum ET is observed between 12 pm – 3 pm, and the minimum flow is between 5 pm - 8 am (Kirchner, 2009; Szilagyi et al., 2007; Troxell, 1936). The lag time is reported to vary seasonally due to flow path change and flow velocities (Barnard et al., 2010; Cadol et al., 2012). Also, it is suggested that the lag time can result from the riparian system's dynamical lag to integrate the effects of its sinusoidal inputs into outputs over time (Kirchner et al., 2020).

The total lag measured at the catchment outlet shows the overall catchment response to transpiration. However, it can be broken down into time portions taken by individual hydrological processes involved in the propagation of diurnal signals. For example, the time plants take to transport sap flow in response to radiation, the time measured between the diurnal peaks in groundwater level and baseflow (Szilágyi et al., 2008), and the instream time associated with the streamflow velocity.

Research on diurnal fluctuations highlights the intricate interplay between water availability, groundwater storage, and riparian dynamics. However, previous studies have scarcely discussed the relationship between ET and the riparian area as a source for generating the diurnal fluctuation. The role of riparian areas in modulating fluctuation lag and amplitude also needs further investigation to form a comprehensive understanding of the hydrological process involved in this phenomenon.

Therefore, the main aim of this study is to analyze the daily streamflow fluctuations to estimate an hourly and daily time series of ET and evaluate the area of the riparian zone around stream networks.

The new approach emphasizes the interconnection between ET and the riparian zone to quantify the relationship between ET and daily streamflow fluctuations and investigate how changes in the riparian area affect ET loss.

2.3 Methodology

2.3.1 Study area

The Toenepi stream (WGS84 coordinates: -37.7146, 175.5632) drains a small catchment in the Waikato region, New Zealand

Figure 2.2. The catchment has an area of 1.6 ha and an elevation range from 40 to 130 m above mean sea level.

The catchment is one of the five representative dairy focus catchments in New Zealand, with great weather and hydrological data (Wilcock et al., 2006). The ground surface topography is primarily flat (max slope 6.5%) and fully covered by pasture apart from the riparian plantings around the Toenepi stream, consisting mainly of shade trees and shrubs (Wilcock et al., 2006).

The vicinity of the stream comprises poorly drained Topehaehae soils (13%) developed from recent alluvium on river flood plains, 47% freely drained sandy loam textured Kereone and Kiwitahi soils, and 40 % of clay textured Morrinsville ash soils (Müller et al., 2010).

The catchment receives an annual average rainfall of 1160 mm with an estimated ET of 892 mm/year (2003–2012), which gives a yearly water yield of around 399 mm/year (Woodward et al., 2013).

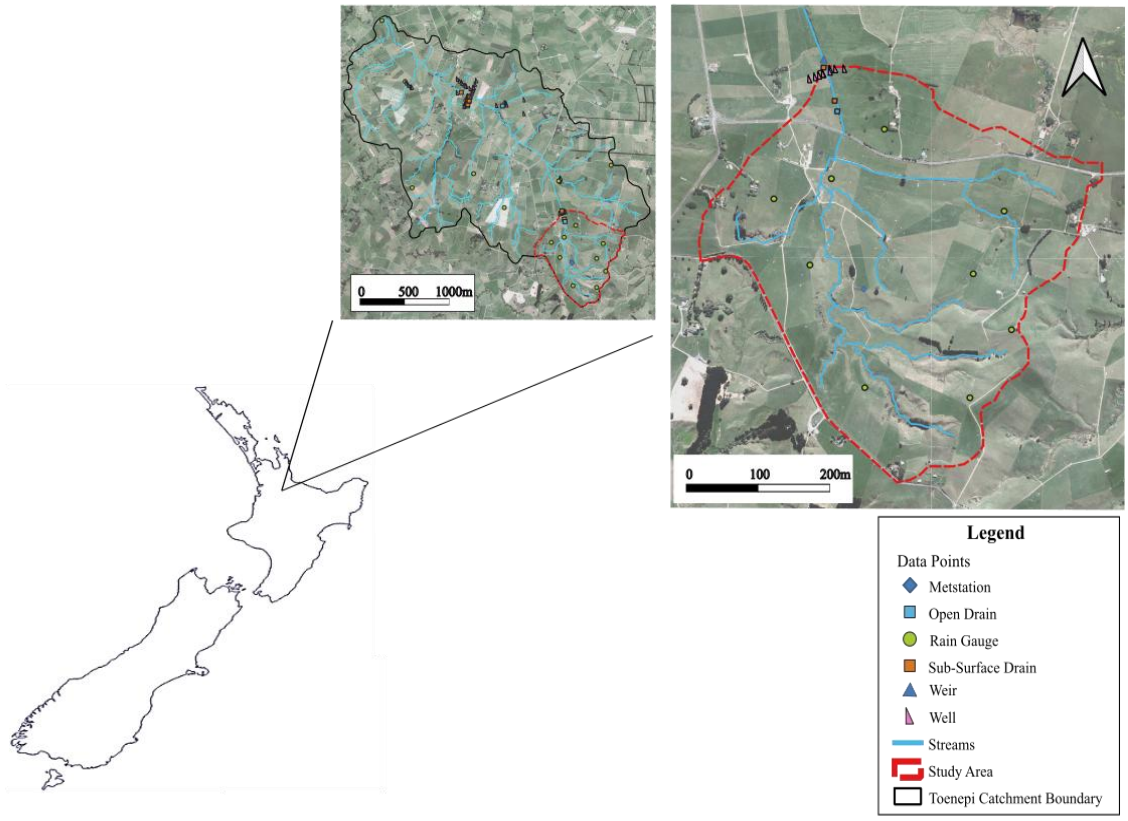

Figure 2.2 The Toenepi catchment and the study area boundary

2.3.2 Data access and recession analysis

The streamflow was monitored continuously from 1995 to 2014 at a 15-minute resolution, using a V-notch weir at the outlet (Wilcock et al., 2006). For this study, the 15-minute streamflow is converted to hourly values to be unified with the other meteorological data obtained from the weather station in the study area. Then, hourly potential evapotranspiration (PET) time series are calculated using the FAO-56 Panman-Montieh method (Allen, Richard G; Pereira, 1991).

Pronger et al. (Pronger et al., 2016) suggested that the PET calculated from the FAO-56 method is an appropriate reference for estimating actual ET in pasture systems in the study area. Scotter and Heng (2003) suggest that most pastures in New Zealand behave like the reference crop for most of the year. In addition, considering that the majority of vegetation in the riparian area has access to

adequate groundwater resources and water fluxes, PET reasonably estimates the actual ET in the riparian zone (Loheide et al., 2005).

The hourly streamflow data from 2003 to 2013 are analyzed to detect the diel fluctuations. Sub-daily random picks in the recession curves are ignored as they could be attributed to local and small rain events. The end of fluctuation episodes is observed when either the recession is interrupted by a rain event or the flow rate becomes too low to carry any signal. In general, three types of fluctuation scenarios are observed in the flood recessions. Balanced fluctuations (Figure 2.3a) are usually observed in the middle of a recession curve when the hydrograph is flat at night and steep in the day. Rising fluctuations (Figure 2.3b) are observed at the end of a flood recession curve when the streamflow increases at night. It was not rare to see all three types of fluctuations in one long recession curve if the recession curve is interrupted by a rainfall event. Steep fluctuations (Figure 2.3c) usually occurs at the beginning of a recession curve when the riparian zone shrinks rapidly and the discharge from groundwater declines rapidly. Any combination of all three types of fluctuations may be observed in a single prolonged recession.

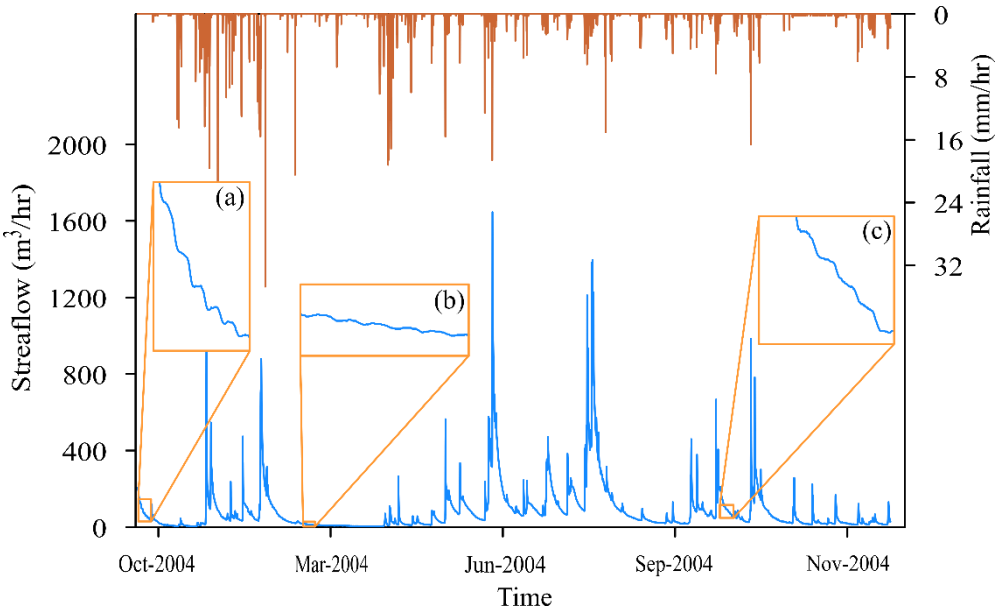

Figure 2.3 Types of diurnal fluctuations observed in the hourly streamflow record in Toenepi.

Forty-one flood recessions with at least four days of fluctuations are detected. The duration of the flood recessions is usually longer in warmer months, as they are less likely to be interrupted by any precipitation. Noticeable diurnal fluctuations started from late winter in August, dominated in spring (September- November) and summer (December – February), and diminished around early autumn in March. No flood recession was observed between April and July that meets the required criteria. Figure 2.4 shows the most extended fluctuation event from 12-Jan-2005 to 31-Jan-2005, when a streamflow recession with daily fluctuations was observed for 19 days before it was interrupted by a rainstorm. During this flood recession, the PET started at around 6 a.m., reached a maximum value around noon, and dropped to zero shortly after 7 p.m. A lag time of 5 hours is observed between the PET and streamflow deficit Q_d peaks.

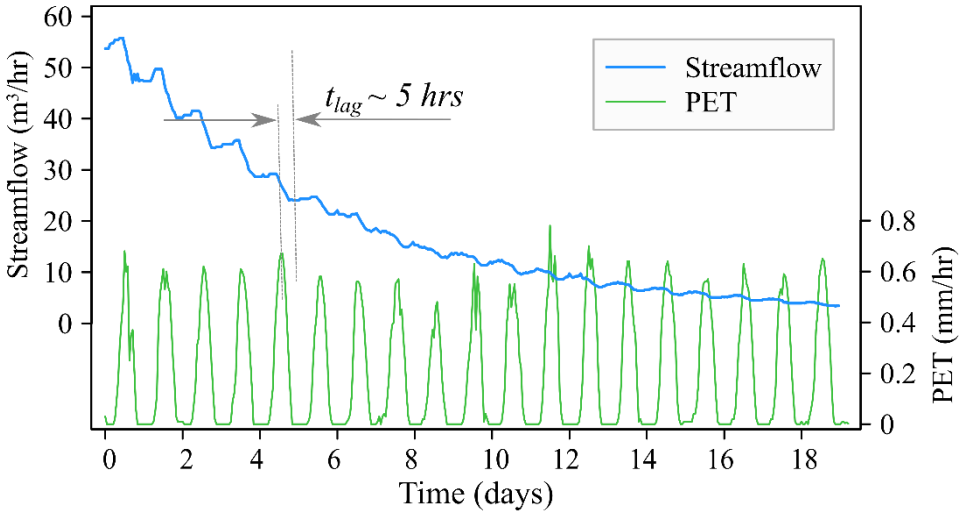

Figure 2.4 Daily flow fluctuations in Toenepi Stream in response to temporal variations in ET from 12-Jan-2005 to 31-Jan-2005

2.3.3 Calculation of Riparian ET (ETr)

A conceptual cross-section of a riparian zone is illustrated in Figure 2.5. In the absence of rainfall during a flood recession, the catchment water balance can be written as:

$$Q_{SF} - Q_R - Q_{ET} = \frac{dV}{dt} \tag{2.1}$$

where Q_{SF} is the observed streamflow at the outlet, $Q_{R.}$ is the groundwater recharge, Q_{ET} is the ET flow abstract, and $\frac{dV}{dt}$ is the water storage change in the river network. Since ET is negligible at night, the only source of stream flow is groundwater recharge, which recharges recedes without a rain event—however, the difference in recharge rates between day and night results in a diurnal streamflow fluctuation.

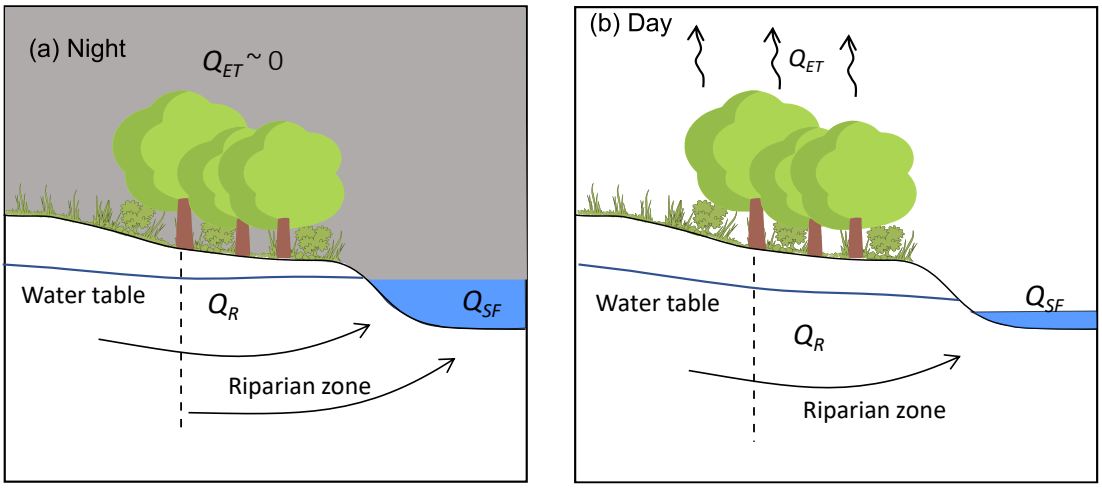

Figure 2.5 A conceptual cross-section of a riparian zone and water balance components that contribute to streamflow during (a) night and (b) day

In this study, a similar approach suggested by Gribovszki et al. (2008) for estimating ET from groundwater table fluctuations is adopted for streamflow fluctuations. A Bezier-Spline interpolation curve is fitted to the observed streamflow hydrograph in this method. An example of fitting a Bezier-Spline interpolation curve to a streamflow hydrograph is illustrated in Figure 2.6.

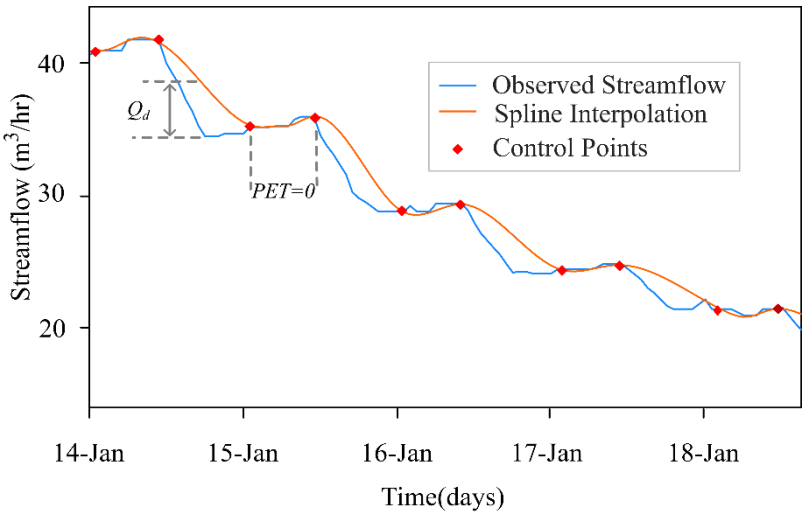

Figure 2.6 An example of fitting a Bezier-Spline interpolation curve to a streamflow hydrograph, estimation of streamflow deficit Qd. and a comparison with PET and Q_d

The interpolation curve is formed by linking the daily minimum and maximum discharge points at the beginning and end of the periods when the effect of ET became negligible on streamflow. The time series of ET from the active riparian area (ET_r) is obtained by the equation (2.2) below

$$ET_r(t - t_{lag}) = \frac{Q_d(t)}{A_r(t)} \tag{2.2}$$

where t_{lag} is the lag time between the maximum ET and minimum streamflow observed at the outlet for each fluctuation, $ET_r\ (t\text{-}t_{lag})$ is the time series of average ET abstracted from the riparian area at, $Q_d(t)$ streamflow deficit is the difference between the interpolation curve and streamflow at the outlet, and A_r is the size of the riparian zone that actively contributes to the streamflow fluctuations.

2.3.4 Time series of the area of the riparian zone, Ar(t)

As the catchment starts to dry out, groundwater storage in the riparian area decreases. As a result, the riparian zone shrinks gradually at the same rate as the groundwater storage reduces. Although the ET per unit area remains unchanged during the recession, the total volume of water ET loss in the riparian zone decreases slowly as the size of the riparian area decreases. This information is critical for understanding the dynamics of riparian ecosystems and underscores the significance of

effective conservation strategies in maintaining ecological balance. A conceptual example of the shrinkage of the active riparian area around a stream network in three timesteps is illustrated in Figure 2.7.

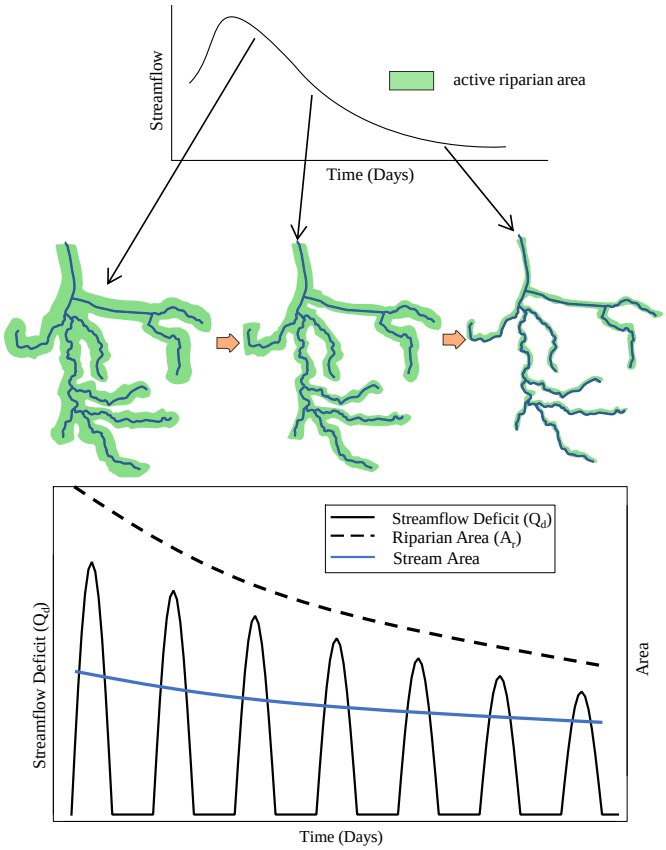

Figure 2.7 A schematic of the active riparian area around a typical stream network after a flood event in three timesteps

An exponential expression often explains the flow decline during a recession (Tallaksen, 1995).

$$Q_{SF} = Q_0 k^t \tag{2.3}$$

Q_{SF} is the streamflow in the recession period, k is the recession constant, and Q_0 is the flow at the beginning of the recession.

The start of a recession Q_0 can be defined using a baseflow separation method like a recursive digital filter-based flow separation method (Lyne & Hollick, 1979). Figure 2.8 shows the Mathematically,

$$Q_q(t) = \begin{cases} -\alpha Q_q(t-1) + \frac{1+\alpha}{2}[Q_s(t) - Q_s(t-1)] & for \quad Q_q(t) > 0 \\ 0 & otherwise \end{cases} \tag{2.4}$$

$$Q_b(t) = Q_s(t) - Q_q(t) \tag{2.5}$$

where *Qq(t)* is the filtered quick flow at time t, *Qq(t-1)* is the quick flow component at time t-1, *Qb(t)* is the baseflow, and α is the digital filter parameter. The fast digital filter method gives consistent and easily reproducible results (Nathan & McMahon, 1992).

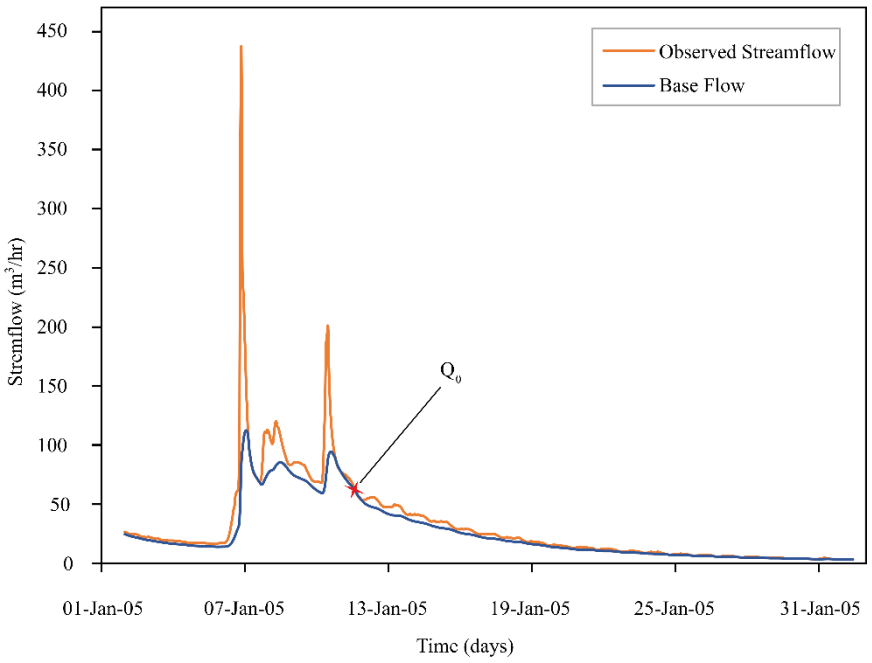

Figure 2.8 Baseflow separation using the recursive digital filter method to define the starting point of a recession.

During a flood recession, in which groundwater recharge is the only resource, and ET is the only abstracting agent, the area of the riparian zone is assumed to be directly proportional to the streamflow rate. Therefore,

$$A_r(t) = A_0 k^t \tag{2.6}$$

Where, A_0 is the initial active riparian area at the beginning of the recession.

Combining equations (2.3) and (2.6) and yields:

$$A_r = \frac{A_0}{Q_0} Q_{SF} \tag{2.7}$$

Then, combining equations (2.2) and (2.7) yields:

$$ET_r\left(t - t_{lag}\right) = \frac{Q_0 Q_d(t)}{A_0 Q_{SF}(t)} \tag{2.8}$$

Equation (2.8) hereafter is the "new method" for estimating a time series of average ET abstracted from the active riparian area (ET_r).

2.4 Results and Discussion (Application of the method)

2.4.1 Estimation of ETr

The time series of Q_d (the difference between the interpolation curve and streamflow) is calculated by fitting Bezier-Spline interpolation curves to flood recessions. As an example, an hourly time series of Q_d for the recession curve from 12-Jan-2005 to 30-Jan-2005 is illustrated in Figure 2.9. The magnitude of Q_d declines as the average daily discharge decreases during the flood recession.

Sometimes, the Q_d value becomes negative during the night when the spline curve does not follow a sharp change in the actual recharge rate at the start and end of the night. The negative Q_d values are removed from the Q_d time series.

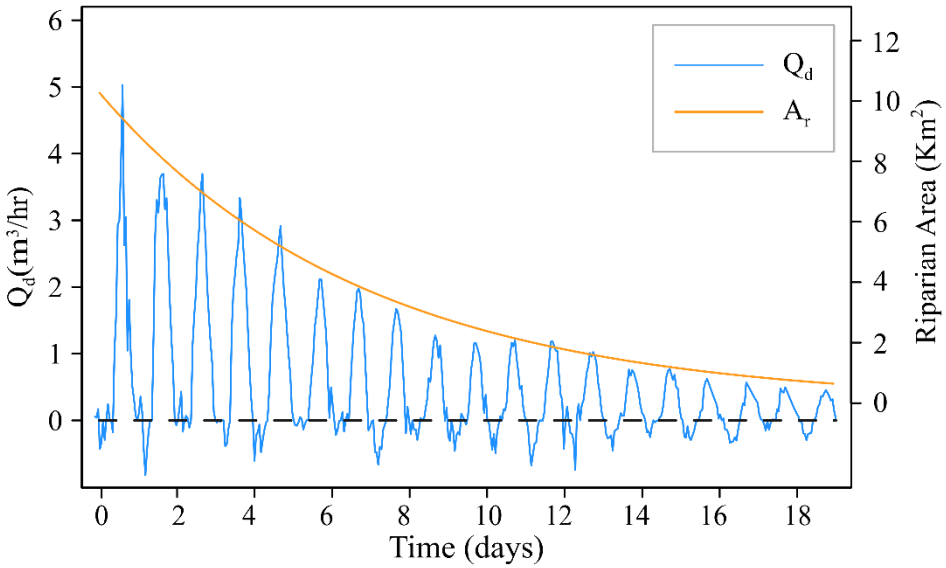

Figure 2.9 An hourly time series of Qd and hourly time series of riparian area (A_r) in Toenepi stream from a flood recession period between 12-Jan-2005 to 30-Jan-2005

Assuming PET truly represents ET in the riparian area, the hourly time series of ET_r is calculated by minimizing the root-mean-square error between PET and ET_r calculated from Equation (2.8 by varying A_0 as a changing variable in MS Excel solver.

The goodness of fit measure suggested by Kling-Gupta efficiency (KGE) (Gupta et al., 2009) measures the correlation between PET and ET_r.

$$KGE = 1 - \sqrt{(r-1)^2 + \left(\frac{\mu_{PET}}{\mu_{ET_r}} - 1\right)^2 + \left(\frac{\sigma_{PET}}{\sigma_{ET_r}} - 1\right)^2} \quad (2.9)$$

where r is Pearson's correlation between PET and ET_r, μ_{PET} is the mean of PET, μ_{ET_r} is the mean of ET_r, σ_{PET} is the standard deviation of PET, and σ_{ET_r} , is the standard deviation of ET_r. KGE ranges between 0 and 1, where 0 means no correlation, and 1 represents a perfect correlation.

The estimated ET_r with and without considering 5 hrs lag time are compared with PET and shown in

Figure 2.10. The correlation is not strong when the lag time is neglected. However, by offsetting the ET_r values by 5 hours, a clear relationship appears in

Figure 2.10b. Eventually, the lag time that results in the most significant KGE value is considered the best between PET and Q_d.

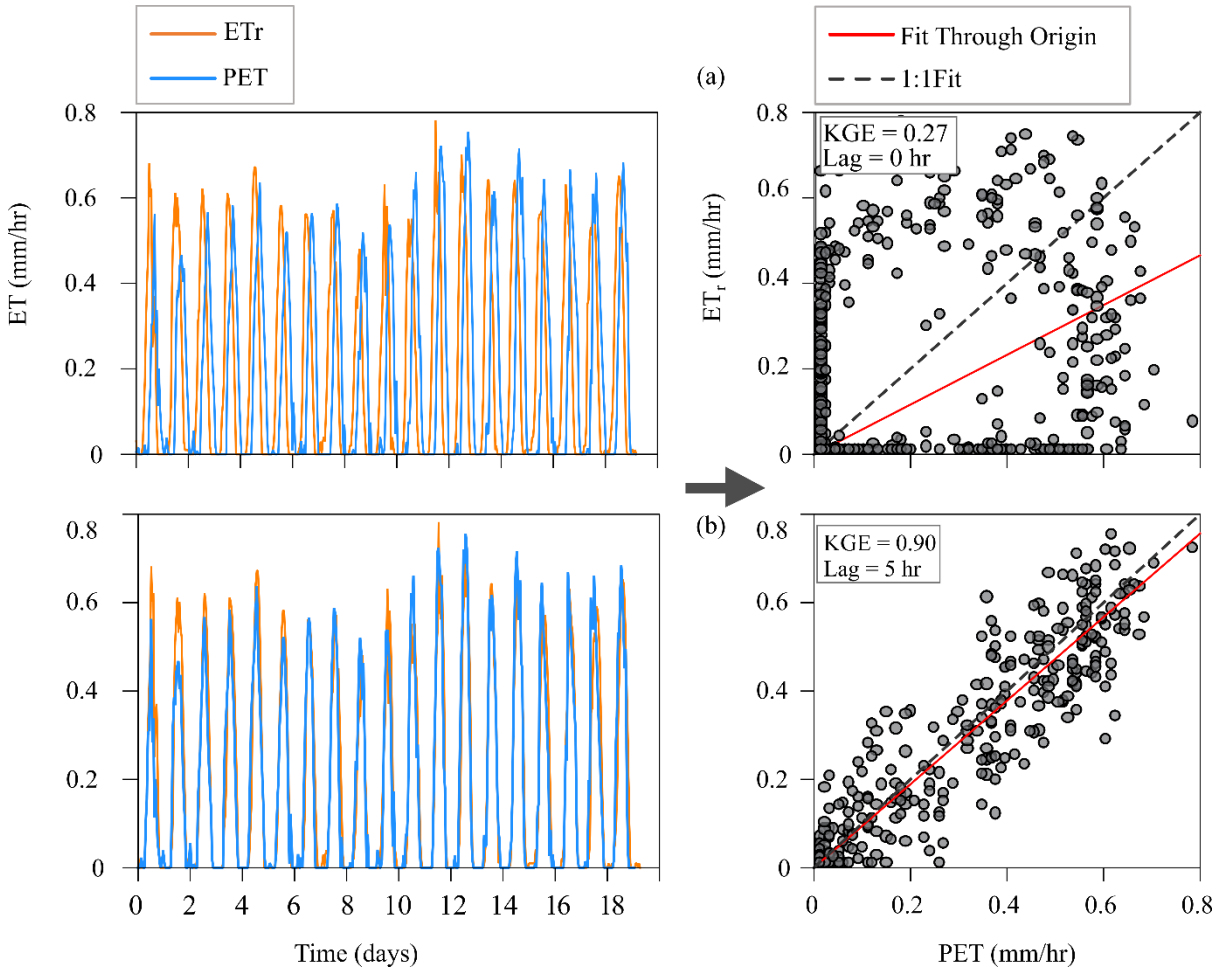

Figure 2.10 A comparison between hourly time series of PET and ET_r (a) without lag time, (b) with 5 hours lag time for 19 days flood recession period between 12-Jan-2005 to 30-Jan-2005

The recession constant (k) is calculated as 0.006 by fitting Equation (2.6) to hourly streamflow for each recession episode, and A_0 is estimated as 10.18 Km^2 by minimising the root-mean-square error between PET and ET_r. Figure 7 illustrates the hourly time series of the riparian area (A_r) estimated by substituting A_0 and k values in Equation 6. Eventually, a comparison between the time series of A_r and Q_d indicates that the diel signal amplitude is directly proportional to the size of the riparian area.

2.4.2 Analysis of hourly time series of ETr

Appendix 1 illustrates hourly estimates of PET and ET_r for 41 flood recessions, along with the goodness of fit (KGE) and lag time.

Analysing the hourly time series of PET shows that solar radiation plays a vital role in calculating PET. A footprint of solar radiation on PET is visible as some local peaks in the hourly PET time series are shown in Figure 2.11. It is exciting to see that the exact impact is recognisable in the hourly ET_r graphs in Figure 2.11. The footprint of solar radiation on ET_r is more recognisable in spring and early summer events.

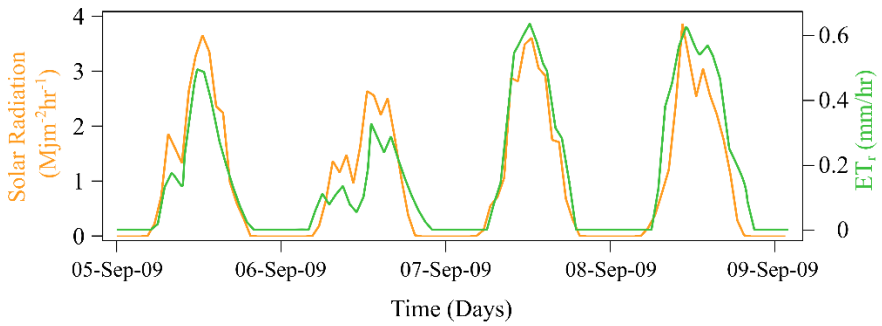

Figure 2.11 Analyzing the impact of solar radiation on PET and ETr

Overall, the new method shows an acceptable performance in estimating the hourly time series of ET_r compared to PET. For example, the average goodness of fit (KGE) for all flood recession events

is 0.83. However, a better correlation between ET_r and PET is observed when there are fewer variations in solar radiations during the day, and PET has a simple bell shape graph. For example, in a spring event from 05/09/2009 to 09/09/2009, the goodness of fit between PET and the new method is 0.96. On the other hand, when solar radiation frequently changes, the correlation between PET and ET_r declines.

2.4.3 Seasonal variation of lag times

The lag time is calculated for all recession episodes. A summary of seasonal variation of the lag time between ET_r and streamflow response is illustrated in the Toenepi stream from 2003 to 2013 (Figure 2.12).

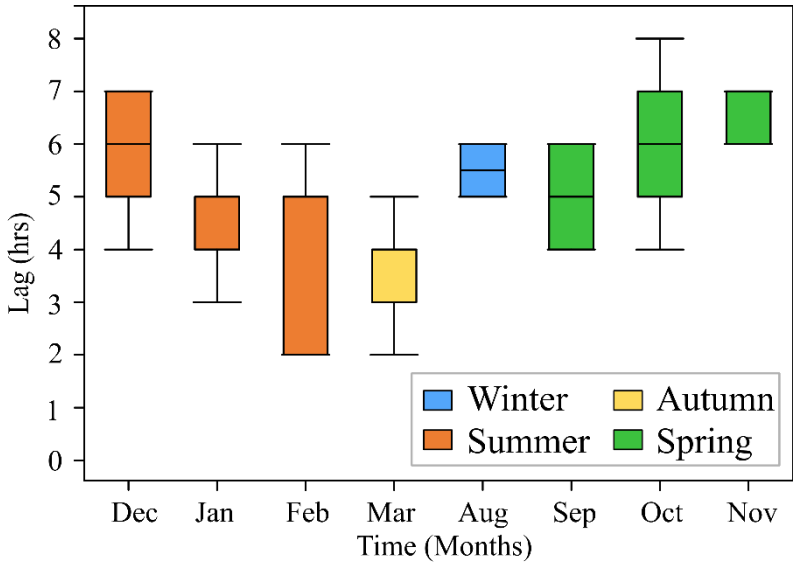

Figure 2.12 Seasonal variation in the lag time t0 between ETr and streamflow response in the Toenepi stream from 2003 to 2013

On average, of 41 cases, the lag time is 4.86 hours, with a standard deviation of 1.47 hours. It is observed that the lag time (t_{lag}) and the streamflow deficit (Q_d) vary seasonally. The average lag time is slightly shorter in spring (5 hrs) than in summer (5.52 hrs). One explanation for the seasonal variation is that the seasonal change in vegetation in streams results in varying the roughness of the stream networks and, consequently, average velocity and lag time. Also, various activities in generating ET-induced diel signals in the streamflow vary seasonally. These activities include solar

radiation, transpiration from the stomata, sap flow movement in the plants, root water uptake, groundwater movement, baseflow discharge to streams, and in-stream travel time to the measuring point.

The shortest lag times of 2-3 hours are observed for shallow flow (< 2 m^3/hr) in the events in February and March. These short lag times for low flows suggest that a tiny proportion of the area near the stream contributes to the streamflow. Therefore, any change in the ET rate more rapidly impacts the streamflow at the outlet.

The average daily ET_r and PET for all events are calculated and illustrated as a scatterplot in Figure 2.13. The summer events show a higher average daily ET_r, around 2.5 to 5 (mm/day), and winter events are the lowest at around 1.5 (mm/day). In autumn and spring events, the average daily ET_r ranges from 1.5 to 4 (mm/day). The scatterplot shows a good agreement between average daily PET and ET_r with a goodness of fit of (KGE=0.88). However, comparing a linear trendline to all events with a 1:1 line shows that the daily average ET_r is marginally lower than PET.

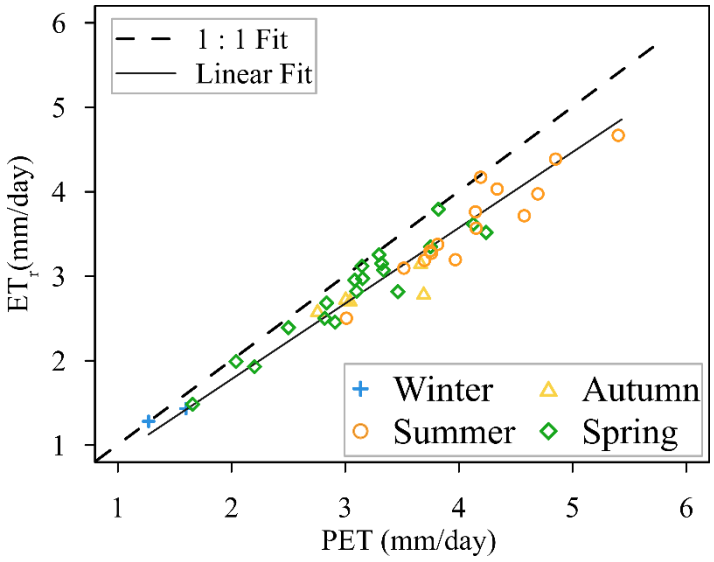

Figure 2.13 Seasonal comparison of daily average PET and ETr

2.5 Conclusions

This study developed a new method to estimate the time series of riparian ET by analysing the streamflow response to diurnal ET. The daily flow fluctuations are assumed to occur because of the ET differences between day and night. The new method also estimates the temporal variation of the riparian area during a flood recession by assuming a linear correlation between groundwater storage and active riparian area. The estimated riparian ET from the new method shows an acceptable correlation with the hourly PET calculated from FAO 56. In addition, the new method requires fewer experimental parameters to estimate ETabstracted from riparian zones than PET.

2.6 Acknowledgments

The authors thank Lincoln Agritech Ltd. for providing flow and weather data.

Data availability

The data supporting this study's findings are available from the corresponding author upon reasonable request.

Chapter 3. Application of Wavelet Transform for Extracting and Analysing Evapotranspiration-Induced Diel Fluctuations in Streamflow Records

3.1 Abstract

Diurnal fluctuations in groundwater and streamflow are produced due to evapotranspiration, indicating a strong connection between streamflow and the groundwater reservoir. Studying the patterns of diel fluctuations can provide valuable information on the hydrological processes in a catchment. Analyzing these fluctuations makes it possible to estimate the evapotranspiration rate as well. In this paper, the signal analysis technique of the wavelet transform is applied to the streamflow time series to extract and analyze diel fluctuations. The performance of two main types of Wavelets transform, continuous and discrete, is accessed against widely applied methods of trend extraction like moving average. The results show that wavelet transform can be used successfully to identify periodic and non-periodic features of the time series, such as seasonal and trend components, and to distinguish between signal and noise. The continuous wavelet transform demonstrates that the diurnal component of streamflow exhibits significant variation over different temporal scales, with the dominant periods ranging from 12 to 36 hours. In conclusion, the findings suggest that wavelet

transform can effectively capture evapotranspiration-induced diurnal streamflow fluctuations and provide insights into the hydrological processes at different temporal scales.

3.2 Introduction:

Diurnal fluctuations in groundwater and streamflow are high-frequency oscillations produced due to the natural dynamic response of the groundwater reservoir against external environmental forces like evapotranspiration (ET). Studies of Diel fluctuations in the streamflow can reveal the temporal patterns and dynamics of water movement and storage in streams, affecting the stream system's water quality, ecology, and management (Kirchner et al., 2020). In addition, diel fluctuations in groundwater and streamflow indicate the presence of a robust connection between streamflow and groundwater (Széles et al., 2018). When diel fluctuations in groundwater and streamflow are observed, it suggests a complex interaction and water exchange between the stream and the underlying groundwater system. Therefore, analysis of diel fluctuations can reveal key hydrological characteristics of a catchment, like the sources and pathways of water in streams (Barnard et al., 2010), the rates and magnitudes of water exchange between streams and their surrounding environments, and the impacts of human activities on stream hydrology (Satchithanantham et al., 2017).

Some studies have analysed diel fluctuations to estimate riparian ET by computing the streamflow loss during each diel cycle (White, 1932; Troxell, 1936; Tschinkel, 1963; Boronina et al., 2005; Gribovszki, Kalicz, Kucsara, et al., 2008; Loheide II, 2008; Cadol et al., 2012; Sarwar et al., 2022). While some others have focused on investigating the origin and the mechanisms of propagation of the diel signals in Streamflow (Barnard et al., 2010; Graham et al., 2012).

In recent years, hydrologists have used time-frequency analysis methods to better understand the complex dynamics and characteristics of variations and trends in hydrological time series. For example, (J. D. Lundquist & Cayan, 2002) showed the capabilities of applying time-frequency

techniques like the Fourier Transform in identifying the distinct periods where diel signals predominately affect baseflow recession.

Similarly, Wavelet analysis is another practical time-frequency approach utilized to examine variations, periodicities, and trends in diverse geophysical time series (Mallat, 2009). Compared to Fourier analysis, Wavelet analysis offers the advantage of revealing different time-frequency components within a time series that can be localized in both the temporal and frequency domains. (Smith et al., 1998).

Wavelet analysis has been applied in hydrology since the early 1990s due to its ability to analyze non-stationary datasets (Rhif et al., 2019; Sang, 2013). It has been shown that Wavelet analysis is an effective tool for extracting non-trivial and potentially useful time-frequency information from non-stationary data sets available in geosciences (Percival, 2008). Some of the applications of Wavelet analysis in hydrology are multiresolution analysis of hydrologic time series (Chong et al., 2019), denoising of hydrologic series to allow for the detection of underlying trends and variations (Sang, 2012), simulation and forecasting of hydrologic series using wavelet-aided convolution neural networks (Adamowski & Sun, 2010), and analyzing groundwater level fluctuations including the decomposition of time series into different frequency components (Huang et al., 2021). Moreover, derivative techniques of Wavelet transform, like Wavelet cross-correlation and coherent analysis, are used by (Briciu et al., 2019) to compare and correlate upstream and downstream diurnal cycles of different water quality parameters.

Further, CWT can aid in characterizing extreme events such as floods or droughts by revealing their temporal signatures and how they may change over time in relation to the macroclimate indexes (C. A. G. Santos & de Morais, 2013). Studies by (Sang, 2013; A. Zhang et al., 2015) have used the time-frequency information from CWT to improve forecast models' accuracy and hydrological processes' accuracy. Combining CWT with statistical models like ARIMA improved forecasting models for hydrological time series by capturing the non-stationary characteristics of hydrological time series (Wu et al., 2021). CWT has models. Additionally, wavelet analysis methods have been used to study

the characteristics of hydrological processes and their applications, including serial correlation analysis, frequency analysis, and fuzzy analysis (Sang, 2013).

Understanding the daily characteristics of streamflow offers a window into the time-varying impact of different environmental parameters on catchment hydrological processes. However, investigating diel fluctuations presents challenges due to the intricate and highly variable spatiotemporal nature of the hydrological dynamics involved in these processes (Graham et al., 2012). The numerical and analytical methods utilised in the abovementioned studies have been valuable for quantifying the link between diel signals and ET. However, these methods do not fully capture the entire range of information on diurnal characteristics. They fall short of capturing details such as the timing and magnitude of the daily peaks, which can vary across different periods and locations (Xiao et al., 2018). This limitation comes from the fact that these methods primarily focus on the time domain of streamflow signals, neglecting the frequency components of the streamflow signal (Yan et al., 2020). Diurnal fluctuations are naturally occurring frequency-based phenomena, and only relying on time-domain analyses could lead to the oversight of crucial frequency-dependent patterns and dynamics (Grinsted et al., 2004; Rhif et al., 2019).

However, the previous studies examining diurnal fluctuations in streamflow have primarily relied on time-domain analyses, such as calculating mean daily streamflow values or investigating trends in the data (Czikowsky & Fitzjarrald, 2004; Loheide II, 2008; Sarwar et al., 2022). While these methods provide valuable insights into the overall daily hydrological behavior of the system, they may not fully capture the comprehensive range of information on daily characteristics. These approaches often overlook critical frequency-dependent patterns and dynamics inherent in diurnal fluctuations, which can be essential for understanding the temporal impact of environmental parameters on catchment hydrological processes (Percival, 2008).

This study addresses these limitations by employing Wavelet analysis to investigate the temporal changes in diurnal streamflow fluctuations. The specific objectives of this study are: (1) to choose the optimal wavelet family to decompose streamflow time series into multiple lower resolution

levels, (2) to remove trends using wavelet thresholds and extract diel signals, and (3) to represent diel signals at different scales and times through a power spectrum of the continuous wavelet transform.

3.3 Methodology

3.3.1 Overview of Continuous and Discrete Wavelet Transform

Wavelet analysis has two main types: continuous wavelet transform (CWT) and discrete wavelet transform (DWT) (Vetterli & Herley, 1992). The following integrated expression gives the CWT of a signal $x(t)$

$$\tilde{x}(\tau, s) = \frac{1}{\sqrt{s}} \int_{-\infty}^{+\infty} x(t) * \overline{\psi}_{s,\tau}\ (t)dt \tag{3.1}$$

where $\tilde{x}(\tau, s)$ is the transformed signal, τ is the translation parameter, which controls the locations of the Wavelet, s is the scaling parameter, which controls the width of the Wavelet, and $\psi_{s,\tau}\ (t)$ refers to a wavelet basis function at that particular scale and translation of the mother wavelet $\psi(t)$. A mother wavelet with different scaling and translation factors can generate countless daughter wavelets.

$$\psi_{s,\tau} = \frac{1}{\sqrt{s}}\ \psi\left(\frac{t-\tau}{s}\right) \tag{3.2}$$

As an illustration, Figu presents a schematic demonstrating how CWT effectively captures both the low and high-frequency components of the signal. The mother wavelet $\psi(t)$ undergoes continuous scaling (τ) and translation (s) operations, spanning the entire signal length multiple times. With each

pass of CWT, a distinct daughter wavelet (for example $\psi_{s1,\tau 1}$ *(t) and* $\psi_{s2,\tau 2}$ *(t)*)convolves with the signal, generating an array of coefficients that represent the degree of similarity between the signal and the Wavelet at that particular scale and position. This process enables the identification and localization of signal features with varying frequencies, making CWT a powerful tool for time-frequency analysis. The resulting CWT coefficients provide valuable insights into the signal's time-varying characteristics and underlying dynamics, enhancing our understanding of complex time series data (Mallat, 2009; Debnath & Shah, 2017).

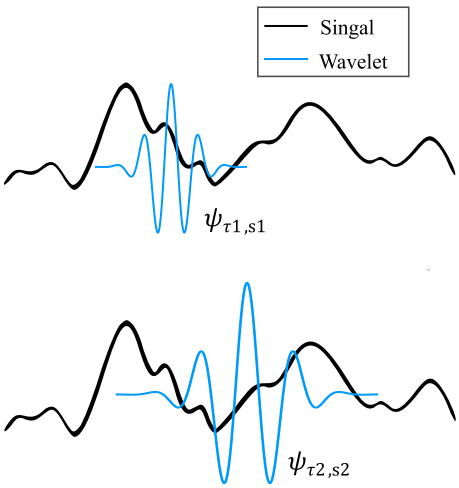

Figure 3.1 Continuous Wavelet Transform (CWT) Principle: Illustrating the CWT process involving the convolution of the Morlet wavelet with the signal at various scales and translations. In this depiction, ψs1,τ1 (t) denotes a contracted form of the mother wavelet, while ψs2,τ2 (t) corresponds to a scaled version.

The decomposed arrays of CWT coefficients represent its different constituent frequency components, while their magnitude indicates the presence of specific frequencies at different time points. Therefore, CWT coefficients provide valuable insights into the signal's time-varying characteristics and underlying dynamics, enhancing our understanding of complex time series data (Mallat, 2009; Debnath & Shah, 2017).

Many types of mother wavelets are found in the literature, each with unique advantages and applications (Misiti, 2007). For example, the Morlet wavelet utilized in this study can effectively analyze oscillatory patterns in time-series data, proving invaluable in signal processing and neuroscience, where detecting transient events and rhythmic patterns is crucial.

The CWT of a signal involves significant overlapping of wavelets at and between different scales, which results in redundant information, i.e., duplicate arrays of coefficients. The redundancy might provide high resolution but requires substantial computational resources (Addison, 2018). One solution to this problem is to use the DWT method, where the scale and translation parameters are restricted to discrete values that are $s = a_0^m$ and $\tau = nb_0a_0^m$ (a_0, $b_0 \in$ R+; m, $n \in$ Z) , respectively. The integer *m* is the resolution level of DWT, and *n* is the proportionality constant (Mallat, 2009).

Implementing discrete scale and translation parameters in Equation 3.2 yields:

$$\psi_{m,n}(t) = \frac{1}{\sqrt{a_0^m}}\,\psi\left(\frac{t - nb_0a_0^m}{a_0^m}\right) \tag{3.3}$$

For convenience, DWT is operated as low and high pass filters on a dyadic grid (a_0 =2) with a fixed-width wavelet (b_0 =1). The wavelet function $\psi(t)$ and a related scaling function, $\varphi(t)$ are defined as

$$\psi_{m,n}(t) = g_k\sqrt{2^m}\psi(2^m t - n) \tag{3.4}$$

$$\varphi_{m,n}(t) = h_k\sqrt{2^m}\psi(2^m t - n) \tag{3.5}$$

where g_k and h_k are low- and high-pass filters, respectively.

DWT provides a much more concise set of information as compared to CWT. During each DWT pass, the signal is divided into several coefficient arrays called detailed and approximation coefficients. The division is based on a cut-off frequency *fs*, which is often the most dominant frequency in the signal. The detail coefficient cD_n captures all the high-frequency components (noise) at level *n*, while the approximation coefficient comprises all the remaining high-frequency components (noise+ trend). In each successive pass, the DWT is applied on the approximation coefficient cA_n to further divide it into sub-signals cD_{n+1} and cA_{n+1}. The iterative process of signal decomposition continues until either the desired level of decomposition is achieved or the signal length can no longer be halved. The pyramid-like discretization makes DWT a more straightforward analysis than CWT (Mallat, 2009; Percival, 2008). This also enables a more accurate signal reconstruction from a given set of DWT coefficients. Based on these advantages, this study uses DWT to decompose diel streamflow signals into their temporal components to identify trends and reconstruct detrended signals.

3.3.2 Application of DWT for Trend Removal with Wavelet Thresholding:

Wavelet thresholding is utilized for distinguishing noise, including diurnal oscillations, from the streamflow recession signal in detecting diurnal oscillations. The fundamental concept behind wavelet thresholding is eliminating noise components that do not meet the specified thresholding criteria from the detail components. This process produces a reconstructed signal representing the original signal's non-oscillatory trend. By utilizing threshold-based wavelength detrending, sudden spikes and drops in the signal can be smoothed out, allowing for the extraction of time-frequency information associated with the non-oscillatory fluctuations. This helps to reveal and emphasize the underlying patterns or trends in the data while effectively isolating the diurnal oscillations from other noise sources.

In wavelet thresholding, the signal is first decomposed into its "dyadic components" and then reconstructed by applying a specific thresholding value denoted as λ. The denoising through wavelet

thresholding involves determining appropriate thresholds for each level of the time scale, typically done using a specific method. These determined thresholds are then applied with a suitable thresholding rule to remove unwanted noise from the primary signal effectively. By using this approach, wavelet thresholding can efficiently reduce noise while preserving the essential features of the original signal.

3.3.2.1 Threshold Calculation:

A threshold scheme depending on the decomposition level (Johnstone & Silverman, 1997) is employed where a unique λ_i is calculated for each detailed component based on its noise strength σ_i , and applied to each decomposition level individually.

$$\lambda_i = \sigma_i \sqrt{2.\ln(N_i)} \tag{3.6}$$

where σ is the noise strength, and N_i is the length of detailed coefficients at each resolution level i. The noise strength at each level is calculated as

$$\sigma_i = \frac{1}{0.6745} \sum_{t=1}^{N_i} |cD_i(t)| \tag{3.7}$$

The signal is then reconstructed using the list of thresholded detail coefficients. Noise is removed from all the detailed coefficients at each level. The resulting signal represents the underlying trend.

3.3.2.2 Thresholding Rules:

A threshold rule is a criterion that filters out detailed coefficients using a thresholding value λ. There are three main types of thresholding rules.

In soft thresholding, the wavelet coefficients with significant positive and negative magnitudes above λ are shrunk toward zero. The soft thresholding is given as

$$cD'_i(t) = \begin{cases} sgn(cD_i(t)) \,.\, (|cD_i(t)| - \lambda) & |cD_i(t)| > \lambda \\ 0 & |cD_i(t)| \leq \lambda \end{cases} \quad (3.8)$$

where $cD'_i(t)$ is the modified detail coefficient and *sgn(x)* is the sign function

$$sgn\,(x) = \begin{cases} 1 & x > 0 \\ 0 & x = 0 \\ -1 & x < 0 \end{cases} \quad (3.9)$$

The second thresholding rule is hard thresholding. In hard thresholding, detail coefficients whose value falls below λ are discarded immediately (Andrecut, 2019). The hard thresholding is given as

$$cD'_i(t) = \begin{cases} cD_i(t) & |cD_i(t)| > \lambda \\ 0 & |cD_i(t)| \leq \lambda \end{cases} \quad (3.10)$$

The third type of traditional thresholding rule is the non-negative garrotte thresholding.

$$cD'_i(t) = \begin{cases} cD_i(t) - \dfrac{\lambda^2}{cD_i(t)} & |cD_i(t)| > \lambda \\ 0 & |cD_i(t)| \leq \lambda \end{cases} \quad (3.11)$$

It is intermediate between hard and soft thresholding and provides a compromise between the two. It behaves like soft thresholding for values significantly above the threshold and reflects the properties of hard thresholding for low input values (Gao, 1998). All three thresholding rules are applied in the analysis to the entire set of discrete wavelet families. Figure 3.2 visually represents how the three thresholds compare using a sample array of wavelet coefficients. The thresholding is applied between -0.5 and 0.5. The thresholding rules differ in treating the input coefficients outside the specified noise range. In soft thresholding, the non-noise coefficients are shrunk to zero on either noise threshold. On the other hand, no scaling is performed in hard thresholding, and all the non-noise coefficients are kept unchanged. The Garrote thresholding provides a compromise between soft and hard thresholding. The coefficients gradually shrunk between zero and the original values as we moved from smaller to larger coefficients. The garrote offers advantages over hard and soft shrinkage, including smaller mean-square error and less sensitivity to small perturbations in the data (Fourati et al., 2005).

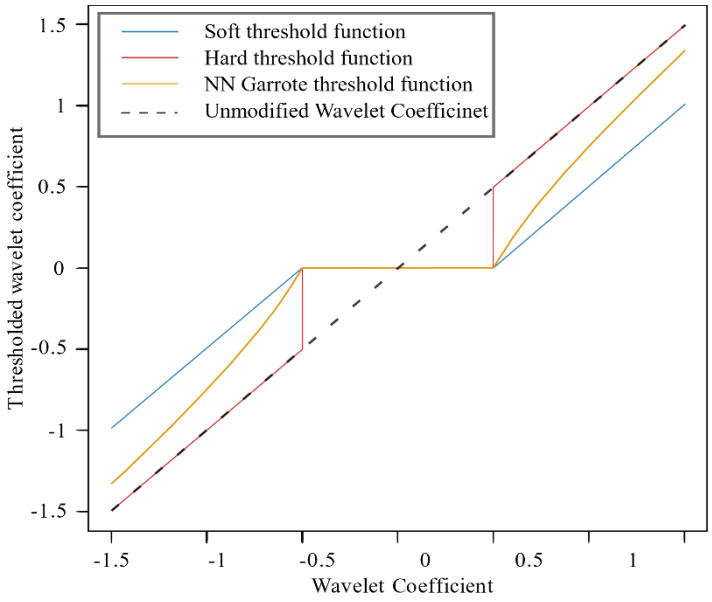

Figure 3.2 Comparative Visualization of Soft, Hard, and Garrote Thresholding Rules: The X-axis shows the input values, while the Y-axis displays the corresponding thresholded output values.

3.3.2.3 Wavelet Selection

One of the key advantages of wavelet analysis is the availability of different wavelet basis functions called mother wavelets, which can be used for various types of analysis (Daubechies, 1988; Mallat, 2009; Zeshang Yang et al., 1995). However, the output of wavelet analysis is highly dependent on the mother wavelet used, and care should be taken in choosing the appropriate wavelet.

For this study, different wavelet functions available in the Python library *pywavelets* were tested. *Pywavelets* provide extensive support for a wide range of wavelet transforms. It includes 106 pre-built wavelet functions such as Haar, Daubechies, Symlets, Coiflets, and more, with the ability to support custom wavelet functions as well. Testing a diverse range of wavelet functions ensured that the best possible combination of wavelet bases was selected with each thresholding type.

The first step is obtaining a recession signal exhibiting diurnal patterns. The diurnal signal is denoised/detrended using the moving average and the wavelet thresholding process. The thresholded wavelet coefficients are then used to reconstruct the denoised signal. The wavelet thresholding process is repeated for all the wavelet families with all three types of thresholding rules.

The main criteria for the selection of an optimal Wavelet are based on the signal and noise ratio (SNR) and the similarity of the denoised signal with a reference diurnal waveform. The SNR is calculated for each denoised signal. It serves as a crucial metric to quantify the amount of the desired signal against the noise present in the signal. A higher SNR indicates that the denoised signal has less noise and more of the desired signal. The SNR is expressed as

$$SNR = 10 \ln \frac{\sum y^2}{\sum \sqrt{y - \tilde{y}}^2} \tag{3.12}$$

where y is the original signal and $\tilde{y}$ is the denoised signal. A higher SNR value indicates a better denoising performance.

Along with SNR, quantitative indices like root mean square error (RMSE) and correlation coefficient are calculated to identify the similarity between the denoised signal and a reference diurnal signal. A lower RMSE indicates a closer match to the reference signal. RMSE is given by:

$$RMSE = \sqrt{\frac{\sum(y - \tilde{y})^2}{length(y)}} \tag{3.13}$$

The selection process is refined by introducing a Fourier Transform-based filtering step. The spectral density of the denoised signals is analysed using the Fast Fourier Transform (FFT) algorithm to find the dominant frequency in the signal, i.e., the frequency component with the highest amplitude. This step is crucial as it provides insight into the primary periodic component present in our denoised signal. The resulting FFT information is used to filter out wavelets where the dominant frequency of the denoised signal significantly differed from a diurnal frequency, i.e., 24.

Finally, the Wavelet that led to the highest SNR and the lowest RMSE post-FFT-based filtering was selected as the optimal Wavelet. The performance indices of each wavelet family are also compared against previously used detrending methods like the rolling mean to evaluate the performance of the proposed wavelet detrending method.

The abovementioned process is also shown in the flowchart in Figure 3.3. Firstly, an appropriate wavelet function is selected from the family of discrete wavelets, and the signal is detrended with wavelet detrending. Following the detrending process, the dominating frequency of the detrended signal is determined using FFT analysis. In cases where the dominant frequency is not diurnal (24-hour cycle), the detrended signal is deemed unfit and discarded. Conversely, if the signal corresponds to a diurnal attribute, it is retained for further calculations, which include SNR, RMSE, and R^2. Finally, an optimal wavelet function with the lowest SNR and RMSE values is selected, which ensures the Wavelet's denoising ability while minimising noise interference.

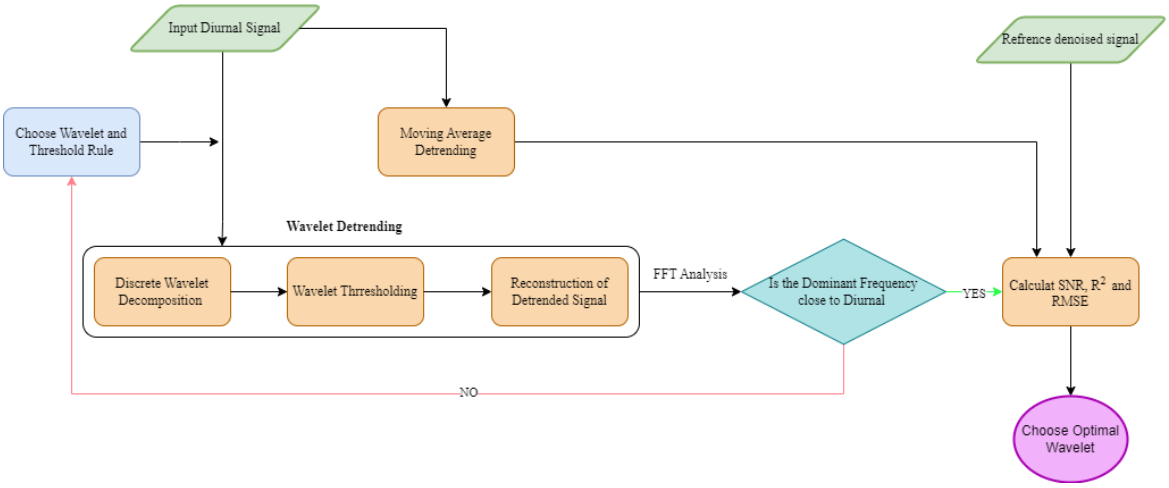

Figure 3.3 Flow chart for the selection of appropriate wavelet for optimal extraction of diel signals from synthetic sample fluctuating signals and observed streamflow.

3.3.3 Automating Extraction of Diurnal Signals Using Continuous Wavelet Transform:

3.3.3.1 Modification of DWT Process:

The detrending process from discrete wavelet transform has been shown to effectively remove noise from hydrological series and reveal the time-frequency employed to minimise these effects, but sometimes doing so produces undesirable artifacts into the decomposition and makes it difficult to accurately detrend lengthy data, primarily when the trend extends near the boundaries (Lukas et al., 2016; Mallat, 2009) However, DWT has some limitations when applied to detrend a long-term signal: (1) DWT introduces boundary effects at the edges of a times series. (2) The wavelet basis functions have limited support in time, which means they are not well-suited for modeling long-term trends (Mallat, 2009). The entire time series is divided into overlapping sections of a finite length to address these issues and make DWT work with our long-term streamflow data. The DWT coefficients are calculated on overlapping sections, and the detrended part of the section is obtained. The final detrended signal is obtained by Stitching together all the individual detrend sections. The

average is calculated at the central point. The detrending process removes the more significant frequency components associated with the trend and prepares the data nicely for a more accurate application of the continuous wavelet transform.

3.3.3.2 Extraction of Diurnal Episodes

The steps involved in the CWT extraction process are as follows:

1. The frequency range corresponding to the diel signals of interest is defined to capture the variations appropriately. Regarding diurnal fluctuations, the coefficient arrays for frequencies between 23 and 25 hours are chosen for further analysis.
2. Timestamps are identified where the magnitudes of the selected diel coefficients are the largest compared to the neighbouring noise or no-diel components.
3. These timestamps are then used to extract episodes of diurnal fluctuations from the detrended dataset.
4. Refinements are made to the extracted episodes, like removing Streamflow records exhibiting significant power spectrum distortion due to precipitation from the analysis.
5. Diurnal episodes lasting less than four days are discarded from the analysis as employed in similar studies (Sarwar et al., 2022) as an optimal minimum length to identify visible trends in the episode.
6. Diurnal episodes with peaks falling outside of the 5^{th}—95th quantiles are removed as those are associated with precipitation events and have high noise component attribution.
7. Episodes occurring during the Autumn and Winter months (April - May- June—July) are also discarded as the diurnal fluctuations in those months can not be associated with ET due to frequent precipitation and decreased temperatures.

The whole process is automated through a Python script, enabling swift extraction of diurnal signals from extensive streamflow data.

3.4 Testing of Proposed Methods

3.4.1 Hypothetical Scenario

An ideal scenario is utilized to demonstrate the performance of the proposed DWT method. A synthetic signal (S.S.) is generated based on the suggestion provided by (Kirchner et al., 2020), which represents diel fluctuations in s streamflow recession.

$$y = b^{-at} + \sin(2\pi vt) * c^{-at} + noise \quad (3.14)$$

where a is the recession constant, b is initial streamflow, c is the diel amplitude, and noise is a signal having a standard normal distribution with an average of 0 and a standard deviation of 1 (also known as Gaussian white noise). The noise function with $\mu = 0$ and $\sigma = 1$ is

$$p(x) = \frac{1}{\sqrt{2\pi}} e^{-x^2/2} \quad (3.15)$$

The synthetic signal includes a known trend and a noise component, which can help compare the denoising capabilities of different wavelet functions and enable us to compare the results of DWT with previously applied detrending methods like the moving average. In addition to the sample signal described, one real-life streamflow signal (RS) is analyzed using the proposed method.

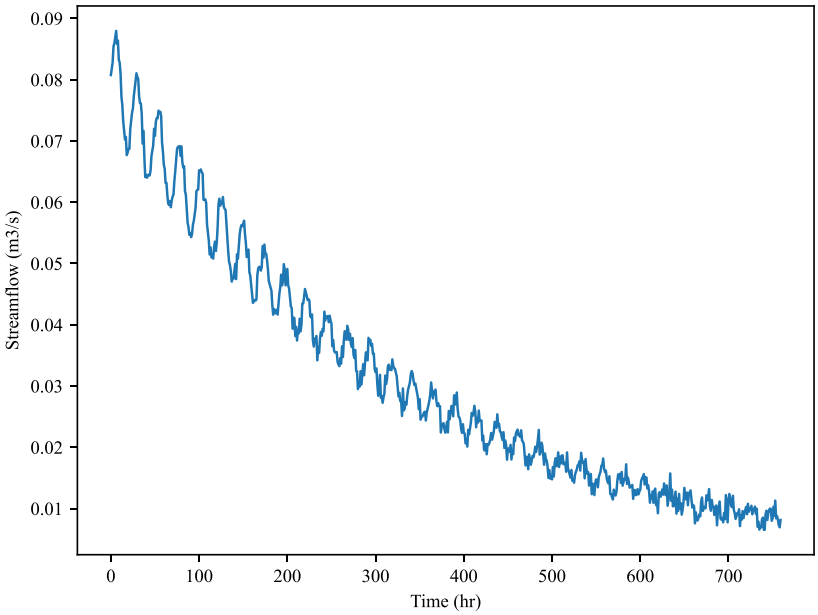

Figure 3.4 Synthetic flood recession with daily fluctuations when a = 0.003, b = 0.08, and c = 0.008

3.4.2 Real streamflow scenario

Hourly streamflow data from the Toenepi stream in Waikato, New Zealand, is applied to investigate the application of W.A. on Streamflow daily fluctuations. The Toenepi stream (WGS84 coordinates: -37.7146, 175.5632) drains a small catchment in the Waikato region, New Zealand. The catchment has an area of 1.6 ha and an elevation range from 40 to 130 m above mean sea level. The sub-catchment is a headwater catchment, with a flat (max slope 6.5%) and fully covered by pasture apart from the riparian plantings around the Toenepi stream, mainly consisting of shading trees and shrubs (Wilcock et al., 2009). There is adequate vegetation along the stream route and a moderately well-drained aquifer. The catchment showed daily fluctuations in the streamflow recessions, particularly in warmer months (Sarwar et al., 2022).

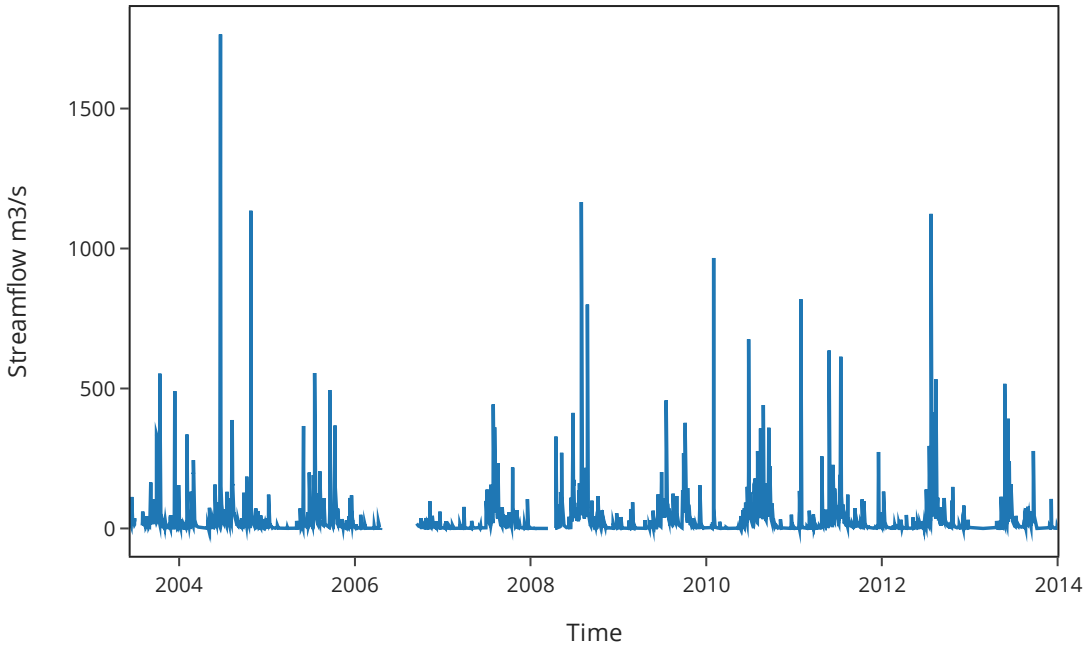

Figure 3.5 Hourly streamflow series for Toenepi, Waikato.

The process is first applied to a single summer recession to compare the detrending performance of methods like DWT and moving average (Figure 3.6). The recession is selected to represent the typical characteristics and fluctuation patterns found in the original extended dataset. After determining the best-performing wavelet for the single summer recession, the detrending method is scaled to the entire dataset. This involves applying the modified DWT or process for the whole dataset to perform a comprehensive detrending.

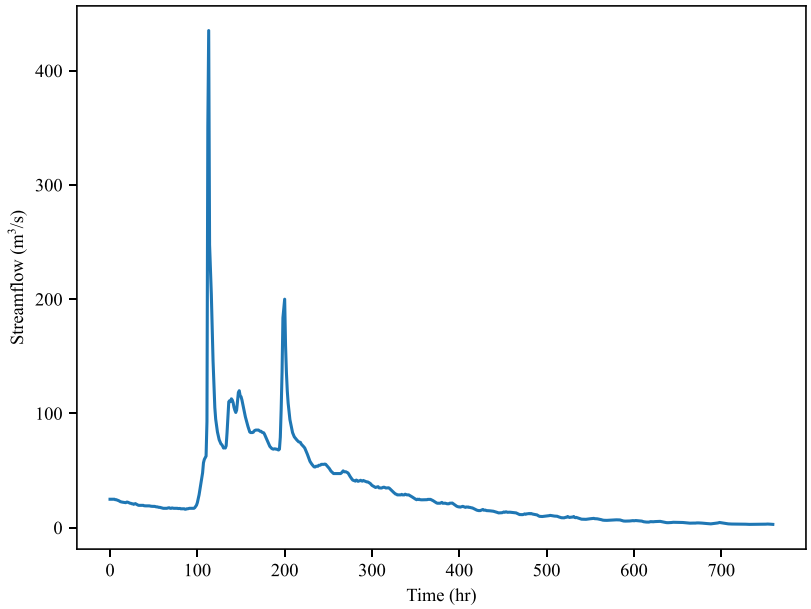

Figure 3.6 Streamflow signal from Toenepi showing diurnal fluctuations.

3.5 Results and Discussion:

3.5.1 DWT Detrending

3.5.1.1 Wavelet Decomposition:

Figure 3.7 and Figure 3.8 show the decomposition process of the synthetic signal S1 and observed streamflow R1, respectively. The DWT decomposition of the synthetic signal is further detailed to show the division of the parent signal into detail and the approximation sub-signals at each decomposition level. The approximation coefficient results from low-pass filtering and represents information on all the low-frequency components at each level. For example, at level 1, the scale is set as $2^1 = 2$, and the frequency content is halved fs/2. The approximation coefficient, cA1, represents a smooth version of the signal and contains all the components with a frequency range of (fs/2 → 0). Similarly, the approximation coefficient at the last decomposition contains the slowest-moving components (trend) of the original signal with a frequency range of (fs/32 → 0). In conclusion,

pyramid-like decomposition provides a multiresolution analysis of a signal, allowing for the examination of its frequency content at different scales.

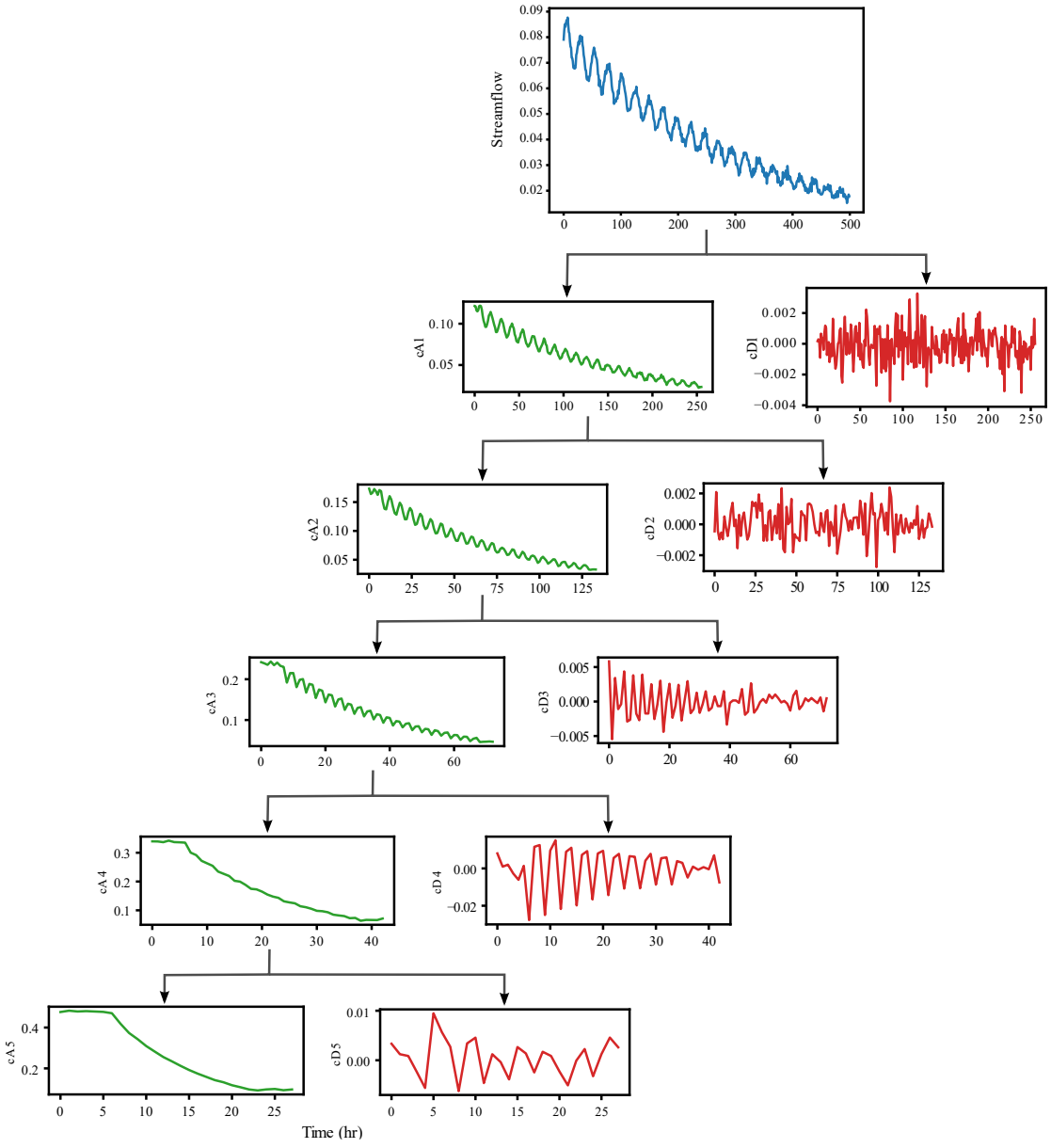

Figure 3.7 DWT workflow for the synthetic diel signal. The original signal is decomposed into a pair of detail and approximation coefficients. The approximation coefficient then undergoes further vision at each level, revealing the finest details in the signal.

DWT workflow for the synthetic diel signal. The original signal is decomposed into a pair of detail and approximation coefficients. The approximation coefficient then undergoes further vision at each level, revealing the finest details in the signal.

For the actual streamflow signal, the DWT plots using the wavelet "bior6.8" are shown in Figure 3.8. The DWT results in five decomposition levels, each representing the signal attributes at a different resolution scale. The separation into multiple resolution levels is crucial in revealing the significant changes in non-stationary signals like streamflow—the abrupt changes in the detailed coefficients correspond to the rapid changes in the streamflow due to the sudden precipitation events. As we move upward in the decomposition levels, the detailed coefficients become more refined, locating short-term signal variations. On the other hand, the approximation coefficient is smooth and captures the long-term pattern or trends in the streamflow signal.

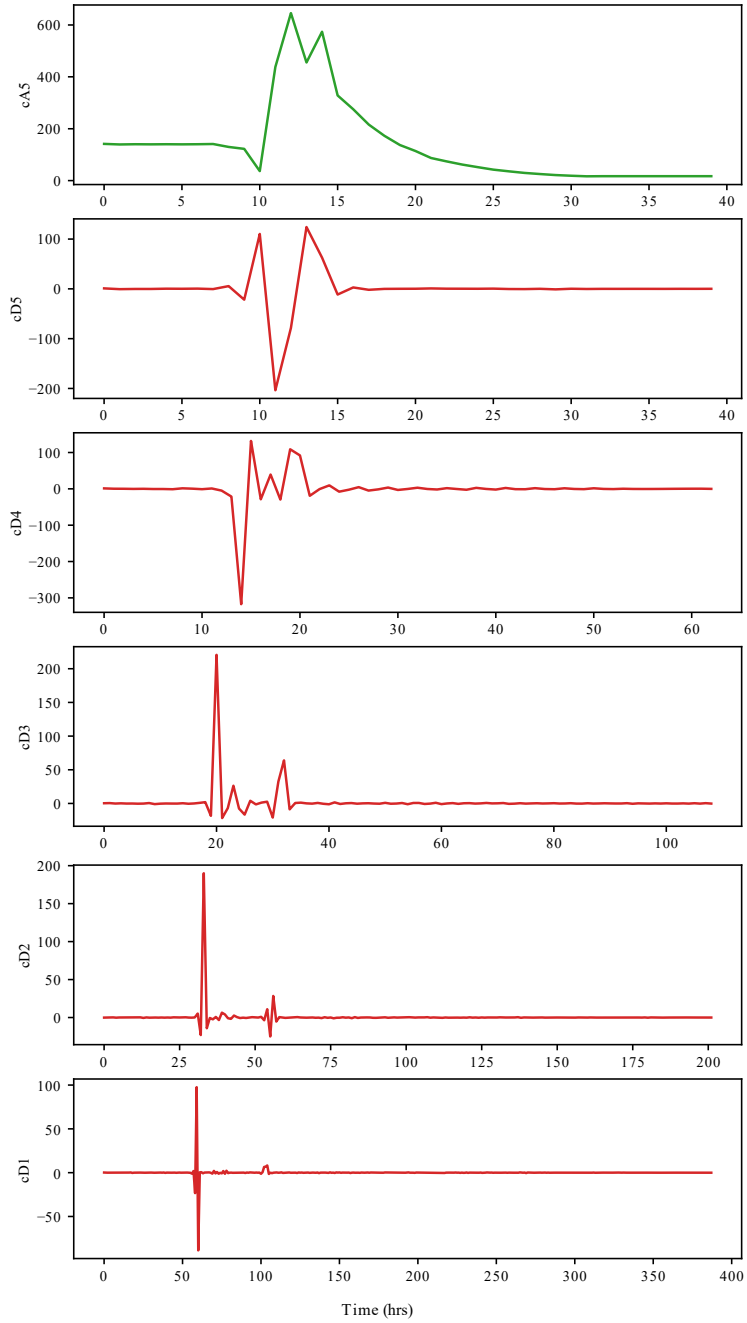

Figure 3.8 The maximum level DWT decomposition of the real-life observed streamflow. The detailed coefficients represent the noise or short-term fluctuations at each level, while the approximation coefficients exhibit the long-term trend in the signal.

3.5.1.2 Wavelet Shrinkage:

The detailed coefficients from DWT are then subjected to wavelet thresholding (Figure 3.9). The thresholding process converts the original coefficient array into modified coefficient arrays. The

detail coefficients whose values do not meet the threshold criteria are truncated. The threshold adjustment is more frequent at higher frequency levels, where almost 95% of the values become zero.

DWT decomposes the hourly streamflow data containing at least one recession event into four lower-resolution levels. The detail components denoted from cD1 to cD4 represent the sub-signals having a period of 2hr to 32hr, respectively, with the periods increasing as we move down the resolution level. Hence, the detailed components at lower resolution levels have lower frequencies than those at higher decomposition levels. The approximation coefficient cA4 represents the signal's slowest changing component at the sixth decomposition level. There is a sharp rise in the magnitudes of coefficients around the time of the peak flow, representing the magnitudes of high-frequency noises associated with the peak flow event.

Figure 3.9 also shows the inverse DWT process, where the trend is reconstructed from the modified set of detail coefficients. A sub-signal of the primary signal is obtained using the *waverec* command in the pywt python module. The reconstructed signal is free from all the high-frequency noise components and represents the underlying trend of the primary signal. A detrended signal is then obtained by subtracting the trend from the primary signal.

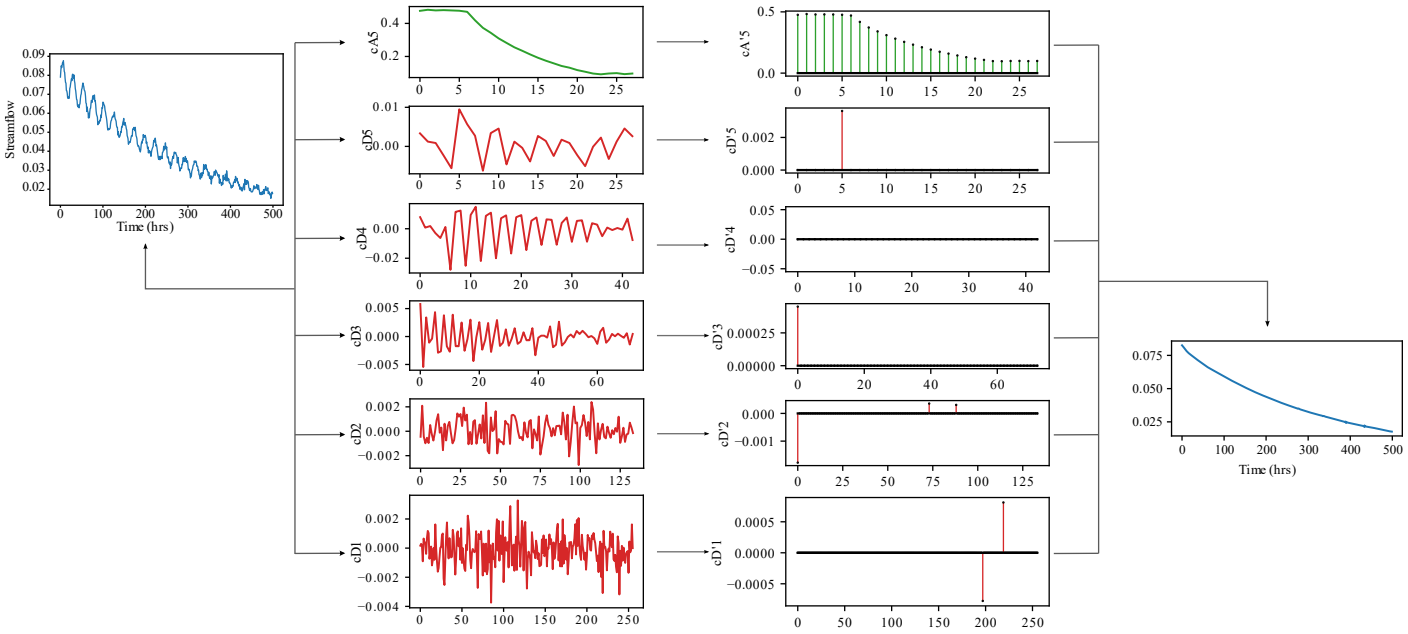

Figure 3.9 Wavelet-aided thresholding to denoise each decomposed coefficient of the signal, followed by the reconstruction of the denoised signal representing the underlying trend.

Likewise, the following stem plots (Figure 3.10) show wavelet thresholding results for the four decomposition levels of Coif 5 using the Garrotte threshold rule. The left column shows the log values of the unmodified detailed coefficients, while the right column has threshold-adjusted values against the corresponding resolution level. The stem plots provide a visual representation of the thresholding process. In these plots, the retained coefficients in the right column indicate parts of the signal that are believed to contain essential information, while the eliminated coefficients in the left column signify areas deemed to contain noise. The approximation coefficient is left unchanged as it is believed to contain only the trend information. The resulting thresholded coefficients then be joined with the approximation coefficient to obtain the denoised signal representing the underlying trend of the primary signal.

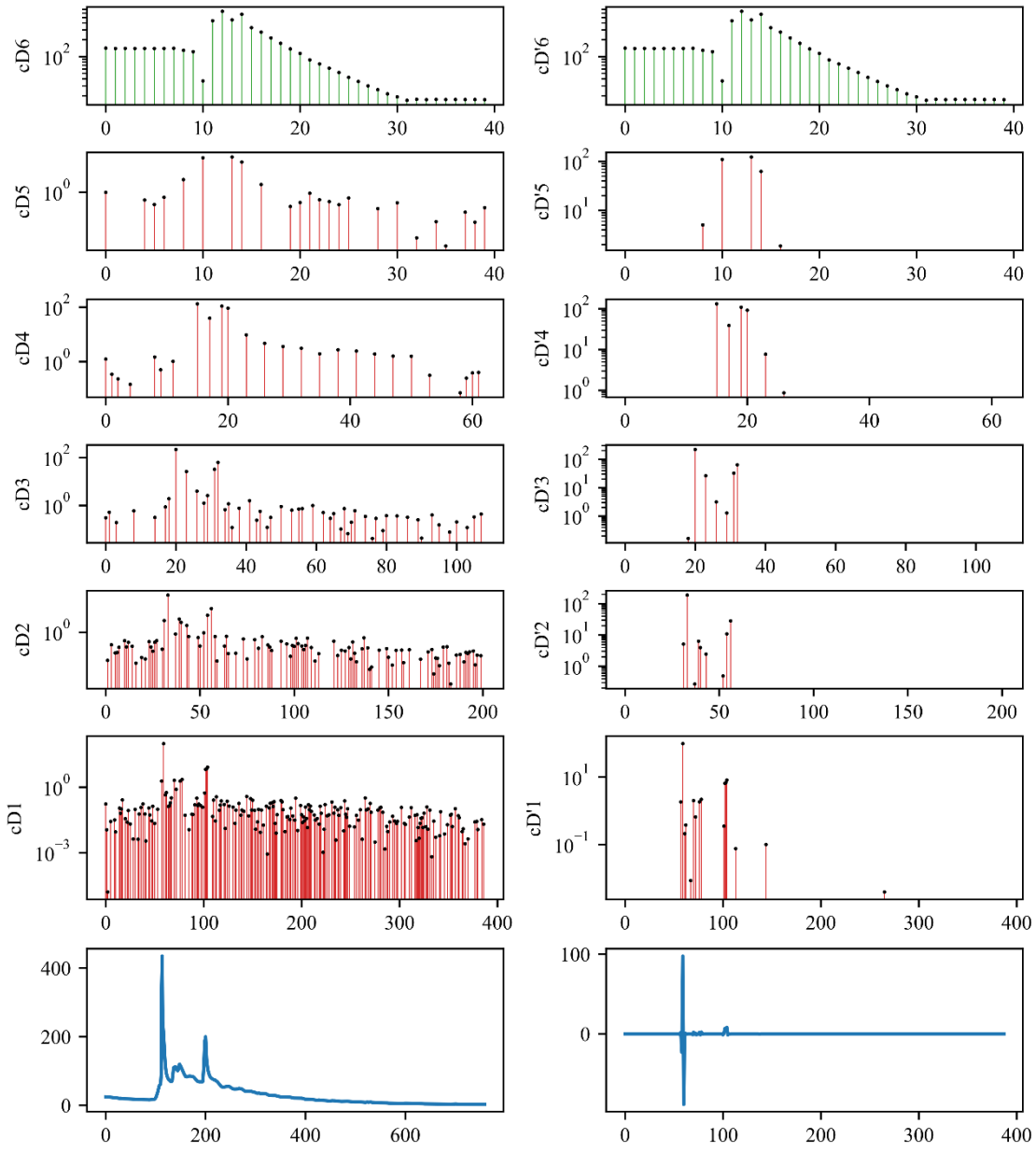

Figure 3.10 Amplitudes of the DWT coefficients of the observedstreamflow signal (left) and the threshold adjusted coefficients(right)

Adjusting the thresholding criteria can tweak the stemplots. The threshold criteria work as a trade-off between noise reduction and the preservation of signal details and depend on the type of application. The selection of optimal wavelet type and thresholding criteria can ensure a more efficient denoising process, resulting in a cleaner, clearer signal with the essential features intact.

Finally, the trend is reconstructed from these thresholded arrays of coefficients. The detrending results from the wavelet threshold method and the moving average are shown in Figure 3.11. The wavelet trend can better follow the sudden spikes in the signal due to the peak magnitudes retained in the threshold-adjusted detail coefficients.

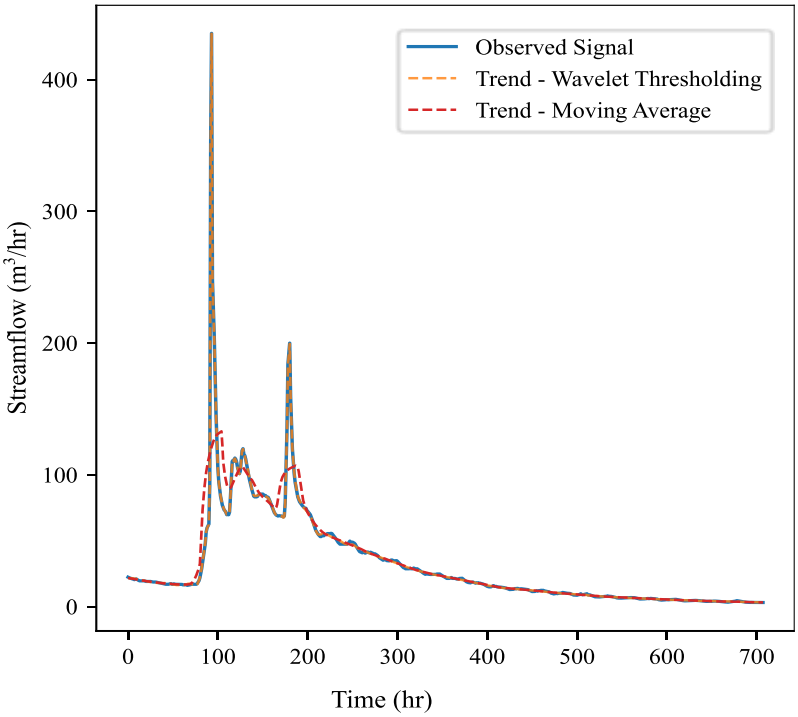

Figure 3.11 Comparison between detrended signals using wavelet threshold and moving average methods.

3.5.1.3 Wavelet Selection:

Wavelet analysis, which consists of wavelet decomposition and thresholding, is performed for each mother wavelet of the discrete Wavelet family and against all three thresholding rules. The Table 3.1 This chart shows the coefficient of correlation (R^2), SNR, and RMSE values for the moving average and the three best-performing Wavelets against all the threshold types.

The SNR and correlation analysis for SS reveal that DWT showed similar denoising performance to the moving average for extracting the diurnal fluctuations from a recession. The sym15 Wavelet

with the hard thresholding had the highest correlation and SNR values. The detailed WA for the sym15 wavelet is presented in the following sections.

For the signal R1, the moving average method performed poorly, with an R^2 close to zero, high MSRE, and a low SNR value, indicating poor correlation with the original signal, high error, and low signal-to-noise quality. In contrast, the DWT denoising showed significantly better results. For instance, the 'bior6.8' Wavelet with the 'garrotte' threshold delivered an R2 of 0.3477, an MSRE of 0.5002, and an SNR of 91.6488, substantially improving the moving average method. This demonstrates the effectiveness of DWT in handling more complex, noisy signals compared to traditional smoothing methods like the moving average. The moving average might be most suitable for stationary signals where the underlying trend remains relatively constant. The moving average may not effectively remove the high-frequency components if the signal exhibits non-stationarity, such as the non-stationary trends introduced by the precipitation events in the baseflow time series.

In summary, the DWT denoising method offers a competitive, and sometimes superior, alternative to the moving average for denoising streamflow signals. However, the DWT results heavily depend on the choice of the best wavelet and thresholding method for the signal's specific characteristics.

Table 3.1 R^2, MRSE, and SNR values for SS and the best-performing wavelet basis function

Signal	**Wavelet**	**Threshold**	**R^2**	**MSRE**	**SNR**
SS	Moving Average		0.9996	0.0015	68.53
	sym15	soft	0.9994	0.0017	65.88
	sym15	hard	0.9963	0.0015	68.50
	sym15	garrotte	0.9991	0.0017	66.75
RS	Moving Average		0.0009	18.59	19.35
	coif8	soft	0.1166	0.7698	83.03
	coif8	hard	0.1166	0.7698	83.03
	bior6.8	garrotte	0.3477	0.5002	91.65

It may be noted that similarity (R^2 and RMSE) calculations for synthetic and observed streamflow signals are conducted against different reference signals due to the inherent uncertainty associated with the actual trend in the observed streamflow data, which is unknown at the time of analysis. The similarity between the artificially introduced sample diurnal fluctuations and the detrended signal obtained through wavelet analysis and moving average techniques is computed for synthetic signals.

Alternatively, the similarity is computed between the detrended signals and the corresponding lagged potential evapotranspiration (PET) for the observed streamflow. The lagged PET signal is used here as a reference because the diurnal fluctuations are closely related to ET or PET through a specific lag time (Sarwar et al., 2022). This distinction in correlation calculation between synthetic

and natural streamflow is critical and reflects real-world data analysis's unique nature and challenges. However, SNR alone can be considered adequate in the absence of a reference denoised signal like PET.

3.5.2 CWT Analysis

3.5.2.1 Wavelet Power Spectrums

The CWT analysis presents us with multiple graphs, which can help us identify the frequencies and times where the diurnal fluctuations were present in the primary signal. The typical CWT analysis of the observed streamflow signal is presented in Figure 3.12

The parameters for the continuous wavelet analysis are adopted from (Torrence & Compo, 1998) set as $\delta t = 1$ hour since our data is hourly distributed. The first scale, *SS*, is 2 hours because $s = 2\delta t$ and $\delta j = 0.25$ to do 4 sub-octaves per octave (scale level). Moreover, j equals 11 to plot the graph to up to eleven powers of two.

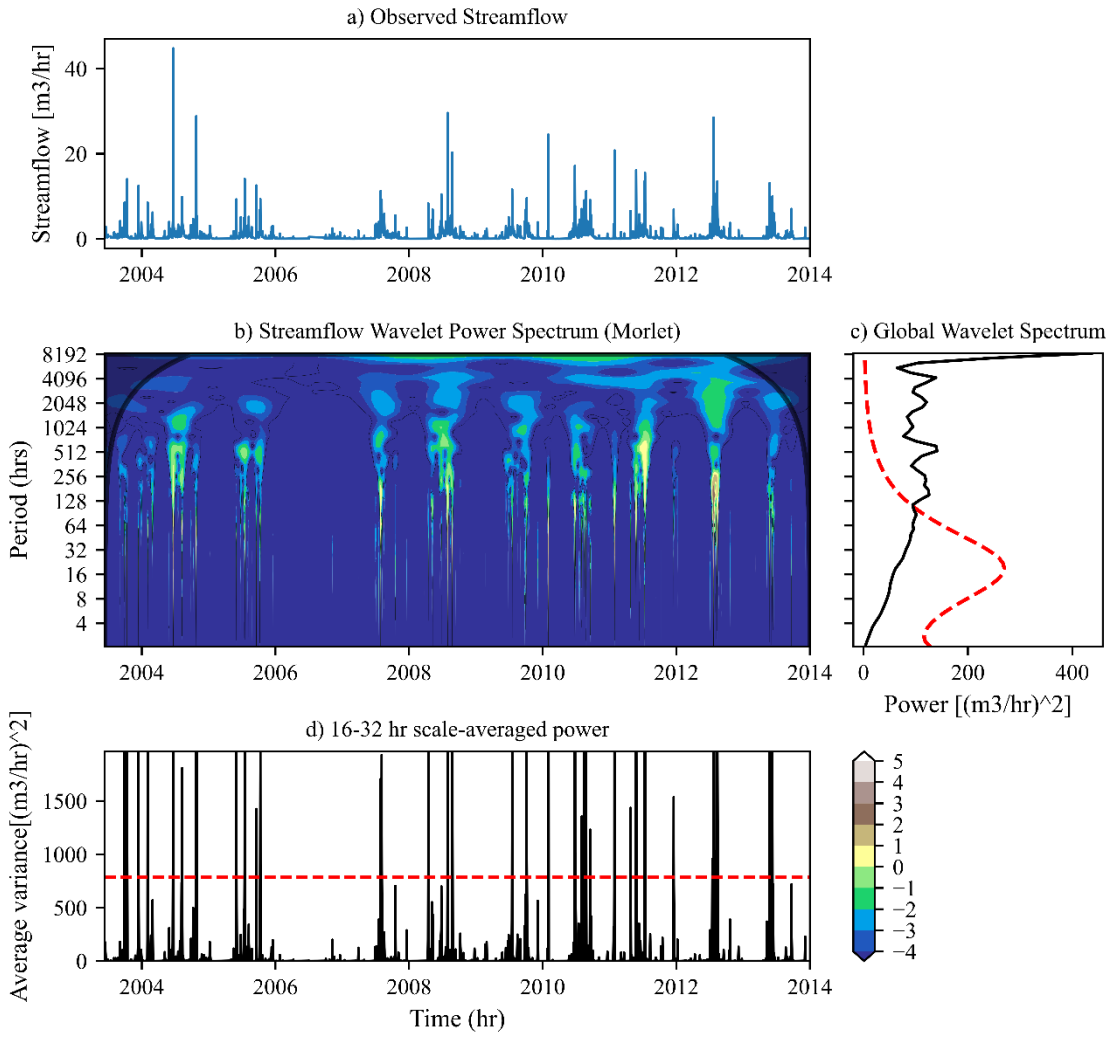

Figure 3.12 CWT analysis of the observed streamflow time series. The time series and wavelet power spectra are shown in (a) and (b). The scalogram represents the strength of power (log_2) in the contour image in (b). Fig(c) shows the global wavelet spectrum with a 95% significance line in the red dotted line. Figure (d) represents a 16-32 hr. scaled average wavelet with a 95% significance line.

The first plot (Figure 3.12b) shows the wavelet transform's power (absolute value squared) for the hourly detrended streamflow at different scales and times. The power is represented by a color scale, with higher power areas being more yellow, while lower wavelet powers scale towards blue. The red contours correspond to the 95% significance level drawn against a red noise background spectrum. The red noise corresponds to the signal's autocorrelation with a lagged-1 version of itself

and represents the expected power at each frequency in the absence of any accurate signal. (Torrence & Compo, 1998).

$$x_n = \alpha x_{n-1} + z_n \tag{3.16}$$

where α is the lag-1 autocorrelation of the time series, and z_n is Gaussian white noise.

The shaded region is the cone of influence, inside which the distortion due to edge effects is significant. Because of zero padding, these edge effects occur at the wavelet spectrum's beginning and end.

The second CWT plot (Figure 3.12c) shows the global wavelet spectrum (GWS), which is a helpful tool for determining the most dominant frequency in the primary signal. It is constructed by integrating the wavelet power spectrum across all time points for each scale. The peaks in the GWS correspond to the scales at which the signal has the most power or energy. GWS can also be used for significance testing, where the GWS is compared against a specified background noise model. In Figure 3(c), the red line represents the 95% significance level against a red-noise background spectrum.

The third CWT plot (Figure 3.12d) shows the scale average variance (SAV), which measures the strength of signal fluctuations over a specified range of scales. It is obtained by averaging the CWT power spectrum across various scales of interest. It can help identify times of particularly strong or weak fluctuations in the signal over the range. The scaled-powered average's statistical significance is also assessed by comparing it against a 95% confidence level. Both the wavelet power spectrum and the scaled power average are used to identify and filter the timestamps of significant noise in the signal.

3.5.2.2 CWT Analysis of Detrended Signals

(a) Moving Average

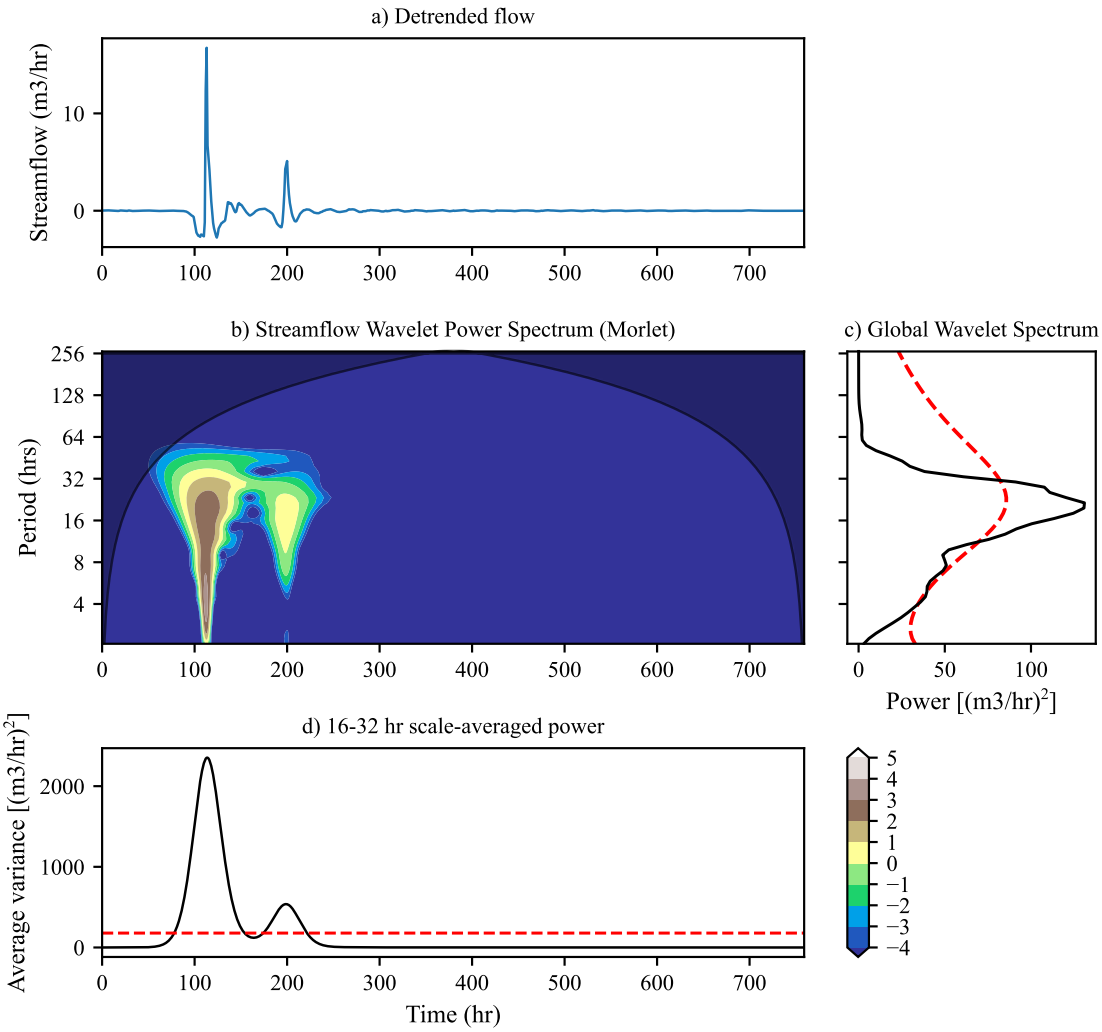

Figure 3.13 CWT of the moving average detrended signal

Figure 3.13b shows the wavelet transform's power (absolute value squared) for the hourly streamflow at different scales and times. As can be seen from Figure 3.13b, due to incomplete detrending, the moving average produces an undesirable boost in power for certain regions while other regions get attenuated in the wavelet spectrum.

The global wavelet power of the moving average-detrended signal (Figure 3.13c) has a huge peak amplitude, which masks the peaks of higher frequencies. Although the peak is observed in the diel

region, it has a broad base and is intersected by the 95% significance level line in the global wavelet power plot.

The SAV subplot (Figure 3.13d) shows the time series of the average signal variance inside the diurnal frequency range. The time series for the 16-32 hr scaled averaged power has two statistically significant peaks corresponding to the two power concentrated regions in the wavelet power spectrum. In contrast, the average variance for the rest of the region stays below the significance level, which tells us very little about the evolution of the diurnal signal with time.

(b) Wavelet Detrending

The "bior 6.8" wavelet is chosen for the detrending purpose, with a decomposition level of 4. The garrote threshold rule is used to remove noise in each decomposition level. The combination of wavelet type and threshold rule has been seen to perform best when detrending the real-life observed streamflow signals to extract diurnal fluctuation. Represents the wavelet scalogram of the thresholded detrended signal.

A good spread of wavelet power across the entire series length shows the ability of the wavelet threshold algorithm to extract diel signals from non-stationary streamflow data sets having precipitation events. The global wavelet power (Figure 3.14b) has a sharp peak concentrated in the diel region, and its magnitude goes well above the 95% confidence level. This peak represents the strength of diel oscillations in the signal. The GWS (Figure 3.14c) of the wavelet-aided detrended signal has a minimal peak amplitude compared to the moving average, which again shows the DWT method's better detrending performance for extracting diurnal fluctuations.

The SAV plot (Figure 3.14d) for the 16-32 hrs band remains above the 5% significant levels, representing the strength of the diel fluctuations in those regions. The time series of scaled average variance shows the temporal location of the events, which are responsible for the peaks shown in the global power spectrum. Moreover, the decay in the diel signal peaks is replicated in the scaled average variance for the 16 -32 hr band for the wavelet-aided detrended signal. On the time series

of scaled average time series, there is a rise in the variance at the time of the rainfall event, whereas the variance throughout the signal remains significant. In conclusion, the continuous wavelet analysis of the wavelet-detrended signal shows improved results where a power concentrated spread uniformly across the length of the data set. The scaled average variance also shows an excellent distribution above the significance level.

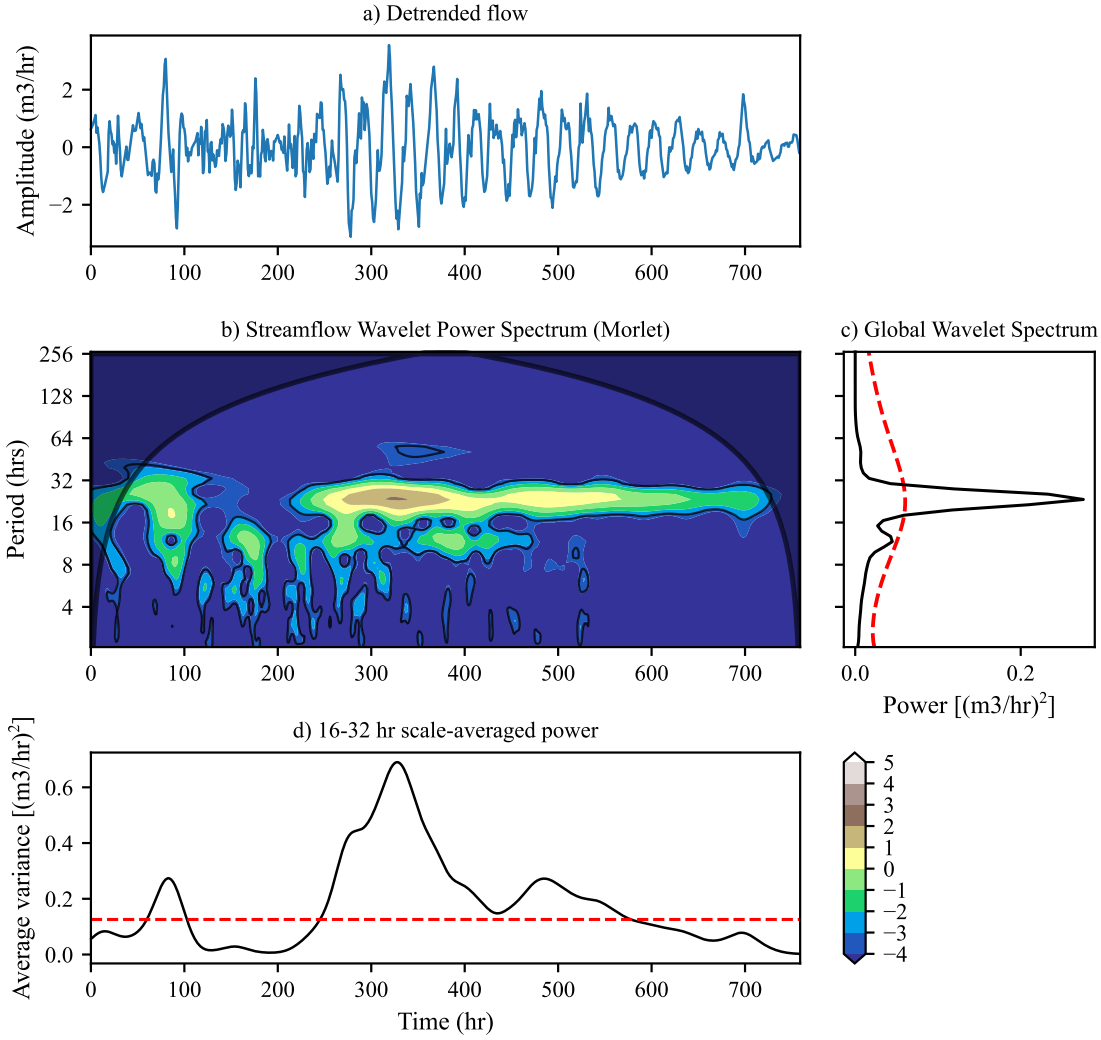

Figure 3.14 CWT of the detrended signal via wavelet-aided thresholding

3.5.3 Extraction of diurnal episodes

The CWT plots of the detrended signals give us a deeper insight into the variability in the power and variance of diel fluctuations inside the signal and help extract diurnal episodes from the signal. The extracted diurnal signals are also subjected to the prescribed filtering criteria, followed by manual inspection.

Finally, the extracted signals are validated by comparing them with the manually identified diurnal episodes in the same data set by Sarwar et al. (2022).

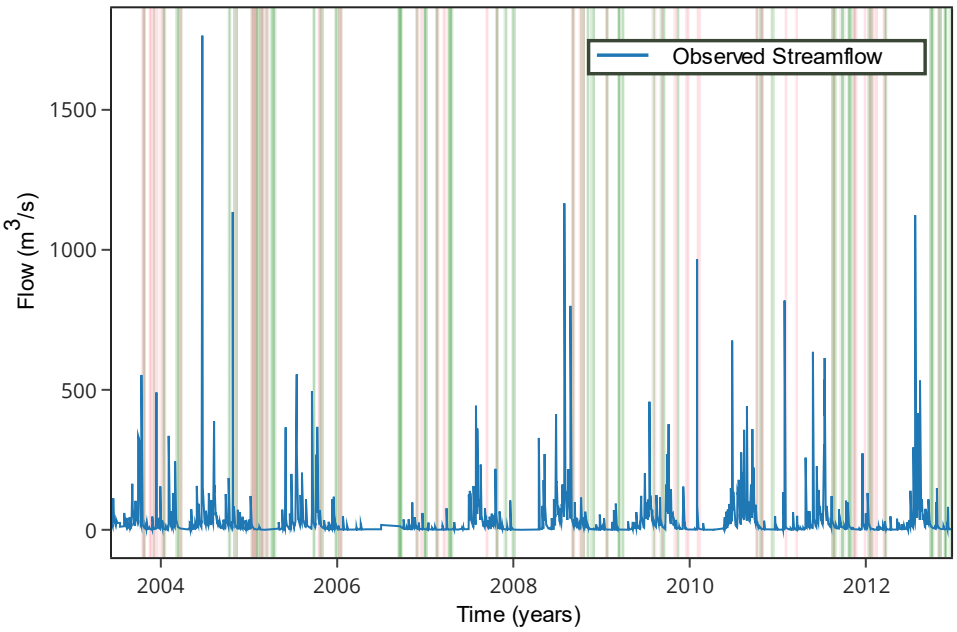

Figure 3.15 Comparison of the diurnal episodes: manually extracted (Pink Bars) vs. the CWT method (Green Bars)

The comparison reveals that the diurnal episodes extracted through CWT analysis overlap the manually extracted signals on several occasions (27/41); however, there are instances where the diurnal episodes differ.

There could be several reasons accounting for this observed discrepancy. Firstly, it's crucial to recognize that the extraction criteria employed in the CWT method are explicitly defined to isolate

proper diurnal fluctuations. Specifically, the dominant frequency sought in these episodes is either 24 hours or very close to it. However, during the manual extraction process, it was observed that many diurnal episodes exhibited a complex diurnal nature and contained other dominant harmonic frequencies. These additional harmonic frequencies can significantly distort or even overlay the underlying diurnal fluctuation pattern. As a result, this interference can compromise the CWT method's ability to accurately distinguish the diurnal component, potentially leading to a failure in predicting diurnal fluctuations at those timestamps.

Secondly, it's worth considering the CWT method's frequency resolution. Although different frequency resolutions are tested to optimize the extraction process, they may not always be sufficient to effectively separate closely spaced harmonic frequencies from the diurnal frequency, especially when these harmonics fall within the range of the diurnal frequency itself.

Despite these differences and challenges, it's important to highlight that the proposed CWT method still successfully extracted a reasonable number of diurnal episodes. It even revealed diurnal oscillations where the manual extraction method failed, possibly due to oversight or other limitations.

Overall, this comparison underscores the complexities of analysing diurnal fluctuations and the importance of considering various factors, including harmonic frequencies and frequency resolution, when employing different extraction methods. It also highlights the complementary nature of the CWT method, which can uncover diurnal patterns that may go unnoticed through manual extraction alone.

3.5.4 Comparison with FFT analysis

The CWT method is also evaluated against the traditional FFT for detecting diel signals from streamflow data. FFT transforms data into the frequency domain, identifying dominant frequencies through power spectral density (PSD) peaks. In the case of a diurnal signal, the desired frequency is 1/24, or 1 cycles per day.

The data is divided into smaller segments of 5 days long, and each segment is shifted forward by 1 day to create the next episode. FFT is then applied to each window, and if four consecutive windows show a dominant frequency corresponding to the diel signal, the entire segment is classified as containing a diel signal. The diel identifications are presented in Figure 3.16.

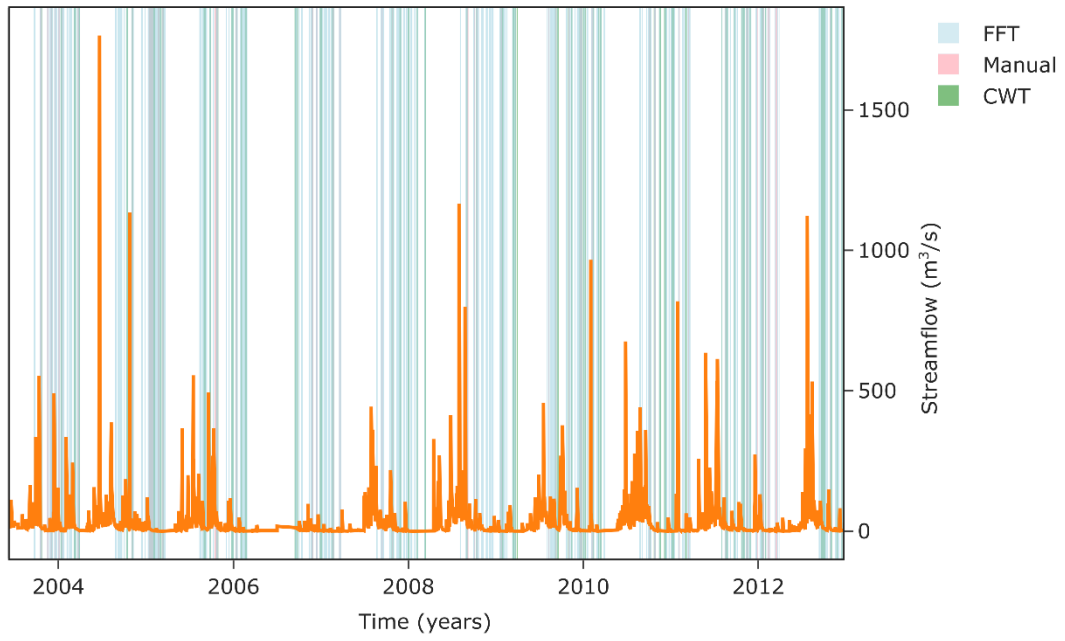

Figure 3.16 Comparison of diurnal episodes extracted from FFT , CWT and manual identification.

While the Fast Fourier Transform (FFT) segments matched the Wavelet Transform (WT) results in multiple locations, they produced numerous false positives (Figure 3.17). The dominant frequency within each FFT window often corresponded to diel signals. However, these signals were not consistently present throughout each day within the window. Additionally, in regions with pronounced peaks and deep troughs in the signal, FFT frequently mislabeled windows as diel. This occurred because the PSD value for the diel period was highest, even when noise or other frequencies significantly influenced the spectrum. Figure 3.18 shows the PSD graph of a noisy episode. Due to noise distortion in the signals, a few different signals show a high strength within 70% of the peak. Consequently, the FFT method sometimes struggles to differentiate between true diel signals and artefacts caused by noise or other periodic influences.

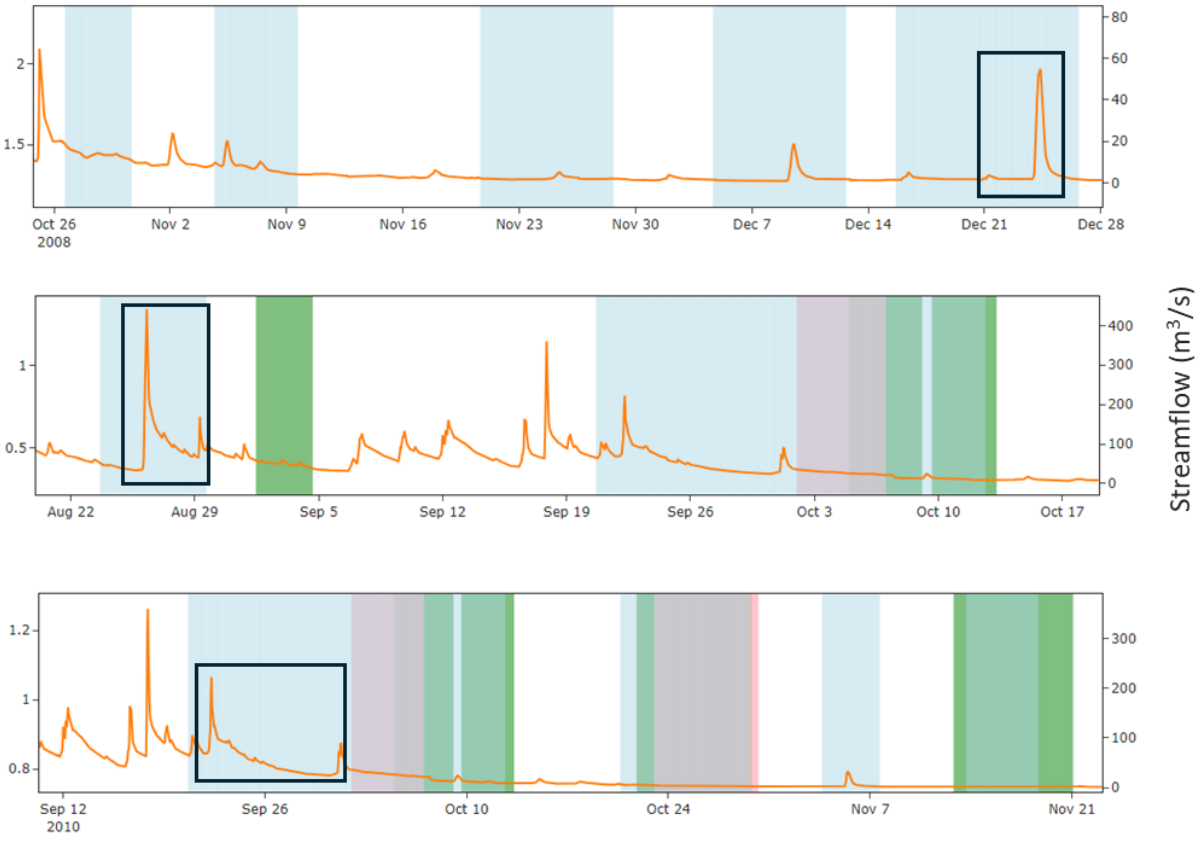

Figure 3.17 Examples of false identification of diel segments in FFT.

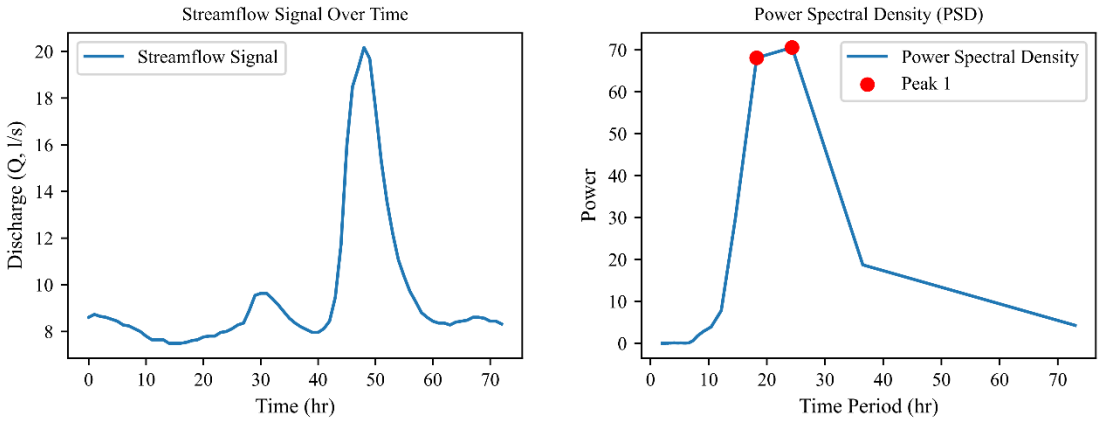

Figure 3.18 The PSD graph of a streamflow segment (2008-11-03: 2008-11-06) shows different frequencies of significant strength, causing a false identification of the diel episode in FFT.

FFT struggled to localise diel frequencies accurately, making it impossible to extract precise timestamps when the diel signal was most prominent. The fixed window approach of FFT limits its effectiveness with non-stationary data, where equally strengthed PSD peaks—such as diel signals

mixed with noise—often lead to errors. Its lack of time-domain information further prevents tracking variations in diel signal strength over time. These shortcomings reduce FFT's reliability in distinguishing diel signals from noise. In contrast, WT offers better temporal resolution and accuracy, making it more suitable for analysing dynamic and complex signals like streamflow data.

3.6 Conclusion:

Wavelet analysis is used in this paper to extract and analyse diel fluctuation from a streamflow signal. A detrending scheme based on wavelet-aided thresholds is used to extract dial signals from streamflow sessions and a workflow to choose the best Wavelet. The wavelet-aided threshold method was also pitted against the most widely used moving average method. Based on the comparison with the moving average and the results of the CWT, it was seen that the W.A. detrending scheme was better able to follow sudden peaks in the stream flow and that the detrended data had a more uniform power spectrum as compared to the detrain did signal obtained from moving average. The global wavelet spectrums also provided wavelet powers of the detrended signals against mean that noise spectrum. Lastly, the scale average time series of the average variance of the signal provided the temporal distribution of variance inside a specific frequency band. They helped identify the exact timestamps of the event carrying the most variance in the frequency band.

Chapter 4. Investigating Seasonal and Spatial Variations in Diurnal Streamflow Fluctuations and Their Correlation with Catchment Attributes

Abstract

Diurnal streamflow patterns within a catchment reflect the complex interplay of topography, land cover, and climate systems, influencing both short-term and long-term hydrological behaviours. Wavelet transform has been applied to extract and analyse diurnal fluctuation episodes from long-term hydrological records from various regions in New Zealand, ranging from generally warmer and more humid in the North to cooler and more variable climates in the South, with alpine landscapes The diurnal features, namely diurnal amplitude, and lag, are compared with different catchment features, representing catchment and drainage network shapes and sizes. The results showed positive correlations of diurnal features with the different shape and size parameters. The climate of catchments also played a role in controlling the temporal connection between vegetation activity and catchment response. In general, the catchment with the warmer climate and more circular geometries

showed longer and higher response times than the catchment with cooler temperatures and more elongated shapes.

4.1 Introduction

Quantifying the hydrologic response of a catchment is critical for effective water management. Hydrologists can assess the impacts of climate and other induced changes on a catchment and forecast catchment behaviour by analysing different hydrologic patterns showing overall catchment hydrologic response (Kirchner, 2009; Mlamla et al., 2022). These hydrologic signatures help quantify the catchment response and include variables like surface runoff, evapotranspiration, groundwater storage, snowmelt, and baseflow index, among others (H. K. McMillan et al., 2022). Each signature provides a unique perspective on different hydrological processes and catchment characteristics.

Diurnal fluctuations in streamflow are critical hydrologic patterns that can reveal key catchment characteristics (Gribovszki, Kalicz, Kucsara, et al., 2008). Diurnal fluctuations in streamflow refer to the daily variations in a stream's flow rate or discharge. These fluctuations often exhibit a distinct diurnal pattern, characterised by regular rising and falling flow rates over a day following the diurnal variation in solar radiation or ET (Lundquist & Cayan, 2002). However, the diurnal shape has been observed to vary based on the location of the fluctuation of the falling hydrograph (Sarwar et al., 2022).

The transpiration activities of riparian vegetation primarily drive the diurnal signature in non-snow catchments and depend on various physical and hydrological factors within a catchment (Bren, 1997; Graham et al., 2013; Sarwar et al., 2022; Szilágyi et al., 2008; White, 1932). Černohous & Šach, (2008) observed that in a small experimental forest catchment, during rainless periods, the decrease in streamflow during the daytime compared to nighttime was primarily attributed to forest evapotranspiration. Alternatively, Mutzner et al., (2015) found that evapotranspiration-induced diurnal streamflow cycles can occur in alpine catchments alongside snowmelt or ice melt cycles.

4.1.1 Characteristics of Diurnal Features

This study focuses on the two main features of diurnal streamflow signals: amplitude and timing of the diurnal maximum and minimum. The diurnal amplitude has been defined as half of the difference between the highest and lowest streamflow values observed within 24 hours (Czikowsky & Fitzjarrald, 2004). The amplitude variations of diurnal streamflow fluctuations provide valuable insights into catchment behaviour and water storage. Studying these fluctuations can also help estimate riparian zone evapotranspiration.

The second diurnal attribute is the time lag between the timings of the diurnal minimum and the maximum transpiration of riparian plants. The time lag helps us understand the role of riparian water uptake in the overall water balance in the catchment. The lag times can reveal the pathways and timings through which water moves within the catchment (Barnard et al., 2010). The total time lag measured at the catchment outlet shows the overall catchment response to transpiration. However, it can be broken down into time portions taken by individual hydrological processes involved in the propagation of diurnal signals. For example, the time plants take to transport sap flow in response to radiation, the time measured between the diurnal peaks in groundwater level and baseflow (Szilágyi et al., 2008), and the instream time associated with the streamflow velocity.

Catchment characteristics like land use, topography, and soil types can affect diurnal streamflow fluctuations individually or collectively. The riparian vegetation is a critical catchment characteristic in controlling the diurnal patterns in baseflow. Vegetation also is crucial in regulating water fluxes through its effect on ET (Bren, 1997). Several studies have investigated the impact of vegetation cover on diurnal streamflow variations (Bren, 1997; Cuevas et al., 2018; Nachabe et al., 2005). For example, (Bren, 1997) found that removing vegetation from slopes resulted in significant changes in the diurnal variations of a small mountain stream. Nachabe et al. (2005) compared the ET demand and lateral fluxes with groundwater discharge for forested and pasture covers, determined a positive correlation between the parameters, and attributed the correlation to the ET consumptive use and the

proximity of the vegetation to the outlet. Similarly, Sarwar et al. (2022) demonstrated that the riparian zone could act as a source of evapotranspiration for a small headwater catchment by analyzing daily streamflow fluctuations.

The topography of a catchment also plays a crucial role in shaping the diurnal patterns of streamflow. A combination of factors like catchment size, shape, and slope can influence how water is distributed within the catchment and how flow pathways are modified (Barnard et al., 2010; Bren, 1997). A study by Wondzell et al. (2007) provided a velocity hypothesis to explain the lag increase with catchment size and stream length increase. The stream velocity hypothesis suggested that as catchment size and stream length increase, the daily increase in lag should also increase. Graham et al. (2013) investigated how catchment size influences the temporal correlation between transpiration and diel fluctuations in streamflow. The research revealed that, as summer progresses, the delay between vegetation water utilisation and streamflow response extends in each sub-catchment. This increase in lag time is influenced by factors such as catchment stream length and other characteristics, including geology, vegetation, and stream geomorphology.

Another study by Fondley et al. (2016) employed an analytical solution of flow equations to determine the role of river network size on the propagation of diurnal fluctuations in river networks. The study concluded that the river network's shape and size could affect diurnal signal propagation more than the soil-water processes, with larger catchments and longer river reaches exhibiting slower propagation of diurnal fluctuations in streamflow.

In addition, other catchment characteristics, like soil properties and topography, can also influence diurnal fluctuations. The hydraulic properties of the soil, such as its permeability and water-holding capacity, can affect the rate of infiltration and the storage and release of water in the catchment (Castellini et al., 2021).

The hydraulic properties of soil play a direct role in governing water infiltration into groundwater or its movement towards surface water, such as overland flow. Key soil attributes like permeability, water-holding capacity, and compaction significantly affect how water infiltrates the soil and

recharges the groundwater (Xia et al., 2022). Soils with higher water-holding capacity can buffer against rapid streamflow changes by slowly releasing water, thus masking diurnal fluctuations (Patel et al., 2021). However, this effect may be more pronounced between extended dry/wet periods or between different seasons like summer and spring than for rapidly changing flows in the short term. Moreover, soils with higher permeability, like sandy soils, allow for adequate groundwater recharge and provide higher sustained baseflow, ultimately dampening the rapid streamflow variations that would otherwise occur due to factors like evaporation during the day and cooling at night (Wang et al., 2009).

Soil permeability also affects hydraulic conductivity on shorter time scales. The amplitude of diurnal fluctuations depends on the water uptake depth and the soil permeability (Loheide II, 2008). In a study by Ali et al. (2013)A simulation is performed to analyse 2D steady-state saturated-unsaturated flow in hillslopes featuring depth-varying saturated hydraulic conductivity. The results of this simulation highlighted the significant impact of variations in the magnitude of the exponential decline in hydraulic conductivity on the patterns of flow, residence time, and the distribution of transit times.

The length of a catchment or the longest streamflow path determines the travel time for water to move from the upper reaches of the catchment to the outlet. Longer flow paths generally result in slower responses and delayed diurnal fluctuations due to the increased water travel time through the watershed (Wondzell et al., 2007). Stream travel time determines the lag between climate drivers of ET and the overall catchment hydrologic response (Széles et al., 2018). A longer flow path also interacts with the riparian zone over a longer distance, increasing baseflow contribution and diurnal amplitude in streamflow through constructive interference (Wondzell et al., 2007).

Urbanisation can significantly impact streamflow patterns. The conversion of natural land cover to impervious surfaces, such as roads, buildings, and parking lots, can increase surface runoff and reduce infiltration, leading to changes in the timing and magnitude of streamflow (Bibi et al., 2023). Urban areas often have extensive stormwater management systems, including storm drains and

detention ponds. These can further alter the flow regime by shortening the groundwater travel times and increasing baseflow discharge (Schilling et al., 2012). This interference can mask diurnal fluctuations in streamflow, making it challenging to see the ET effect on groundwater levels and baseflow.

4.2 Objective

Understanding the diurnal fluctuations and their relationship to catchment parameters is essential for water resource management, ecological assessments, and flood forecasting. Several studies have focused on analysing the mechanisms for generating and propagating diurnal fluctuations or have used diurnal streamflow fluctuations to estimate riparian ET (Barnard et al., 2010; Bond et al., 2002; Loheide II, 2008). However, very few studies have focused on studying the effects of catchment attributes on daily fluctuations and their evolution across various catchments.

This study mainly focuses on the variability in the diurnal streamflow fluctuations across 217 catchments in New Zealand. Moreover, the possible relationships between the catchment's physiographical parameters, including catchment shape, size, vegetation type, land cover, and soil properties, alter the characteristics of the fluctuations.

4.3 Material

4.3.1 Study Catchments and Data

The study uses a variety of hydrological and climate datasets to analyse diurnal fluctuations and catchment characteristics. The hydrological data consisted of streamflow observations. Streamflow data for most of the regions in the study was readily available on environmental data portals of regional authorities (councils). However, the 15-minute streamflow data were obtained via service request for the Waikato region and later converted to hourly resolution. Table 4.1 provides details of the regions in the study, the number of catchments, and the period of hydrological data used for each region.

Table 4.1 Details of the catchments and hydrological data included in the study

Region	Auckland	Bay of Plenty	Waikato	Canterbury	Northland	Tasman
Total	28	27	16	117	50	23
Catchments with Diel Signals	21	16		56	32	19
Period of Streamflow	2014-2021	2012-2021	2012-2022	2013 - 2022	2012 - 2021	2012-2021

Apart from the streamflow data, a variety of climate and land Hourly radiation data was obtained from CliFlo (Climate Information, https://cliflo.niwa.co.nz/) system of the NIWA (National Institute of Water and Atmospheric Research) for some climate stations across different NZ regions.

The 8 m national DEM (Digital Elevation Model) raster from LINZ (Land Information New Zealand_ https://data.linz.govt.nz/) was used to delineate catchments based on the location of the flow measurement site. The delineation process was refined using the vector catchment first-order dataset from NIWA, which is also based on the same 8 m DEM. The delineated catchments for regions selected for study are shown in Figure 4.1. Besides obtaining the catchment shape parameters, the NIWA dataset also contained a stream layer, which determined each catchment's longest flow path, slope, and drainage density.

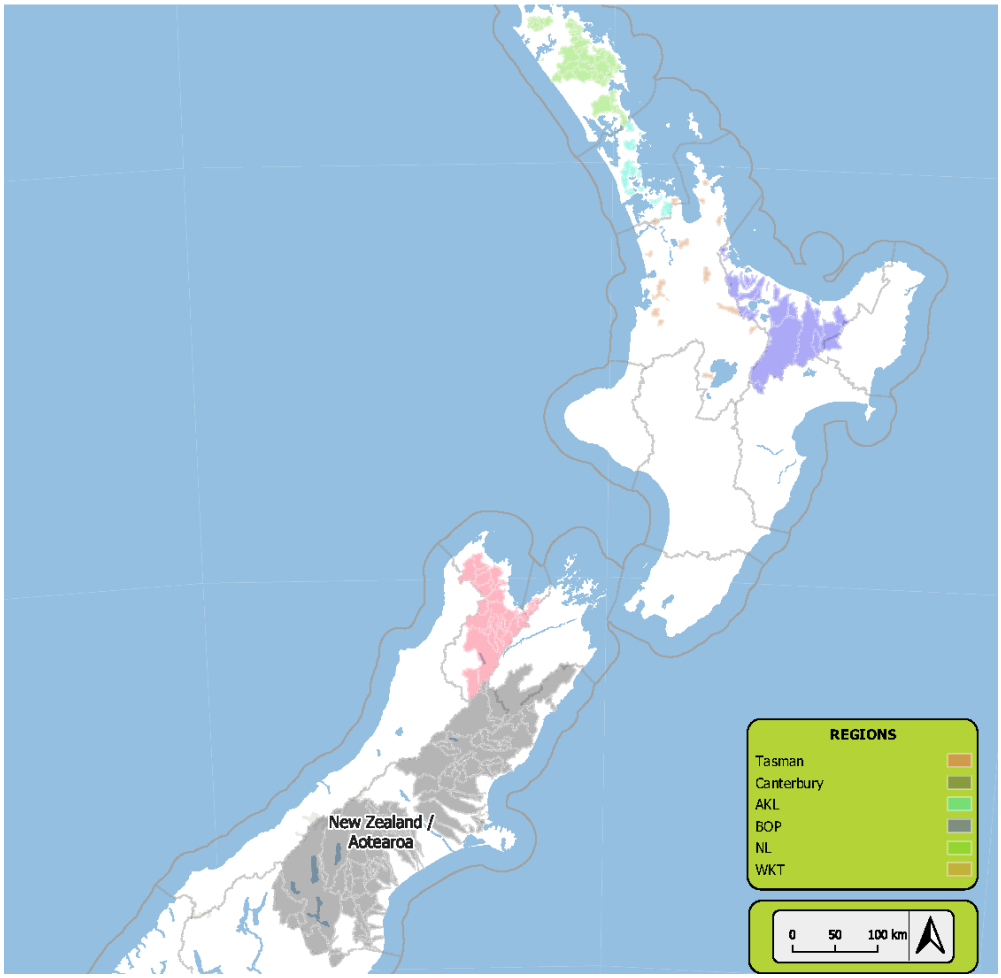

Figure 4.1 Catchments included the study.

Snow cover data was obtained from NASA's Giovanni data service (https://giovanni.gsfc.nasa.gov/giovanni/). The data included raster maps for the seasonal averages of snow depths for New Zealand. Table 4.2 summarizes the different types of data used in this study and information on their sources.

Table 4.2 A summary of datasets used in this study with their sources.

Data	Units - Resolution	Database	Source
Streamflow	m^3/s - 15 min/ 1hr		Council Environmental Data
Digital Elevation Raster	8m		LINZ portal
1st order Vector Catchments and Streams		River Environment Classification Database v2	NIWA
Solar Radiation	MJ/m^2 - 1hr		CliFlo - NIWA
Snow Cover	0.1º - Monthly	FLDAS_NOAH01_CP_GL_M	GIOVANNI
Land Cover		LCDB v5	LRIS Portal

4.3.2 Catchment Selection Criteria

The study employs basic rules to identify catchments for analysing diurnal stream flow fluctuations. The first and most important of the criteria is dealing with snow-fed catchments. The South Island of New Zealand features numerous snow-fed catchments crucial to the region's water supply and hydroelectric power generation. These catchments are primarily found in the Southern Alps, the mountain range that runs along the western side of the South Island (Khadka, 2020).

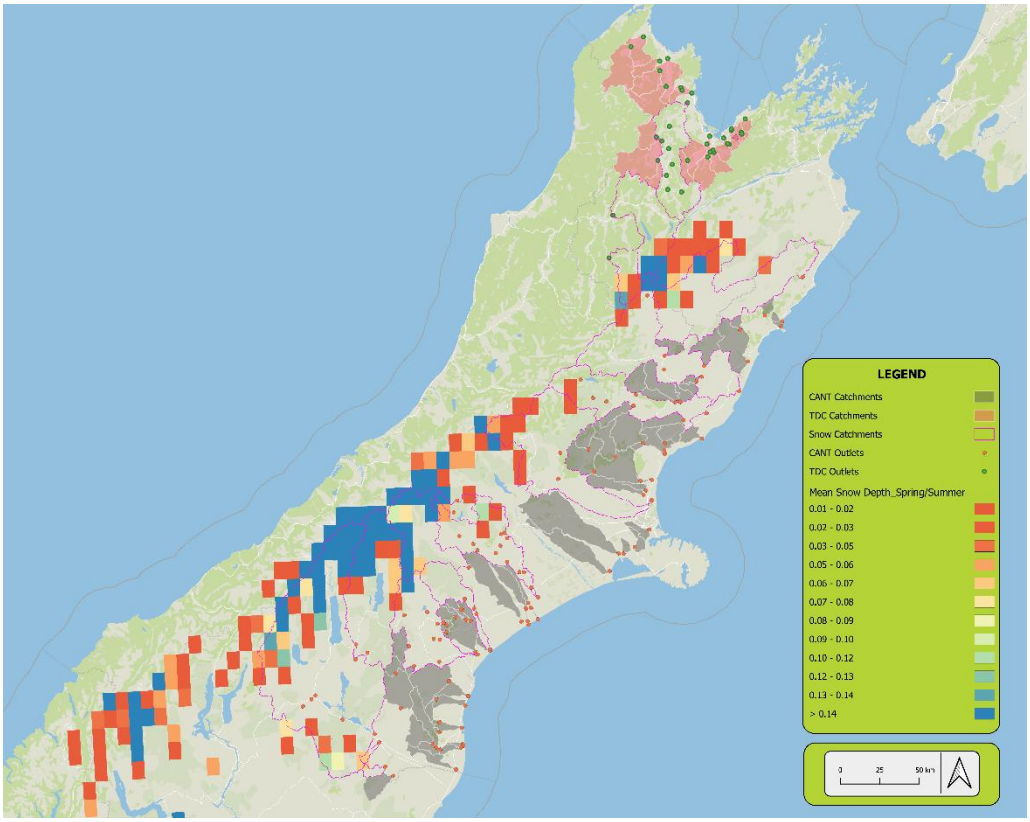

Figure 4.2 Average Snow Depth during the Spring-Summer season in the South Island, New Zealand, and the selected non-snow catchments

In the catchments where snowmelt and ET cycles occur, daily variations in solar flux drive these cycles, but they exhibit opposite effects on the catchment streamflow. Snowmelt contributes to streamflow during the daytime, while ET removes water from the system during the daytime. The streamflow patterns in these catchments are often driven by a combination of factors, including snowmelt, rainfall, and evaporation (J. D. Lundquist & Cayan, 2002). However, the net effect of snowmelt and evaporation on streamflow depends on their relative strengths. When both processes are active, they can cancel each other out if they are of equal strength (Kirchner et al., 2020).

Satellite snow maps, which show the long-term mean snow depth, are used to identify catchments where the snowmelt could affect the relationship between ET and streamflow (Figure 4.2).

The catchments where the mean snow cover depth is equal to or greater than 0.01m throughout the summer/spring season are excluded from the study to focus on a more homogenous set of catchments

where diurnal fluctuations are primarily influenced by ET and rainfall, making the analysis more relevant for those specific conditions

A cutoff of 500 km^2 for catchment size was adopted due to the increasing spatial variation in land use. Increased travel distance along the channels might also cause destructive interference in diurnal signals and offset the diurnal lag in larger catchments. The cutoff also removed catchments with large water bodies like lakes and rivers on a significant portion of their area. These are also excluded due to their possible buffering effects on masking the ET-induced diurnal fluctuations.

Finally, only catchments without any or minimal human interference were selected for the study by employing specific land use criteria. The land use in each catchment was analysed using LCDB v5, which had land use information from 1996 to 2018. Catchments with more than 5% residential cover were excluded to minimize the effect of urbanization on diurnal streamflow fluctuations and establish valid links between catchment characteristics and diel signals. Moreover, only catchments without significant changes in dominant land use throughout the period covered by the hydrological dataset were considered to avoid potential biases in the overall ensembles. This approach ensured that natural factors, rather than anthropogenic ones, primarily influence the observed diurnal fluctuations in streamflow. The complete list of catchment names, with their location and shape attributes, is provided in Appendix A.

4.4 Methodology

4.4.1 Streamflow Data Processing

The analysis of streamflow data involves a series of crucial steps designed to uncover the underlying patterns and diurnal characteristics. These steps are detailed below.

4.4.1.1 Detrending through DWT

The hourly streamflow data were first detrended by subtracting a trend from the original time series, which was calculated using the discrete wavelet transform (DWT).

Figure 4.3 shows an example hydrograph and the detrended signal with the modified DWT process. The entire streamflow signal is divided into sections of finite length, and DWT is applied to the overlapping individual sections. The resulting detrended sections were then stitched together to obtain the full-length detrended signal. The "bior 6.8" wavelet was chosen for the detrending purpose, with a decomposition level of 4. The Garrotte threshold rule was used to remove noise at each decomposition level. The combination of wavelet type and threshold rule has been seen to perform best when detrending the real-life observed streamflow signals to extract diurnal fluctuation. The DWT trend adequately follows the sharp rise and fall in the signal while showing fewer variations during exponentially decaying recessions.

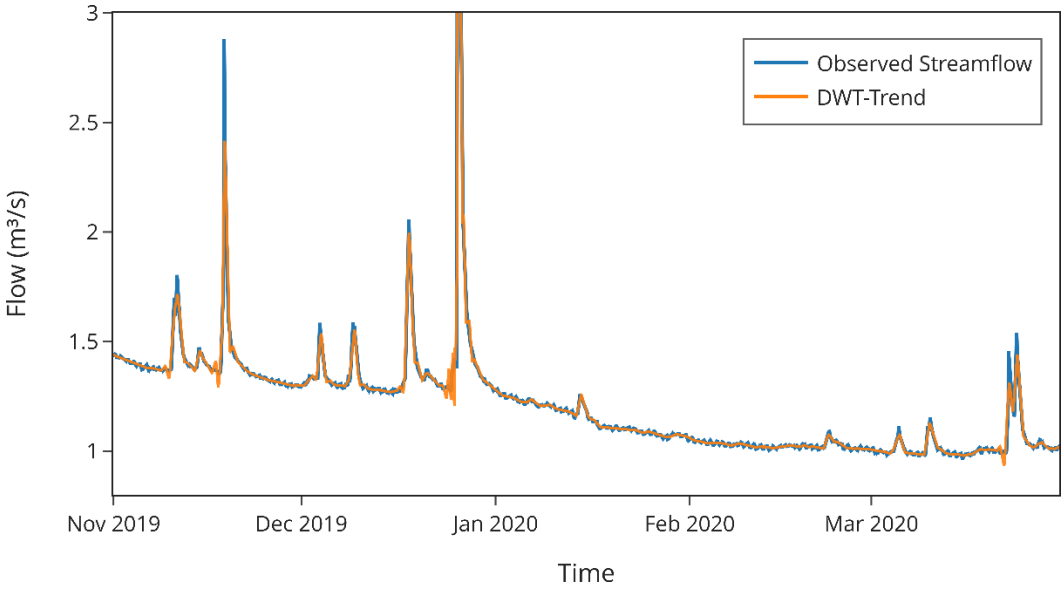

Figure 4.3 Detrending of a sample hydrograph with the modified DWT thresholding process.

4.4.1.2 Continuous Wavelet Transform (CWT):

The time series was passed through the designed CWT process to identify the diurnal episodes. The CWT provides high-resolution information about a signal's time and frequency characteristics and enables the identification of transient events like sharp peaks or sudden changes in frequency. CWT coefficients can be presented as a power spectrum and used to visualise the relative strength of

specific frequency components within the signal (Figure 4.4b). Peaks in the CWT spectrum indicate the presence of significant frequency components at particular times.

The second CWT plot, (Figure 4.4c), is the global wavelet spectrum (GWS), which measures the overall strength of different frequencies across all scales (or frequencies) in the wavelet transform. It helps identify dominant frequencies by showing which frequencies have the highest power throughout the entire signal length. By examining the GWS, the most significant frequency components in the signal can be identified, regardless of when they occur.

The third plot,(Figure 4.4d) is the scale average variance (SAV) obtained by averaging the variances between a specific scale range across the signal length. SAV is particularly useful for understanding how a signal's variability changes for different scale ranges. A high SAV value above the specified threshold indicates that other frequencies outside of the specified range are more dominant.

Together, the CWT helps us identify timestamps where the dominant frequency in the signal is diurnal or close to diurnal while discarding any locations where the diurnal frequency might be more dominant. However, there was significant distortion in the signal corresponding to a spike.

Only the episodes with a dominant diurnal frequency for at least four days are selected for further analysis—other filtering operations, like removing the outliers before averaging and removing any isolated event after removing outliers.

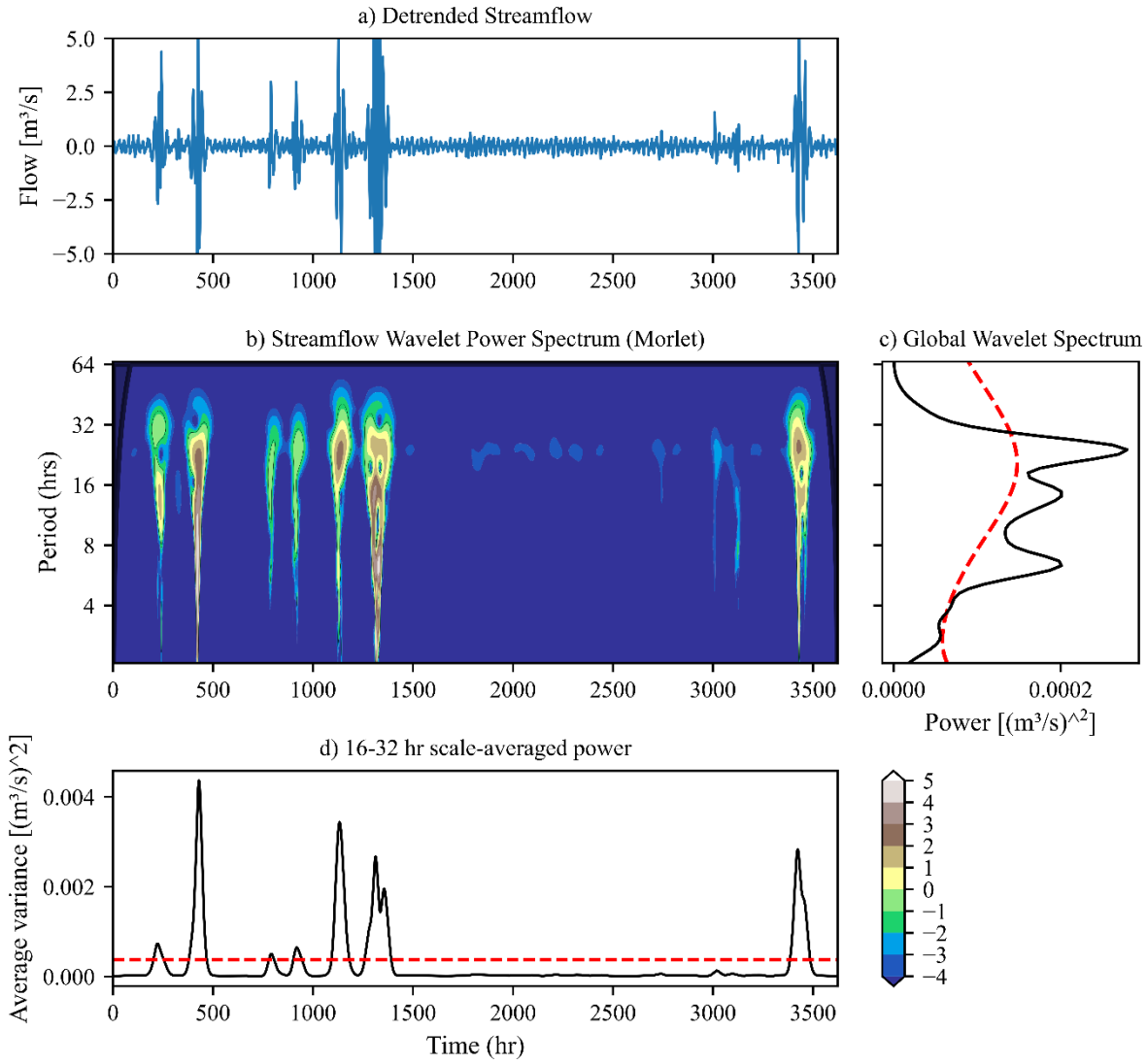

Figure 4.4 The CWT plots for the detrended streamflow signal. Plot (b) represents the wavelet powers for individual scales across the time domain with the help of a colour scale. Plot (b) is the global wavelet spectrum, showing the total power in each scale and the 5% significance red-noise threshold. Plot (c) shows the average variance in the signal between the scale range 16 -32, which corresponds to the diurnal fluctuations, and the 5% significance red-noise threshold.

4.4.1.3 Averaging Diurnal Signals:

An average representative diurnal profile of the signals is often constructed to summarise the diurnal characteristics of a site and compare it with different catchment parameters. This is achieved by creating an ensemble of daily observations against each specific hour of the day across the entire dataset (Figure 4.5).

The ensembles are then averaged to construct the typical diurnal pattern for a specific location or station, such that the average value at each hour of all the days forms a point on the diurnal profile curve. Ensemble averaging produces a more reliable diurnal profile that captures the true essence of the underlying pattern and provides a more robust and representative estimation of diurnal features.

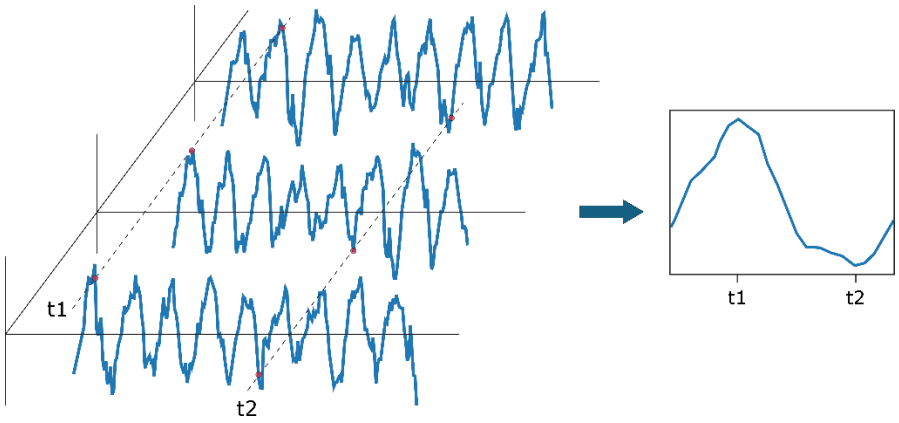

Figure 4.5 The Process of obtaining ensemble averages from multiple continuous diurnal episodes. Three sample diurnal episodes are shown here on a uniform time axis. All the fluctuation points falling on the same timestamp are averaged together across the length of each signal and for all episodes to obtain a 24-hour representative signal.

4.4.1.4 Calculating Diurnal Features:

The average diurnal profiles are then used to calculate the diurnal amplitude and timing of each site's diurnal maxima and minima (Figure 4.6). The amplitude is half of the difference between diurnal

maximum and minimum values. Meanwhile, the diurnal lag is the difference between the timestamps of maximum radiation and the following diurnal minima.

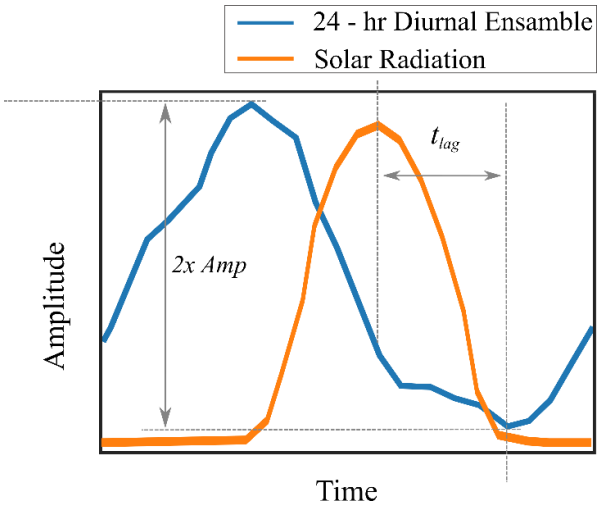

Figure 4.6 Calcualtion of diurnal features

4.4.2 Catchment Parameters:

Different attributes are used to quantify the shape of catchments. Collectively, these indices provide valuable information to comprehend the characteristics and behaviour of different drainage basins. The following are the key parameters frequently utilised for this purpose:

4.4.2.1 Circulatory Ratio (Rc):

The circularity ratio is the ratio of the basin area and the area of a circle with the same perimeter as that of the basin (Miller, 1953). The circularity ratio measures the circularity or compactness of the catchment shape. A low R_c value implies an elongated basin shape, while a high R_c value indicates near circular.

$$R_c = 4\pi A/P^2 \qquad (4.1)$$

Where, A = catchment area

P = Catchment perimeter

4.4.2.2 Elongation ratio (Re)

The elongation ratio is the ratio between the diameter of a circle with the same area as the basin and the basin length (Schumm, 1956). The elongation ratio is used to categorise the general shape of a subbasin. Elongation ratio values typically range from ~0.2 to 1.0, with lower values representing elongated basins and values close to 1 representing circular basins (Subramanya, 2008). The elongation ratio measures the drainage basin's form, and the Re was calculated by Equation:

$$R_e = \frac{2}{L_b}\sqrt{A/\pi} \qquad (4.2)$$

Where, L_b = length of longest flow path

4.4.2.3 Compactness or Form Ratio (Rf):

The form ratio of a catchment is defined as the ratio of the perimeter of a catchment to that of an equivalent circle (Horton, 1932). Mathematically,

$$R_f = \frac{0.282 * P}{\sqrt{A}} \qquad (4.3)$$

The equivalent circle is a hypothetical circle with the same area as the catchment. This ratio may provide a measure of a catchment's response time in relation to a precipitation event. A high form ratio describes a catchment having a fast and peaked catchment response with a tendency of flash flooding (Abdo, 2020; Wagener et al., 2007).

4.5 Results

4.5.1 Extraction of Diurnal Episodes

Figure 4.7 shows the streamflow series for one of the stations included in the study. It also shows the detrended signal by applying a modified DWT process and the timestamps for diurnal signals, as revealed by CWT. Further, the figure shows the 24-The ensemble means for the diurnal signal and the solar radiation.

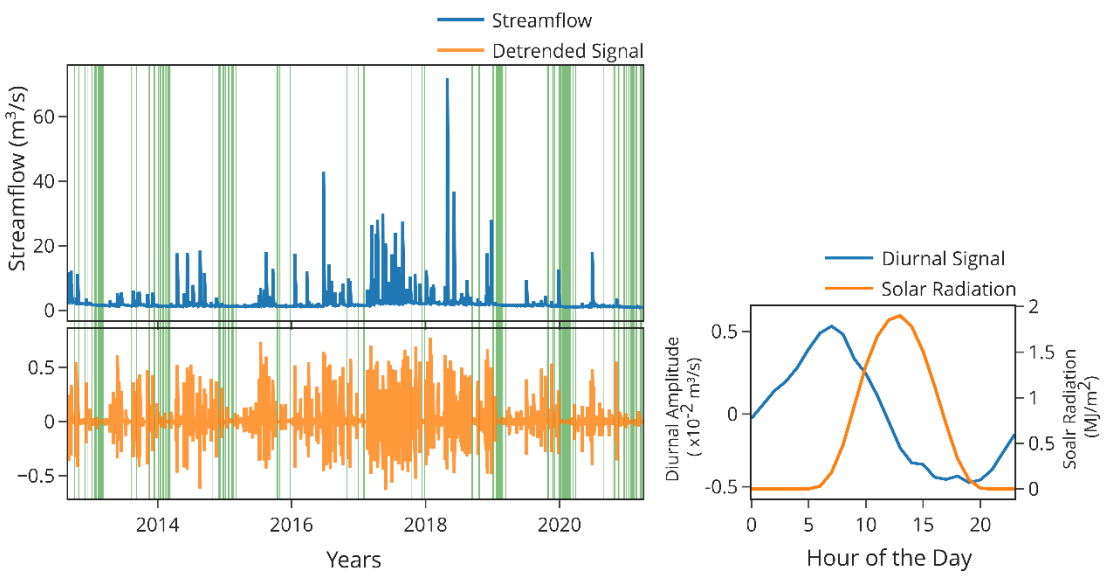

Figure 4.7 Extraction of diurnal episodes from a sample length of streamflow observations using the wavelet transform process. The second plot also shows the 0-24 hr ensemble average of all the diurnal fluctuations detected in the signal and the solar radiation.

As the CWT process reveals, the green bars represent the timestamps of diurnal episodes in the detrended signals. The individual fluctuations are aggregated to create 24-hour ensembles. This aggregation process smooths out the episode-to-episode variations and provides a consolidated signal representing the streamflow's average diurnal behaviour over a 24-hour cycle.

Similarly, a parallel process is undertaken with the solar radiation data. A 24-hour mean for the solar radiation values is calculated by averaging radiation measurements throughout the study period. This average allows for quantifying the difference between the peak radiation value and the subsequent minima within the diurnal fluctuations, providing insights into the daily variation in solar radiation and illuminating the timing and magnitude of peak solar energy input and its subsequent decline over a day.

4.5.2 Catchment Shape Parameters

The shape parameters, including drainage density, elongation ratio, circulatory ratio, and compactness, are calculated for the delineated catchments and summarized in Table 4.3.

Table 4.3 Average values of different catchment shape parameters for different regions

Region	Elongation Ratio	Circulatory Ratio	Compactness
Auckland	0.624	0.300	1.862
Bay of Plenty	0.452	0.213	2.229
Canterbury	0.465	0.226	2.241
Northland	0.586	0.298	1.872
Tasman	0.565	0.282	1.930
Waikato	0.507	0.246	2.052

The combination of these values is then used to assess the shapes of the catchments in each region. Auckland showed the highest Re and Rc values with the smallest compactness, meaning Auckland

had more circular-shaped catchments. The catchments in Canterbury and Bay of Plenty showed the lowest, indicating an elongated catchment shape.

4.5.3 Seasonal Variation in Diurnal Amplitudes

The descriptive statistics of diurnal amplitude for different seasons are also shown in Figure 4.8 These parameters include maximum, minimum, mean, median, and fractional diurnal amplitude. In addition to these diurnal parameters, the figure shows the seasonal and regional average temperatures. The figure provides a region-wise breakdown of the parameters in different seasons and their seasonal averages. The regions are abbreviated as Auckland (AKL), Bay of Plenty (BOP), Waikato (WKT), Northland (NL), Tasman (TDC), and Canterbury (CANT).

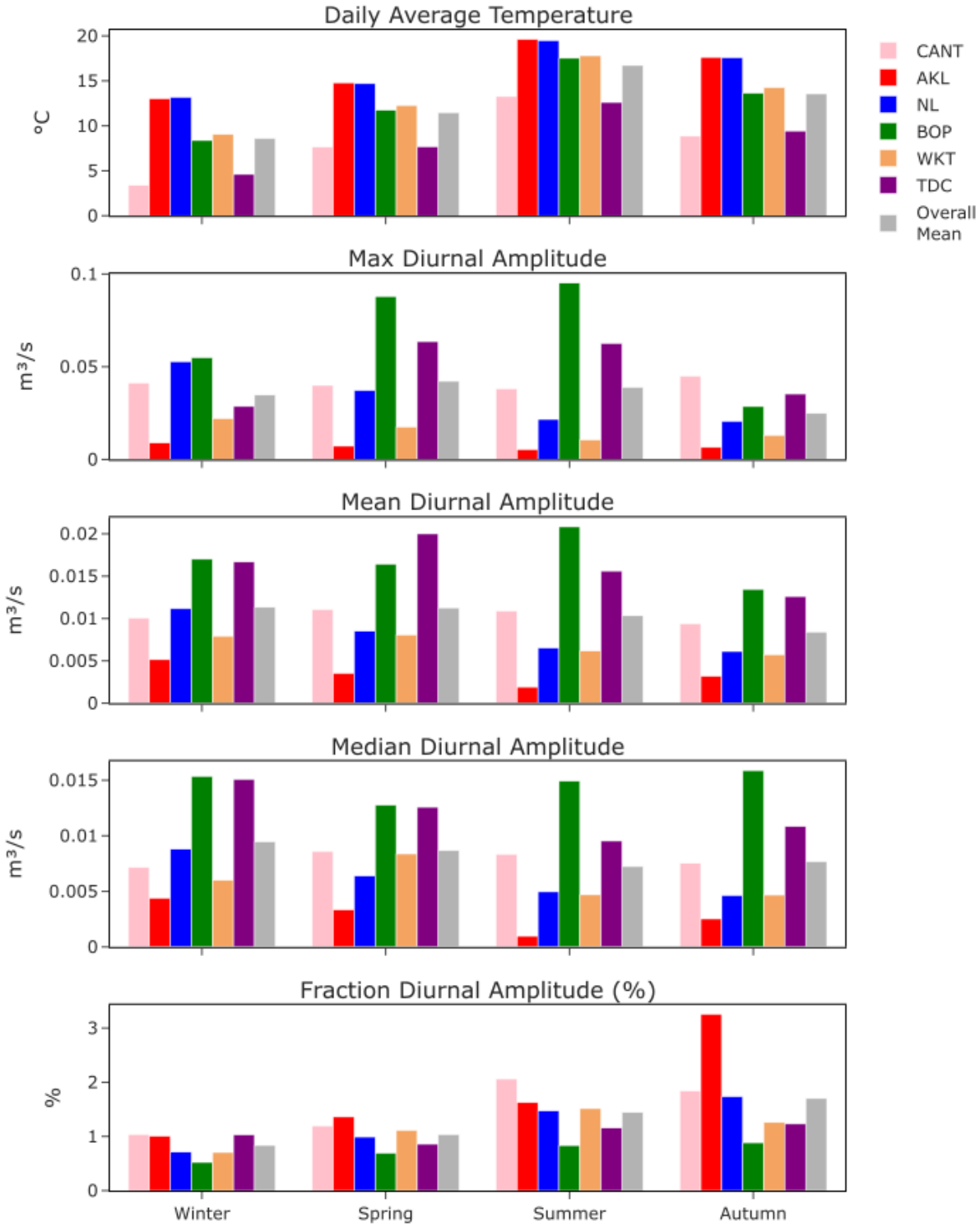

Figure 4.8 Seasonal variation in the average temperature and diurnal attributes for different NZ regions in the study, along with their seasonal averages.

Higher average and median diurnal amplitudes are observed in the colder winter and spring seasons compared to the warmer summer and autumn seasons. Conversely, the proportion of diurnal amplitude relative to the total daily mean flow exhibits an opposite pattern to the amplitude itself. Summer and Autumn episodes showed more significant percentages than the other two seasons. Notably, Auckland showed a significantly higher percent amplitude than the rest in all seasons.

It is worth mentioning that, unlike summer and spring, the winter and autumn seasons do not exhibit a three-month average. The winter season only shows values for August, while Autumn represents values for March only. This is because they represent the beginning and end of diurnal fluctuations and do not have ET-induced fluctuations for the whole season.

Further, A simple correlation analysis is used to quantify the relationship between different catchment parameters and the diurnal features across different seasons. In Figure 4.9, the average diurnal amplitude is also compared with the different catchment sizes and shapes. Catchment shapes are represented in Rc values, where higher Rc values mean closeness to a perfect circle and vice versa.

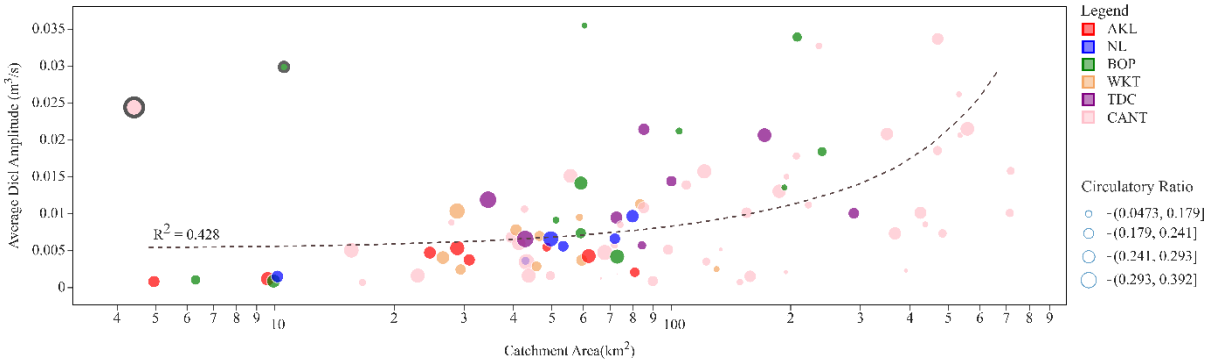

Figure 4.9 Correlation between the different regions' catchment size and the average amplitude of diurnal fluctuations. The bubble size shows the catchment shape in terms of the circulatory ratio.

Overall, the catchments of various shapes exhibited a positive relationship with their scales and diurnal amplitude (R^2 = 0.43). Notably, the Northland and Tasman regions displayed strong

correlations of 0.84 and 0.81, respectively, while the Canterbury region had a lower R^2 value of 0.28. Moreover, the Canterbury region had the weakest correlation for catchments larger than 300 km^2.

4.5.4 Distribution of lag time

Figure 4.10 the seasonal values of average lag times for the catchments in the different regions and the overall average lag time for each region.

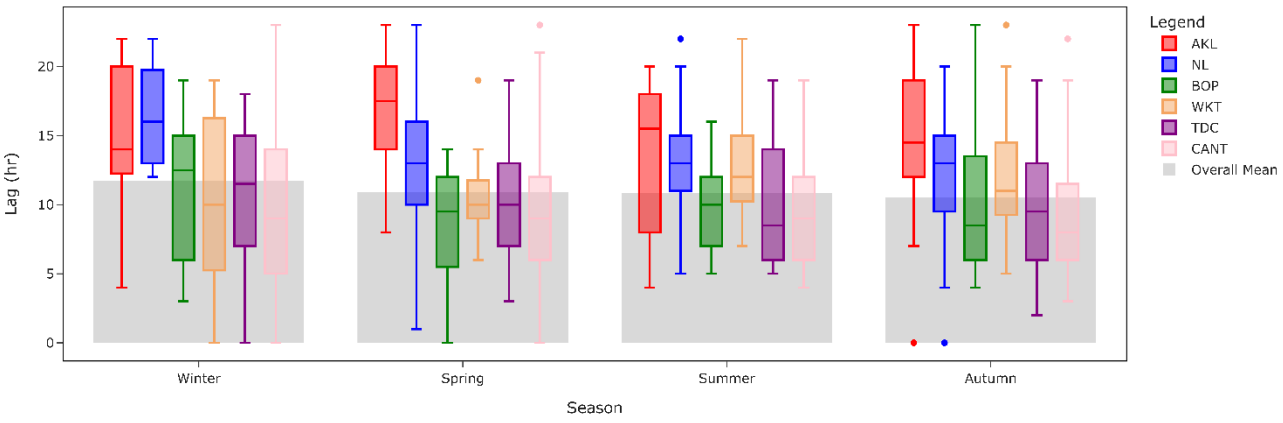

Figure 4.10 Seasonal variations in the lag between maximum radiation and minimum streamflow across different regions. The overall means are represented as grey bars.

The average lag times for the seasons lie within 11 -12 hours. However, the lag shows seasonal variations, as seen in the box plots. For the months of Winter (August), most lag time observations fall above the mean. The variation of lag times remains almost the same for summer and spring, though slightly lower for summer. The autumn season also shows a declining trend in the opposite direction, with most observations below the mean.

Figure 4.11 shows the Geographic Information System (GIS) map illustrating the seasonal lag values across different regions. The map provides a visual representation of the temporal delay in the peak or trough of a season. Each point on the map corresponds to a specific location, with the colour gradient indicating the magnitude of the seasonal lag. This allows for an intuitive understanding of how seasonal changes vary geographically.

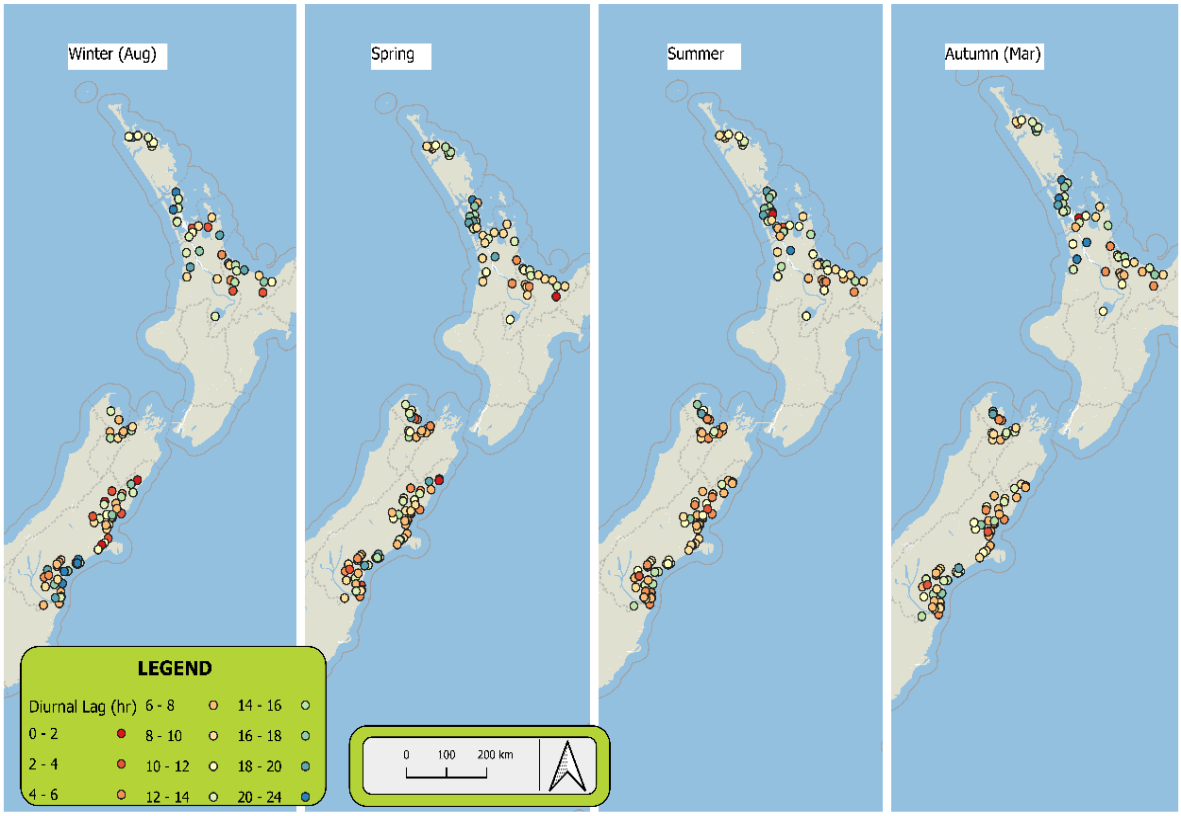

Figure 4.11 Average diurnal lags for the different NZ catchments included in the study across seasons. The Winter season consists of only August observation, while Autumn shows only March values.

4.5.5 Catchment Shape and Diurnal Lag

Apart from the overall distribution of lag time, further investigation is made to analyse the effects of different physiographical parameters on it.

Figure 4.12 shows the average lag time for different lengths of main channels of different catchments. A third parameter of the circulatory ratio is used as a variable size to see further the effect of catchment shapes on the lag time stop. It is observed that catchments with a central channel having less than 30 Km showed a moderate correlation with the lag time for various catchment sizes.

The effect of catchment shape, described in terms of circulatory ratio (Rc), can also be seen in the diurnal lag for different stream lengths.

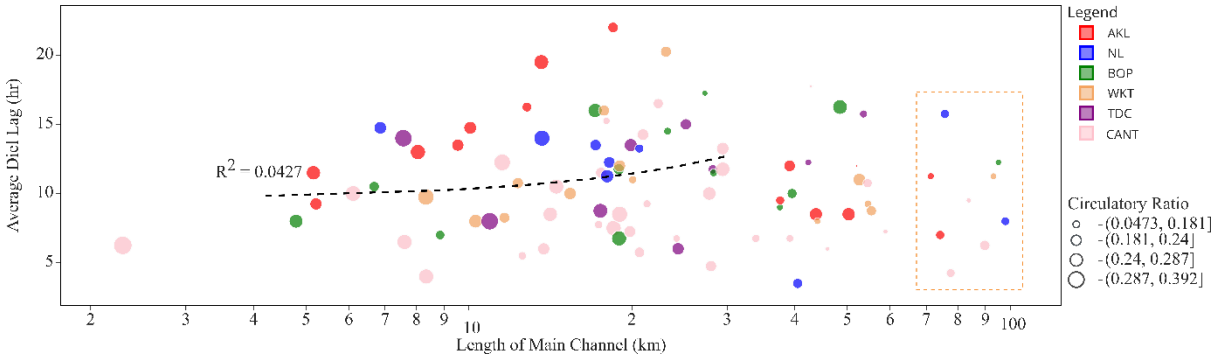

Figure 4.12 Average diurnal lag vs. length of the main channel in the catchment. Bubble size represents the circulatory Ratio (Rc) of the catchment. The data shown inside the dashed box shows the longest flow paths.

Figure 4.12 shows that the catchments can be divided into three groups according to the longest flow path. The first group is the largest, with catchment lengths up to 30km. Most of the catchments in this group have higher Rc values and exhibit a very weak positive correlation with the average diurnal lag. However, for very long catchments of this group with Rc values less than 0.2, there is a decent correlation (R^2 = 0.29) between catchment length and diurnal lag.

The diurnal amplitude is also compared against the average diurnal signals for catchments of various sizes (Figure 4.13).

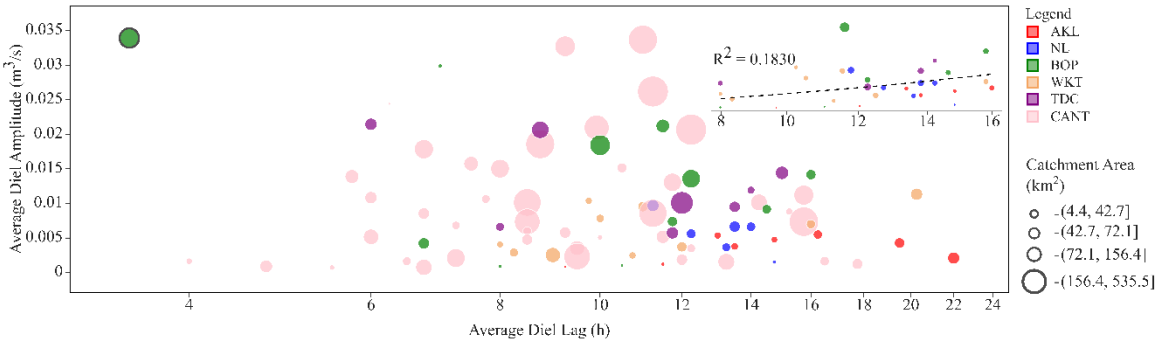

Figure 4.13 Average diurnal lag vs. average diel lag. The data (small box) show a moderate trend between diel amplitude and diel lag. The bubble size shows the catchment area.

The figure shows that catchment size directly impacts the diurnal amplitude, as a higher, more significant proportion of the vegetation zone contributes to the overall baseflow patterns. Most catchments showed a positive relationship between increasing diurnal lag and amplitude, particularly in the Waikato region's catchments. The large catchments in Canterbury showed the highest amplitudes, and the diurnal lags in these large catchments values in. The only catchment segment that showed some degree of correlation between diurnal lag and amplitude comprises smaller catchments (<100 km^2), with lags ranging from 8-hr to 16-hr (shown in the small box).

4.6 Discussion:

4.6.1 Diurnal Amplitude and Spatiotemporal Variability in Climate

The seasonal variation in the average diurnal amplitude reveals the effect of temperature changes on the streamflow patterns. The colder seasons of winter and spring exhibit increased amplitudes in the seasons compared to the warmer seasons. The increase could be attributed to a couple of processes taking place simultaneously. Firstly, with higher soil moisture content in winter and early spring seasons, plant roots are able to reach deeper into the saturated zone and induce more significant diurnal dips into the saturated zone. This, in turn, produces pronounced variations in the groundwater

table between night and day. Ultimately, this oscillation pattern then makes its way to streamflow, resulting in the observed increase in diurnal amplitude.

Secondly, many deciduous trees and plants start to leaf out towards the end of winter or early spring. The emergence of leaves results in a larger surface area for transpiration, and as spring commences and temperatures begin to rise, plants may quickly utilise some of this moisture (Ehlers, 1991; Denham et al., 2023). Combining the increased vegetation activities with available soil moisture may result in higher diurnal fluctuations as plants take advantage of the available water.

Conversely, during the warmer season with extended dry periods, higher ET rates and low groundwater recharge deplete the saturated zone and cause the groundwater table to decline. The saturated zone within the soil gradually shrinks and retreats closer to the stream. Despite higher ET demands, fewer plants can tap into the saturated groundwater reserves as the soil moisture levels are at their lowest in summer. The reduced soil moisture content limits the availability of water for plant roots, making it harder for many plants to engage in significant transpiration (Sarwar et al., 2022).

The temperature changes also affect the proportion of diurnal amplitudes expressed as the percentage of the daily mean discharge's diurnal amplitude. Despite more significant diurnal variations in the amplitude, the relative abstraction is less pronounced than the total available moisture. In late winter or early spring, high soil moisture is the relative abstarction of water compared to the total available water. On the other hand, as the flows shift from high recession to low flows from winter to summer, the percentage of diurnal amplitude represents a higher fraction of the daily mean flow. This may be due to the increased ET activity during summers when temperatures are at their peak. As a result, more water is lost to the atmosphere through ET, further diminishing the volume of water contributing to streamflow.

Notably, Auckland showed the most significant increase in fraction diurnal amplitude, followed by Northland. The increase in percent amplitude is linked to the high-temperature conditions in these regions compared to other regions, particularly the South Island. Auckland region has an average annual temperature of 16 ºC while the South Island is 12 ºC. The high temperature causes a

heightened transpiration rate and increases evaporation from the water's surface (W.K. Song and Y. Chen, 2020). The combination of these effects culminates in an increase in diurnal streamflow amplitude in regions with high-temperature conditions, such as Northland and Auckland.

4.6.2 Diurnal Amplitude and Catchment Attributes

Catchment size and diurnal amplitude strongly correlate across regions, except for Canterbury. This strong correlation implies that, in general, smaller catchments exhibit lower diurnal amplitudes than catchments with larger surface areas. Smaller catchments have limited water storage capacity, higher vegetation ratios, and limited groundwater storage, collectively contributing to more uniform flow patterns. (McGlynn et al., 2004). As the catchment scale increases, the area of active transpiration and evaporation also increases, which increases the loss of Earth's water to the atmosphere.

On the other hand, larger catchments may have more significant spatial variability in the timing and extent of snowmelt and ET processes (Graham et al., 2013). Some parts of the catchment may experience more snowmelt due to higher elevations. In contrast, others may have more significant ET due to lower elevations, which receive more solar radiation and have warmer temperatures and less or no snow cover. This spatial heterogeneity in snowmelt and ET processes may induce diurnal signals of opposing phases across different stretches of the stream and result in a mixed type of diurnal signal (Jutebring Sterte et al., 2021; Mutzner et al., 2015; Lundquist & Cayan, 2002). So, instead of representing a scaled-up version of the diurnal amplitude in a smaller catchment, these signals represent an integration of the diverse hydrological responses occurring throughout the catchment. As a result, the correlation between catchment size and diurnal amplitude becomes weaker in larger catchments due to the diverse and heterogeneous nature of environmental processes within these regions.

4.6.3 Catchment controls on lag time:

The lag between vegetation water use and streamflow response underscores the critical role of subsurface storage and groundwater contributions to streamflow, particularly during low flow

periods. The observation of diurnal lag times reveals several significant implications for catchment behaviour, highlighting the influence of various physiographical parameters on these dynamics.

The comparisons of lag times with different channel lengths revealed that stream distances play an essential role in determining the overall lag between maximum transpiration and the hydrological response of the catchment. The catchments, having a more compact shape, like in the region of Canterbury, had a smaller lag for a similar length of the main channel as compared to Auckland or Northland, where the catchments were much more round in shape. Overall, the lag and channel length are related positively, but a similar relation could not be established for very long streams (>30 km). This may point toward the fact that in smaller or medium-length streams, the diurnal signals experience less destructive interference along shorter and straighter stretches of riparian corridors. For such catchments, their propagation times in the baseflow can be correlated with in-stream distances.

In comparing diurnal lag with the catchment shape, the Auckland region exhibits the most extended diurnal lag, indicating a delayed streamflow response in its catchments. While looking at the different catchment shape parameters, it is determined that this delay could be attributed to the unique characteristics of Auckland's catchments, notably their high elongation and circularity ratio. In contrast, a small circularity points towards a more compact and linear catchment. These factors mean that water has to travel a longer, more winding path before reaching the main river or stream.

Circular catchments with higher Rc values showed larger diurnal lag values for similar mainstream lengths. In circular catchments, water converges towards the central point of the catchment through longer tributaries running along the catchment axis. This can lead to longer travel distances and potentially longer response times as water moves through the catchment's landscape before reaching the central point of convergence. Moreover, water flow from various parts of the catchment to the stream is relatively uniform and can lead to slower propagation (J. Zhang et al., 2022). On the other hand, streamflow in elongated catchments tends to travel shorter distances because water has a more direct path to follow along the elongated axis of the catchment. While there can still be variations in

flow within an elongated catchment, the overall flow patterns are more constrained than circular catchments (Zhang et al., 2022).

Overall, it was observed that catchment size and shape have effectively controlled the lag between maximum vegetation water use and streamflow response. However, it is important to note that other factors, such as vegetation, soil type topography, etc., can also play a significant role in affecting the attribute of these diurnal fluctuations (Graham et al., 2013; Legarda Garzon et al., 2023; Mutzner et al., 2015). Therefore, while catchment shape and scale might impact streamflow, they are just a few factors that can influence diurnal amplitude and lag due to ET.

4.6.4 Catchment Heterogeneity and Durnal Fluctuations

Catchment heterogeneity plays a significant role in shaping streamflow patterns, adding complexity to the analysis of diurnal signals and their relationship to atmospheric drivers (H. K. McMillan et al., 2022). Variations in soil layers create differing capacities for storing and releasing water, resulting in complex streamflow patterns that are not easily correlated with atmospheric conditions (Blume et al., 2009). Rapid responses to rainfall in upper soil layers, combined with slower contributions from deeper groundwater, lead to lagged and multi-peak diurnal variations (Vereecken, 2023).

Diversity in land use impacts diurnal fluctuations by introducing variability in runoff generation, evapotranspiration rates, and water storage dynamics across a catchment. Forested areas with dense vegetation promote infiltration and steady baseflow, leading to pronounced fluctuations driven by evapotranspiration (Széles et al., 2018). Agricultural lands contribute irregular patterns due to irrigation and compacted soils that increase surface runoff (T. Zhang et al., 2018). Urban areas with impervious surfaces amplify rapid runoff responses, often diminishing natural diurnal signals (Rodrigues et al., 2019). The diverse responses of various soil layers and land parcels within the catchment can cause the overall streamflow to seem "decoupled" from daily atmospheric drivers like evapotranspiration, making it challenging to draw direct connections between observed fluctuations and their drivers.

Assuming homogeneity within the catchment when significant heterogeneity exists can lead to misleading conclusions about the factors driving diurnal fluctuations. Data may erroneously suggest that atmospheric drivers alone control diurnal patterns, overlooking the substantial role of internal catchment processes. Conversely, the presence of clear and consistent diurnal patterns might indicate a homogeneous and predictable catchment response with minimal disruption from internal variability. In such cases, streamflow patterns closely reflect external atmospheric influences, as heterogeneities in subsurface structures, soil characteristics, and vegetation cover are not pronounced enough to alter the direct hydrological response on a diurnal timescale. This highlights the importance of accurately accounting for catchment heterogeneity when studying diurnal signals to avoid false interpretations.

4.7 Conclusion:

The relationship between catchment characteristics and diurnal fluctuations in hydrological processes is a complex and multifaceted topic. Vegetation, soil properties, topography, and the interaction between groundwater and surface water all play essential roles in modulating diurnal variations in streamflow, ET, and groundwater levels. Wavelet analysis and numerical modelling are valuable tools for studying this relationship and understanding the underlying mechanisms. The diurnal features show seasonal variations and positively correlate with the catchment areas. On the other hand, diurnal lag showed a mix of trends between catchments and depends on many factors like drained area, the distance to the outlet, and the distribution of the channel network. Further research is needed to explore the specific mechanisms and interactions involved in different catchment settings and to develop more accurate and comprehensive models for predicting diurnal fluctuations in hydrological processes.

Chapter 5. Thesis Conclusion and Future Work

5.1 Conclusion

This thesis provided valuable insights into diurnal streamflow signal behaviours within catchments, their spatiotemporal variability, and their connection to the catchment's physical features. It highlights the complex relationships between climatic drivers, catchment characteristics, and diurnal streamflow fluctuations.

Firstly, in Chapter 2, a review of the existing ET measurement techniques, including techniques involving diurnal fluctuations, unveiled potential research gaps that served as the foundation. This chapter aimed to investigate the relationship between diurnal streamflow fluctuations and the potential evapotranspiration rate of riparian vegetation. The chapter introduced a novel technique that provides insights into riparian areas' temporal dynamics during flood recession by assuming a linear correlation between groundwater storage and the active riparian zone area. The estimates of riparian ET generated by this method exhibit a reasonable correlation with the hourly Potential Evapotranspiration (PET) calculated using the FAO 56 approach. This method also revealed the temporal dynamics between riparian zones, groundwater, and streamflow. Also, the method required very few parameters to estimate ET compared to traditional analytical or hydrological methods, thus enhancing its practical applicability and utility.

Another significant goal was to develop advanced automated techniques for rapidly and reliably detecting and analysing diurnal fluctuations in long-term river flow datasets. Manual identification of diurnal fluctuations in long hydrological records had been a significant limitation on large-sample studies of diurnal streamflow fluctuations, prompting the creation of an automated diurnal fluctuation extraction process employing wavelet transform. Chapter 3 addresses this problem through the use of wavelet transform. It introduces a systematic workflow for selecting the most suitable wavelet for our analysis. Discrete Wavelet Transform (DWT) and Continuous Wavelet Transform (CWT) techniques were tested for their ability to reveal time-frequency information

within diurnal flow time series. The effectiveness of the wavelet-aided threshold method is rigorously assessed by comparing it to the commonly utilised moving average technique. The findings reveal that the wavelet-aided detrending scheme excels in capturing abrupt peaks in streamflow, yielding detrended data with a more consistent power spectrum than the moving average. Additionally, the insights gained from CWT were further utilised to develop an algorithm for systematically extracting diurnal episodes from continuous streamflow records. The CWT plots like global wavelet spectrum, wavelet power spectrum, and scale-average variance offer insights into the wavelet powers of the detrended signals in contrast to the noise spectrum, shedding light on their distinct characteristics.

Lastly, a comprehensive study was conducted in Chapter 4, using streamflow records from 217 catchments in New Zealand, which was built on the knowledge acquired in the first research objective and utilising the capabilities of the wavelet transform; this study enabled the extraction and analysis of diurnal patterns and their implications, shedding light on how various physiographical parameters and land characteristics influence diurnal patterns ion streamflow. The study encompassed catchments from several regions across New Zealand to evaluate the impacts of different catchment attributes on diurnal fluctuations. This produced evidence of associations between the morphologies and sizes of catchments and the characteristics of diurnal fluctuations. Notably, the study revealed seasonal variations in diurnal features and provided evidence of a positive correlation between diurnal amplitude and catchment scale.

Catchment shape also influenced the catchment response time. Elongated catchments within the Canterbury region displayed rapid streamflow responses and minimal lag times between transpiration and diurnal fluctuations, in contrast to circular catchments in the Northern regions. These findings contribute significantly to the broader understanding of how catchment characteristics and shape influence the diurnal dynamics of hydrological processes.

In conclusion, addressing the research objectives contributed to a deeper understanding of the diurnal patterns in streamflow. By integrating field observations, advanced analytical methods, and

providing a regional context, this work advances the understanding of diurnal streamflow dynamics. The findings of the thesis offer a solid foundation for future research endeavours in this hydrology domain, with applications extending beyond New Zealand.

5.2 Future Work

It is recommended that future studies focus on the evolution of diurnal signals for multiple-year datasets to establish sound relationships between the diurnal streamflow signals, climatic drivers, and catchment hydrology. The findings of this thesis can be used to automate the process of recording diurnal observations. Automation can enhance the efficiency and accuracy of data collection, ensuring that diurnal signals are detected without requiring extensive manual efforts, and the potential bias might be avoided. This is essential for maintaining long-term datasets that support ongoing research and decision-making processes.

The current research successfully employed automated extraction methods to analyse and compare catchments' shape parameters with their diurnal signatures; however, further investigations are needed. Future research endeavours should extend beyond comparing diurnal fluctuations solely with shape parameters and explore their relationships with other critical catchment features. This includes an in-depth examination of the influence of riparian vegetation, soil drainage characteristics, channel networks, and groundwater reservoirs on diurnal streamflow patterns.

Additionally, integrating diurnal observations into coupled streamflow-groundwater models could improve results. Investigating the impact of diurnal fluctuations on the outflow within a range of simulations with varying land use and land cover scenarios is essential. This research can show how land management practices, such as urbanisation or agriculture, influence diurnal streamflow patterns and help develop sustainable land use policies.

Appendices

Appendix A: Supplementary Results

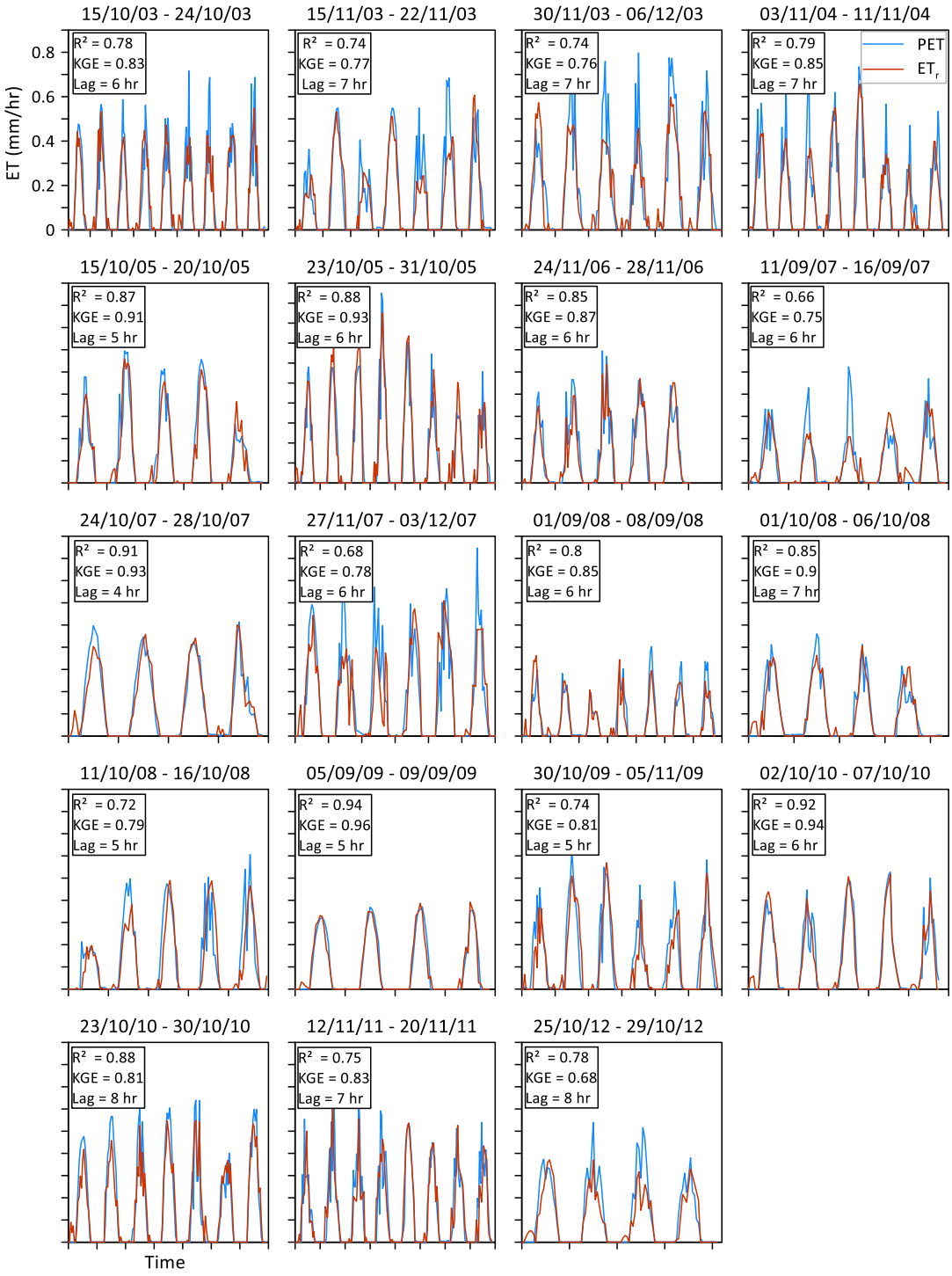

Figure A1 A comparison between hourly PET estimated by FAO 56 and ET_r estimated by the new method during spring months (Sep-Oct-Nov)

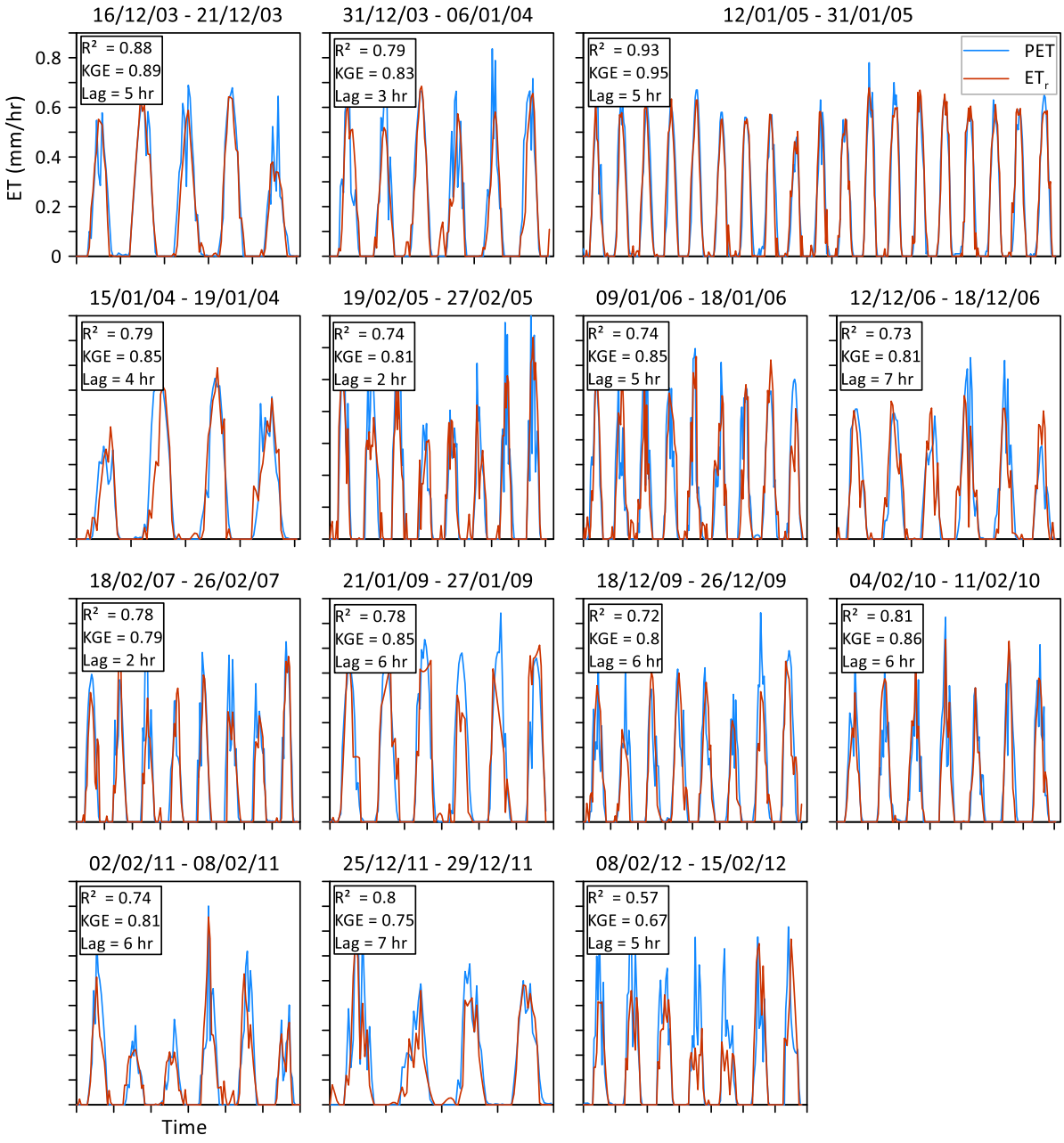

Figure A2 A comparison between hourly PET estimated by FAO 56 and ET_r estimated by the new method during the summer months (Dec-Jan-Feb)

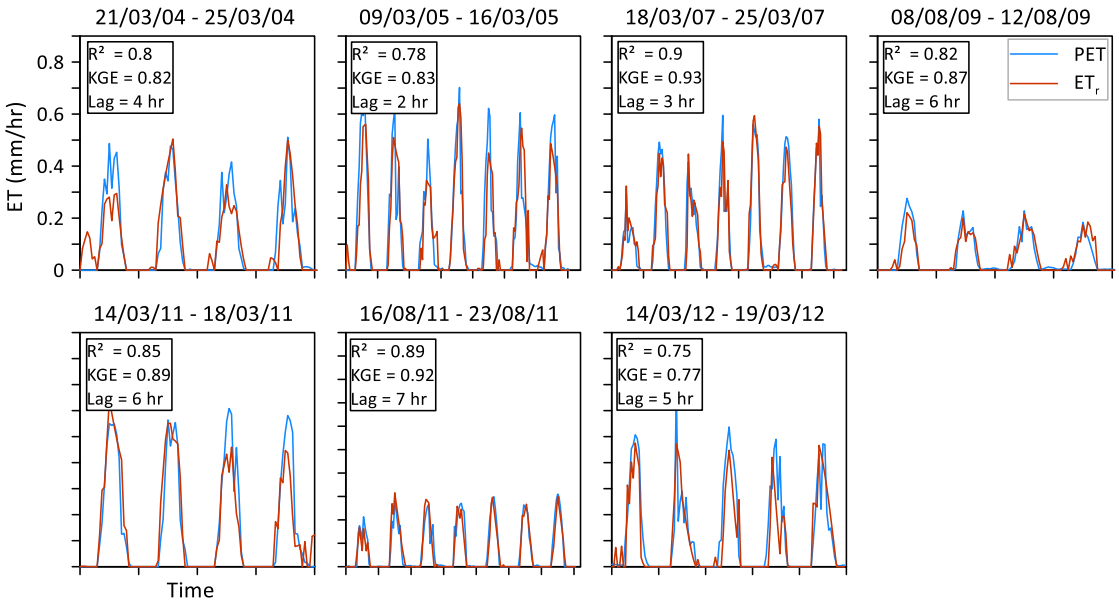

Figure A3 compares hourly PET estimated by FAO 56 and ET_r estimated by the new method during the Winter (Aug) and early Autumn (Mar) months.

Table A1 Statistics for diurnal amplitude across different seasons and regions.

Stat	Season	Regions						Total / Average (m^3/s)
		AKL	NL	BOP	WKT	TDC	CANT	
Count	Winter	9	20	12	11	10	59	121
	Spring	17	33	15	11	18	61	155
	Summer	21	33	17	11	18	62	162
	Autumn	13	32	15	11	14	60	145
Max	Winter	0.0091	0.0526	0.0576	0.0205	0.0340	0.0477	0.0576
	Spring	0.0152	0.0348	0.0729	0.0173	0.0524	0.0420	0.0729
	Summer	0.0163	0.0211	0.0975	0.0109	0.0578	0.0350	0.0975
	Autumn	0.0067	0.0197	0.0372	0.0123	0.0340	0.0389	0.0389
Mean	Winter	0.0050	0.0146	0.0176	0.0079	0.0187	0.0099	0.0148
	Spring	0.0041	0.0083	0.0180	0.0081	0.0200	0.0109	0.0111
	Summer	0.0026	0.0064	0.0216	0.0062	0.0156	0.0107	0.0088
	Autumn	0.0034	0.0061	0.0157	0.0057	0.0126	0.0093	0.0102
Median	Winter	0.0050	0.0089	0.0132	0.0068	0.0162	0.0077	0.0080
	Spring	0.0031	0.0058	0.0142	0.0087	0.0133	0.0087	0.0069
	Summer	0.0014	0.0044	0.0150	0.0046	0.0097	0.0071	0.0056
	Autumn	0.0032	0.0042	0.0141	0.0045	0.0098	0.0064	0.0062
Amp	Winter	1.1674	0.8222	0.7813	0.7050	1.0291	1.0030	0.9384
(%)	Spring	2.2168	1.5370	1.0735	1.1133	0.8598	1.1679	1.3127
	Summer	4.1230	1.6620	1.2938	1.5155	1.1558	1.9898	2.0017
	Autumn	3.1924	1.7350	1.2821	1.2593	1.2316	1.7818	1.7535

Table A2 Datials of the catchments included in the study, along with their physical attributes.

River & Site Name	Region	Area	Perimeter	Stream Length	Longest Flow Path	Form Factor	Elong_Ratio	Circ_ Ratio	Drainage Density
		(km^2)	(km)	(km)	(km)				
Mairangi Bay Stream at Tennis Club	AKL	1.03	5.10	1.42	1.11	1.42	1.03	0.50	1.38
Taiorahi Stream at Westbourne ave	AKL	1.39	6.18	1.60	1.60	1.48	0.83	0.46	1.15
Awaruku stream at Glenvar Road	AKL	2.38	9.78	3.39	2.90	1.79	0.60	0.31	1.42
Vaughn Stream at Lower Weir	AKL	2.44	10.08	3.28	2.87	1.82	0.62	0.30	1.34
Taiaotea stream at Freyberg Park	AKL	2.64	8.82	3.58	2.03	1.53	0.90	0.43	1.36
Motions Stream at Western Springs	AKL	3.55	14.64	4.66	3.78	2.19	0.56	0.21	1.31
Ngakoroa Stream at Mill Rd	AKL	4.95	15.42	7.21	5.22	1.95	0.48	0.26	1.46
Lucas at Gills Road	AKL	6.47	15.12	9.94	3.14	1.68	0.91	0.36	1.54
Newmarket Stream at AYR Street crump weir	AKL	6.86	16.08	8.62	4.76	1.73	0.62	0.33	1.26
Tamahunga River at Quintals Falls	AKL	8.31	18.00	13.21	5.36	1.76	0.61	0.32	1.59
Orewa at Kowhai Ave	AKL	9.59	19.80	15.01	5.16	1.80	0.68	0.31	1.57
Puhinui at Drop Structure	AKL	12.29	24.00	16.31	7.06	1.93	0.56	0.27	1.33
Oteha River at Days Bridge	AKL	12.32	22.32	18.26	6.02	1.79	0.66	0.31	1.48
Meola Creek at Motions Road Weir	AKL	14.89	24.78	20.96	7.62	1.81	0.57	0.30	1.41
Opanuku Stream at Candia Road Bridge	AKL	17.55	25.68	28.30	5.82	1.73	0.81	0.33	1.61
Opanuku at Vintage Reserve	AKL	24.61	33.48	38.02	10.05	1.90	0.56	0.28	1.55
Oratia at Millbrook Road	AKL	28.84	33.36	47.89	8.05	1.75	0.75	0.33	1.66

River & Site Name	Region	Area	Perimeter	Stream Length	Longest Flow Path	Form Factor	Elong_Ratio	Circ_ Ratio	Drainage Density
		(km^2)	(km)	(km)	(km)				
Mangawheau Stream at Weir	AKL	30.93	38.46	51.38	9.54	1.95	0.66	0.26	1.66
Papakura at Great South Road Bridge	AKL	40.41	52.50	64.21	19.37	2.33	0.37	0.18	1.59
Mahurangi Argonaut at College	AKL	48.48	53.82	71.47	12.80	2.18	0.61	0.21	1.47
Kaukapakapa at Taylors	AKL	61.90	49.44	97.90	13.61	1.77	0.65	0.32	1.58
Ararimu River at Old North Rd Bridge	AKL	71.06	54.12	108.24	13.00	1.81	0.73	0.30	1.52
Kourawhero at Farm Bridge	AKL	73.92	52.08	116.69	17.35	1.71	0.56	0.34	1.58
Waiteitei River at Sandersons	AKL	80.88	66.96	124.78	18.47	2.10	0.55	0.23	1.54
Hoteo River at Gubbs	AKL	81.65	57.66	129.30	20.98	1.80	0.49	0.31	1.58
Rangitopuni River at Walkers	AKL	82.20	59.16	127.08	19.18	1.84	0.53	0.30	1.55
Kaipara River at Waimauku	AKL	84.32	57.24	133.38	23.77	1.76	0.44	0.32	1.58
Wairoa River at Tourist Road	AKL	150.62	82.80	245.43	28.70	1.90	0.48	0.28	1.63
Wainui te whara at Mokorua Gorge	BOP	6.31	18.84	9.95	6.68	2.12	0.42	0.22	1.58
Kaiate at Kaiate Falls Rd	BOP	8.39	17.93	13.67	5.96	1.75	0.55	0.33	1.63
Waipapa at Goodall Rd	BOP	9.74	24.00	18.93	8.93	2.17	0.39	0.21	1.94
Waingaehe at SH30	BOP	9.93	20.46	18.58	4.79	1.83	0.74	0.30	1.87
Uretara at Swing Bridge	BOP	10.54	25.56	20.06	8.85	2.22	0.41	0.20	1.90
Puanene at SH2	BOP	11.42	35.40	23.37	12.51	2.96	0.30	0.11	2.05
Te Mania at 87 Sharp Rd	BOP	12.16	22.86	21.39	7.70	1.85	0.51	0.29	1.76
Tuapiro at Farm Bridge	BOP	36.97	40.38	58.10	9.72	1.87	0.71	0.28	1.57
Mangaone at Braemar Rd	BOP	40.29	42.07	62.67	13.65	1.87	0.52	0.29	1.56
Raparapahoe at Above Drop Structure	BOP	51.19	61.87	80.32	23.28	2.44	0.35	0.17	1.57
Waimapu at McCarrolls	BOP	59.11	55.63	100.90	18.92	2.04	0.46	0.24	1.71

River & Site Name	Region	Area	Perimeter	Stream Length	Longest Flow Path	Form Factor	Elong_Ratio	Circ_ Ratio	Drainage Density
		(km^2)	(km)	(km)	(km)				
Nukuhou at Glenholme Rd	BOP	59.16	49.44	101.64	17.10	1.81	0.51	0.30	1.72
Kopurererua at SH29	BOP	60.39	77.29	102.18	27.29	2.81	0.32	0.13	1.69
Utuhina at Depot St	BOP	61.76	55.93	119.49	19.14	2.01	0.46	0.25	1.93
Ngongotaha at SH5	BOP	73.02	53.29	133.20	18.94	1.76	0.51	0.32	1.82
Puarenga at SH30	BOP	78.33	77.95	127.82	13.85	2.48	0.72	0.16	1.63
Waitahanui at Otamarakau Valley Rd	BOP	104.62	88.09	175.55	28.33	2.43	0.41	0.17	1.68
Rangitaiki at SH5	BOP	104.94	70.93	164.40	21.48	1.95	0.54	0.26	1.57
Paraiti (Mangorewa) at Saunders	BOP	192.80	128.60	309.53	42.37	2.61	0.37	0.15	1.61
Tauranga at Omahuru (Ogilvies)	BOP	207.71	109.27	324.29	40.50	2.14	0.40	0.22	1.56
Otara at Browns Bridge	BOP	240.00	118.68	352.56	39.55	2.16	0.44	0.21	1.47
Wairoa at Above Ruahihi	BOP	306.50	137.31	519.51	34.47	2.21	0.57	0.20	1.69
Kaituna at Te Matai	BOP	341.58	183.45	574.96	57.96	2.80	0.36	0.13	1.68
Tarawera at Awakaponga	BOP	515.63	182.36	854.44	51.01	2.27	0.50	0.19	1.66
Waioeka at Cableway	BOP	663.44	212.71	983.09	57.47	2.33	0.51	0.18	1.48
Whakatane at Whakatane (Valley Rd)	BOP	1491.96	320.01	2318.26	105.68	2.34	0.41	0.18	1.55
Rangitaiki at Waiohau Bridge	BOP	2714.82	489.61	4319.14	154.15	2.65	0.38	0.14	1.59
Rangitaiki at Te Teko	BOP	2874.59	533.53	4581.45	176.66	2.81	0.34	0.13	1.59
Kakahu River at Mitchells Weir No.9	CANT	2.86	8.94	4.19	1.91	1.49	1.00	0.45	1.46
Opihi River at Cloudy Peaks	CANT	4.42	11.90	6.45	2.29	1.60	1.03	0.39	1.46
Hook River at Upstream Intake	CANT	10.07	17.88	15.85	5.30	1.59	0.67	0.40	1.57
Waimate Creek at Kelceys Bush Car Park	CANT	10.85	19.20	16.70	5.55	1.64	0.67	0.37	1.54
Barkers Creek at McKeown Road Bridge	CANT	14.40	32.94	26.73	10.69	2.45	0.40	0.17	1.86

River & Site Name	Region	Area	Perimeter	Stream Length	Longest Flow Path	Form Factor	Elong_Ratio	Circ_ Ratio	Drainage Density
		(km^2)	(km)	(km)	(km)				
Lyell Creek at Downstream Warren Creek Confluence	CANT	15.59	24.17	27.68	6.11	1.73	0.73	0.34	1.78
Buchanans Creek at Fletchers Farm	CANT	16.63	34.26	26.48	12.55	2.37	0.37	0.18	1.59
Rocky Gully Stream at Rockburn	CANT	22.92	29.88	36.18	8.34	1.76	0.65	0.32	1.58
Middle Creek at SH1 Bridge	CANT	26.14	32.99	49.51	11.11	1.82	0.52	0.30	1.89
Ohapi Creek at Houstons	CANT	26.72	46.07	45.56	17.32	2.51	0.34	0.16	1.71
Ohapi Creek at Brown Road	CANT	27.88	47.69	48.07	17.95	2.55	0.33	0.15	1.72
Lake Stream at Swingbridge	CANT	30.70	42.18	55.51	14.41	2.15	0.43	0.22	1.81
L-2 River at Pannetts Road	CANT	39.43	44.32	61.97	19.83	1.99	0.36	0.25	1.57
Waihi River at Waimarie	CANT	40.16	39.36	58.97	13.06	1.75	0.55	0.33	1.47
Waihi River at Waimarie	CANT	41.24	41.04	60.96	14.13	1.80	0.51	0.31	1.48
Cam River at Youngs Road	CANT	42.62	54.46	75.64	17.36	2.35	0.42	0.18	1.77
Charwell River at Upstream State Highway 70	CANT	43.14	39.05	60.12	11.52	1.68	0.64	0.36	1.39
Lake Stream at Swingbridge	CANT	43.67	41.28	71.66	7.60	1.76	0.98	0.32	1.64
Lake Stream at Swingbridge	CANT	49.54	53.70	73.08	22.38	2.15	0.35	0.22	1.48
Kowhai River at Below Orange Grove	CANT	55.68	46.84	81.31	14.50	1.77	0.58	0.32	1.46
Lowry Peaks Drain at Longbrook Dairy Br	CANT	57.27	60.37	96.61	12.38	2.25	0.69	0.20	1.69
Flemington Drain at Montgomery Road	CANT	64.40	104.98	103.45	39.17	3.69	0.23	0.07	1.61
Flemington Drain at Montgomery Road	CANT	66.45	113.98	107.55	42.87	3.94	0.21	0.06	1.62
Temuka River at Manse Bridge	CANT	67.94	49.86	97.43	18.98	1.71	0.49	0.34	1.43

River & Site Name	Region	Area	Perimeter	Stream Length	Longest Flow Path	Form Factor	Elong_Ratio	Circ_ Ratio	Drainage Density
		(km^2)	(km)	(km)	(km)				
St Leonards Drain at Above Culvert	CANT	70.77	72.87	115.69	19.57	2.44	0.48	0.17	1.63
Halswell River at Ryans Bridge	CANT	71.82	72.34	112.57	21.33	2.41	0.45	0.17	1.57
Flemington Drain at Wheatstone Road	CANT	72.97	137.73	120.41	52.03	4.55	0.19	0.05	1.65
Heathcote River at Buxton Terrace	CANT	74.35	76.17	112.23	24.19	2.49	0.40	0.16	1.51
Hook River at Hook Beach Road	CANT	82.53	65.16	150.08	24.58	2.02	0.42	0.24	1.82
Hakataramea River at McRaes Gorge	CANT	85.15	64.27	135.65	13.74	1.96	0.76	0.26	1.59
Motunau River at Vulcan Flats	CANT	89.84	68.61	149.97	28.00	2.04	0.38	0.24	1.67
Dry Stream (Hurunui) at Hurunui River Confluence	CANT	91.91	75.56	156.08	27.22	2.22	0.40	0.20	1.70
Lowry Peaks Drain at Longbrook Dairy Br	CANT	98.10	72.03	160.76	17.55	2.05	0.64	0.24	1.64
Percival River at Downstream Chatterton Confluence	CANT	109.08	78.33	176.95	20.66	2.12	0.57	0.22	1.62
Ashley River at Lees Valley	CANT	121.12	68.32	176.08	18.51	1.75	0.67	0.33	1.45
Waitohi River at Lake Sumner Road Bridge	CANT	122.54	89.31	182.17	37.59	2.28	0.33	0.19	1.49
Waikakahi Stream at Te Maiharoa Road Bridge	CANT	133.24	130.67	218.15	45.98	3.19	0.28	0.10	1.64
Otaio River at SH1	CANT	146.27	109.74	247.74	46.69	2.56	0.29	0.15	1.69
Waikari at Pannetts Rd	CANT	148.90	107.48	253.04	39.17	2.48	0.35	0.16	1.70
Tengawai River at Manahune	CANT	154.79	88.69	239.48	20.97	2.01	0.67	0.25	1.55
Omihi Stream (Waipara) at Glen Ray	CANT	158.02	86.19	265.96	29.43	1.93	0.48	0.27	1.68

River & Site Name	Region	Area	Perimeter	Stream Length	Longest Flow Path	Form Factor	Elong_Ratio	Circ_ Ratio	Drainage Density
		(km^2)	(km)	(km)	(km)				
Mandamus River at Tekoa Road Bridge	CANT	169.74	80.31	250.75	25.91	1.74	0.57	0.33	1.48
Parakanoi Drain at Newpark Road	CANT	185.14	123.82	289.01	47.14	2.57	0.33	0.15	1.56
Maerewhenua River at Kellys Gully	CANT	187.02	87.31	265.91	29.43	1.80	0.52	0.31	1.42
Parakanoi Drain at Newpark Road	CANT	193.17	146.19	302.95	56.38	2.97	0.28	0.11	1.57
Parakanoi Drain at Lower Beach Road	CANT	194.51	152.07	305.41	58.82	3.08	0.27	0.11	1.57
Cust Main Drain at Threlkelds Road	CANT	195.10	130.40	325.04	44.05	2.63	0.36	0.14	1.67
Waihao River South Branch at Waihaorunga Road Bridge (R	CANT	197.22	102.78	325.03	37.68	2.06	0.42	0.23	1.65
Mason River at Downstream Lottery River Confluence	CANT	206.75	121.22	314.28	33.90	2.38	0.48	0.18	1.52
Lake Stream at Swingbridge	CANT	217.81	138.30	340.78	73.18	2.64	0.23	0.14	1.56
Okuku River at Fox Creek	CANT	221.71	127.40	321.12	53.59	2.41	0.31	0.17	1.45
Pahau River at Upstream Hurunui Drain Confl (Dalzells B	CANT	235.60	134.05	382.92	54.65	2.46	0.32	0.16	1.63
Hakataramea River at Above Mt Florence	CANT	349.92	123.79	611.98	27.80	1.87	0.76	0.29	1.75
Waipara River at White Gorge	CANT	366.50	127.16	589.19	50.31	1.87	0.43	0.28	1.61
Harts Creek at Timber Yard Road	CANT	390.59	212.50	610.15	83.85	3.03	0.27	0.11	1.56
Pareora River at Huts	CANT	424.94	137.82	680.61	43.76	1.89	0.53	0.28	1.60
Hinds River at Poplar Road	CANT	437.01	191.43	736.29	71.35	2.58	0.33	0.15	1.68
Conway River at SH1	CANT	469.13	164.76	721.37	55.42	2.15	0.44	0.22	1.54

River & Site Name	Region	Area	Perimeter	Stream Length	Longest Flow Path	Form Factor	Elong_Ratio	Circ_ Ratio	Drainage Density
		(km^2)	(km)	(km)	(km)				
Lake Stream at Swingbridge	CANT	469.55	147.56	726.99	52.66	1.92	0.46	0.27	1.55
Lake Stream at Swingbridge	CANT	483.15	173.22	780.13	75.75	2.22	0.33	0.20	1.61
Lake Stream at Swingbridge	CANT	531.73	215.52	858.44	93.15	2.64	0.28	0.14	1.61
Pareora River at SH1	CANT	532.01	170.82	846.15	59.98	2.09	0.43	0.23	1.59
Waihao River at Upstream Bradshaws Bridge	CANT	535.54	219.84	863.67	95.11	2.68	0.27	0.14	1.61
Temuka River at Manse Bridge	CANT	558.05	149.33	946.07	48.48	1.78	0.55	0.31	1.70
Waipara River at Teviotdale Road Bridge	CANT	713.91	213.04	1149.10	74.24	2.25	0.41	0.20	1.61
Waipara River at Teviotdale Road Bridge	CANT	718.06	217.48	1155.67	77.64	2.29	0.39	0.19	1.61
Selwyn River at Ridgens Road	CANT	960.66	261.59	1565.59	101.37	2.38	0.35	0.18	1.63
Lake Stream at Swingbridge	CANT	1136.84	254.54	1805.80	89.79	2.13	0.42	0.22	1.59
Ashley River at SH1 Bridge	CANT	1149.05	277.17	1826.01	97.99	2.31	0.39	0.19	1.59
Whangatane Spillway at Donald Rd	NL	0.59	4.14	0.85	0.85	1.53	1.02	0.43	1.45
Selwyn Swamp at Big Flat Rd	NL	4.33	14.22	6.31	3.97	1.93	0.59	0.27	1.46
Waiotemarama at u/s of FNDC intake	NL	5.49	14.58	8.42	3.41	1.76	0.78	0.32	1.53
Raumanga at Kotuku Dam Intake	NL	8.49	18.54	13.16	5.85	1.79	0.56	0.31	1.55
Maungapareru a at Tyrees Ford	NL	10.15	21.72	16.16	6.86	1.92	0.52	0.27	1.59
Raumanga at Bernard St	NL	16.09	30.66	26.24	8.90	2.16	0.51	0.22	1.63
Waiarohia at Lovers Lane	NL	18.82	27.30	30.46	10.60	1.78	0.46	0.32	1.62
Mangahahuru at County Weir - Kauri	NL	22.13	37.08	34.37	10.59	2.22	0.50	0.20	1.55
Rangitane at Stirling	NL	22.34	32.46	35.33	13.16	1.94	0.41	0.27	1.58
Tarawhataroa at Redan Bridge	NL	23.74	34.25	41.29	10.38	1.98	0.53	0.25	1.74

River & Site Name	Region	Area	Perimeter	Stream Length	Longest Flow Path	Form Factor	Elong_Ratio	Circ_ Ratio	Drainage Density
		(km^2)	(km)	(km)	(km)				
Victoria at Victoria Valley Road	NL	24.84	29.28	37.30	8.88	1.66	0.63	0.36	1.50
Waihoihoi at St Marys Rd	NL	26.96	42.24	42.42	17.05	2.29	0.34	0.19	1.57
Takahue at Crene Road	NL	29.34	36.89	43.26	12.80	1.92	0.48	0.27	1.47
Waipao at Draffin Road	NL	30.27	35.40	49.55	11.84	1.81	0.52	0.30	1.64
Waipapa at Doonside Road	NL	31.31	46.86	53.86	19.18	2.36	0.33	0.18	1.72
Otaika at Kay	NL	35.45	34.62	53.37	11.39	1.64	0.59	0.37	1.51
North at Applecross Rd	NL	38.50	46.98	60.33	19.73	2.14	0.35	0.22	1.57
Hatea at Whareora Rd	NL	41.44	53.81	64.58	13.36	2.36	0.54	0.18	1.56
PuketOtara at BOI Golf Club	NL	42.87	52.97	69.34	20.65	2.28	0.36	0.19	1.62
Ngunguru at Dugmores Rock	NL	45.01	54.53	71.76	18.59	2.29	0.41	0.19	1.59
Ngunguru at Coal Hill Lane Br	NL	46.31	56.57	74.30	20.12	2.35	0.38	0.18	1.60
Otiria at Turntable Hill	NL	47.37	54.29	75.70	18.85	2.23	0.41	0.20	1.60
Ruakaka at Flyger Rd	NL	47.38	45.72	82.35	13.89	1.87	0.56	0.28	1.74
Waitangi at Waimate North Rd	NL	49.67	42.60	79.68	13.64	1.71	0.58	0.34	1.60
Te Puhi at Meffin Rd	NL	53.37	51.83	85.64	18.17	2.00	0.45	0.25	1.60
Ahuroa at Braigh Flats	NL	56.27	57.47	92.12	20.30	2.16	0.42	0.21	1.64
Kerikeri at Peacock Garden	NL	56.83	62.33	158.89	23.00	2.33	0.37	0.18	2.80
Tirohanga at Below Old Mill	NL	57.46	61.43	92.35	21.46	2.29	0.40	0.19	1.61
Kaeo at Waiare Road	NL	72.02	60.71	112.73	17.14	2.02	0.56	0.25	1.57
Mangere at Knights Rd	NL	75.85	55.48	117.91	16.10	1.80	0.61	0.31	1.55
Oruru at Saleyards	NL	79.81	59.09	122.96	18.00	1.87	0.56	0.29	1.54
Hakaru at Topuni Creek Farm	NL	82.24	68.03	128.54	22.67	2.12	0.45	0.22	1.56
Waitangi at SH10	NL	82.62	60.53	132.68	23.73	1.88	0.43	0.28	1.61
Kaeo at Fire Station	NL	88.10	65.27	139.21	21.50	1.96	0.49	0.26	1.58

River & Site Name	Region	Area	Perimeter	Stream Length	Longest Flow Path	Form Factor	Elong_Ratio	Circ_ Ratio	Drainage Density
		(km^2)	(km)	(km)	(km)				
Opouteke at Suspension Br	NL	107.66	70.25	167.73	21.27	1.91	0.55	0.27	1.56
Kaihu at Gorge	NL	115.98	85.96	176.25	27.67	2.25	0.44	0.20	1.52
Waiotu at SH1 Br	NL	121.34	79.79	198.74	24.66	2.04	0.50	0.24	1.64
Victoria at Double Crossing	NL	124.90	70.97	195.42	23.35	1.79	0.54	0.31	1.56
Whakapara at Cableway	NL	162.29	98.03	262.50	25.94	2.17	0.55	0.21	1.62
Waiaruhe at Puketona	NL	173.39	94.67	289.51	24.50	2.03	0.61	0.24	1.67
Hikurangi at Moengawahine	NL	187.76	98.09	312.99	30.84	2.02	0.50	0.25	1.67
Awanui at School Cut	NL	220.29	114.88	351.02	32.19	2.18	0.52	0.21	1.59
Waiharakeke at Willowbank	NL	234.31	123.65	374.31	48.50	2.28	0.36	0.19	1.60
Awanui at Waikuruki	NL	236.42	115.16	377.22	35.56	2.11	0.49	0.22	1.60
Mangakahia at Gorge	NL	243.43	125.68	384.58	30.79	2.27	0.57	0.19	1.58
Punakitere at Taheke	NL	326.40	139.18	540.82	40.68	2.17	0.50	0.21	1.66
Manganui at Permanent Station	NL	409.95	146.50	641.54	51.39	2.04	0.44	0.24	1.56
Wairua at Purua	NL	546.53	163.76	902.87	46.31	1.98	0.57	0.26	1.65
Wairua at Wairua Br	NL	707.01	193.48	1154.62	62.60	2.05	0.48	0.24	1.63
Mangakahia at Titoki Br	NL	809.54	217.17	1306.21	74.92	2.15	0.43	0.22	1.61
Riuwaka North at Littles	TDC	8.23	20.09	11.98	4.77	1.98	0.68	0.26	1.46
Maitai at Avon Tce	TDC	16.70	26.17	23.90	8.43	1.81	0.55	0.31	1.43
Maitai South at above old intake	TDC	18.26	24.23	26.86	6.15	1.60	0.78	0.39	1.47
Maitai at Forks	TDC	34.48	34.07	52.57	7.57	1.64	0.88	0.37	1.52
Roding at Caretakers	TDC	37.57	34.19	51.41	10.57	1.57	0.65	0.40	1.37
Roding at Caretakers	TDC	41.60	36.11	57.37	12.35	1.58	0.59	0.40	1.38
Wakapuaka at Hira	TDC	42.81	37.97	71.43	10.92	1.64	0.68	0.37	1.67
Riuwaka Sth at Moss Bush	TDC	45.84	43.00	68.11	14.08	1.79	0.54	0.31	1.49
Maitai at Avon Tce	TDC	72.70	57.20	109.23	19.90	1.89	0.48	0.28	1.50

River & Site Name	Region	Area	Perimeter	Stream Length	Longest Flow Path	Form Factor	Elong_Ratio	Circ_ Ratio	Drainage Density
		(km^2)	(km)	(km)	(km)				
Tadmor at Mudstone	TDC	84.33	72.75	135.13	28.23	2.23	0.37	0.20	1.60
Riuwaka at Hickmotts	TDC	85.25	63.58	131.66	24.35	1.94	0.43	0.27	1.54
Wai-iti at Belgrove	TDC	91.62	79.71	131.74	20.26	2.35	0.53	0.18	1.44
Anatoki at Happy Sams	TDC	100.03	71.91	137.76	25.17	2.03	0.45	0.24	1.38
Lee at Meads Bridge	TDC	113.20	68.08	162.18	25.96	1.80	0.46	0.31	1.43
Roding at Peninsula	TDC	130.80	77.43	194.18	30.30	1.91	0.43	0.27	1.48
Baton at Baton Flats	TDC	171.79	82.59	236.51	17.50	1.78	0.85	0.32	1.38
Wairoa at Irvines Bridge	TDC	194.74	89.37	283.84	34.40	1.81	0.46	0.31	1.46
Waingaro at Hanging Rock	TDC	212.09	85.04	287.04	37.12	1.65	0.44	0.37	1.35
Tākaka at Harwoods	TDC	259.77	135.24	363.61	33.00	2.37	0.55	0.18	1.40
Wai-iti at Livingston Rd	TDC	288.74	120.53	429.55	39.12	2.00	0.49	0.25	1.49
Aorere at Devils Boots	TDC	377.42	143.21	542.81	48.94	2.08	0.45	0.23	1.44
Wairoa at Irvines	TDC	453.19	160.03	661.32	40.91	2.12	0.59	0.22	1.46
Wangapeka at Walter Peak	TDC	469.79	172.79	681.20	46.25	2.25	0.53	0.20	1.45
Aorere at Devils Boots	TDC	567.99	189.27	844.47	62.81	2.24	0.43	0.20	1.49
Tākaka at Kotinga	TDC	714.92	181.24	1035.50	66.59	1.91	0.45	0.27	1.45
Waimea at TDC Nursery	TDC	768.05	221.44	1131.17	54.53	2.25	0.57	0.20	1.47
Te Tahi at Puketurua	WKT	3.30	14.76	5.70	4.95	2.29	0.41	0.19	1.72
Tapu at Tapu Coroglen Rd	WKT	26.54	33.66	40.76	10.29	1.84	0.57	0.29	1.54
Opitonui at Dstm Awaroa Confluence	WKT	28.81	32.16	45.82	8.33	1.69	0.73	0.35	1.59
Naike at Kaawa School Rd	WKT	29.41	39.12	51.00	12.31	2.04	0.50	0.24	1.73
Waitomo at Aranui Caves Bridge	WKT	36.21	40.51	54.78	11.33	1.90	0.60	0.28	1.51
Orere at Orere Point Rd Bridge	WKT	40.60	43.86	67.40	15.38	1.94	0.47	0.27	1.66
Whakapipi at SH22	WKT	45.63	41.70	75.37	12.48	1.74	0.61	0.33	1.65
Otamakokore at Hossack Rd	WKT	45.70	49.87	73.76	11.63	2.08	0.66	0.23	1.61

River & Site Name	Region	Area	Perimeter	Stream Length	Longest Flow Path	Form Factor	Elong_Ratio	Circ_ Ratio	Drainage Density
		(km^2)	(km)	(km)	(km)				
Wharekawa at Adams Farm Br	WKT	46.50	49.56	69.07	17.77	2.05	0.43	0.24	1.49
Oparau at Langdon Rd	WKT	58.65	64.93	93.32	20.07	2.39	0.43	0.17	1.59
Whareroa at Fish Trap	WKT	59.41	53.83	95.63	18.98	1.97	0.46	0.26	1.61
Awaroa at Hauturu Rd	WKT	71.11	52.93	110.84	17.16	1.77	0.55	0.32	1.56
Matahuru at Myjers Farm	WKT	83.36	66.43	134.74	23.13	2.05	0.45	0.24	1.62
Waitetuna at SH23 Raglan	WKT	86.02	63.19	147.26	18.98	1.92	0.55	0.27	1.71
Piako at Kiwitahi	WKT	108.03	75.07	199.11	28.42	2.04	0.41	0.24	1.84
Oraka at Pinedale	WKT	130.06	105.08	216.85	37.56	2.60	0.34	0.15	1.67

Appendix B: Co- Authorship Forms

THE UNIVERSITY OF WAIKATO
Te Whare Wānanga o Waikato

Co-Authorship Form

Postgraduate Studies Office
Student and Academic Services Division
Wāhanga Rakonga Mātauranga Ākonga
The University of Waikato
Private Bag 3105
Hamilton 3240, New Zealand
Phone +64 7 838 4439
Website: http://www.waikato.ac.nz/sasd/postgraduate/

This form is to accompany the submission of any PhD that contains research reported in published or unpublished co-authored work. **Please include one copy of this form for each co-authored work.** Completed forms should be included in your appendices for all the copies of your thesis submitted for examination and library deposit (including digital deposit).

Please indicate the chapter/section/pages of this thesis that are extracted from a co-authored work and give the title and publication details or details of submission of the co-authored work.

Chapter 2 : Riparian Zone as A Variable Source Area for The Estimation of Evapotranspiration Through the Analysis of Daily Fluctuations in Streamflow , DOI:10.1002/hyp.14708

Nature of contribution by PhD candidate	Conceptualization ,Data Analysis, Computation, Writing and Editing
Extent of contribution by PhD candidate (%)	60

CO-AUTHORS

Name	Nature of Contribution
Ali Shokri	Conceptualization, Editing and Reviewing
Dave Campbell	Conceptualization and Reviewing

Certification by Co-Authors

The undersigned hereby certify that:

- the above statement correctly reflects the nature and extent of the PhD candidate's contribution to this work, and the nature of the contribution of each of the co-authors; and

Name	Signature	Date
Ali Shokri	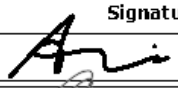	17/10/2023
Dave Campbell		1 Nov 2023

July 2015

THE UNIVERSITY OF WAIKATO
Te Whare Wānanga o Waikato

Co-Authorship Form

Postgraduate Studies Office
Student and Academic Services Division
Wāhanga Rakonga Matauranga Akonga
The University of Waikato
Private Bag 3105
Hamilton 3240, New Zealand
Phone +64 7 838 4439
Website: http://www.waikato.ac.nz/sasd/postgraduate/

This form is to accompany the submission of any PhD that contains research reported in published or unpublished co-authored work. **Please include one copy of this form for each co-authored work**. Completed forms should be included in your appendices for all the copies of your thesis submitted for examination and library deposit (including digital deposit).

Please indicate the chapter/section/pages of this thesis that are extracted from a co-authored work and give the title and publication details or details of submission of the co-authored work.

Chapter 3 Application of Wavelet Transform for Extracting and Analysing Evapotranspiration-Induced Diel Fluctuations in Streamflow Records

Nature of contribution by PhD candidate	Conceptualization ,Data Analysis, Computation, Writing and Editing
Extent of contribution by PhD candidate (%)	75

CO-AUTHORS

Name	Nature of Contribution
Ali Shokri	Conceptualization and Reviewing

Certification by Co-Authors

The undersigned hereby certify that:

- the above statement correctly reflects the nature and extent of the PhD candidate's contribution to this work, and the nature of the contribution of each of the co-authors; and

Name	Signature	Date
Ali Shokri	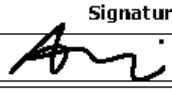	17/10/2023

July 2015

THE UNIVERSITY OF WAIKATO
Te Whare Wānanga o Waikato

Co-Authorship Form

Postgraduate Studies Office
Student and Academic Services Division
Wāhanga Rakonga Matauranga Akonga
The University of Waikato
Private Bag 3105
Hamilton 3240, New Zealand
Phone +64 7 838 4439
Website: http://www.waikato.ac.nz/sasd/postgraduate/

This form is to accompany the submission of any PhD that contains research reported in published or unpublished co-authored work. **Please include one copy of this form for each co-authored work**. Completed forms should be included in your appendices for all the copies of your thesis submitted for examination and library deposit (including digital deposit).

Please indicate the chapter/section/pages of this thesis that are extracted from a co-authored work and give the title and publication details or details of submission of the co-authored work.

Chapter 4: Investigating Seasonal and Spatial Variations in Diurnal Streamflow Fluctuations and Their Correlation with Catchment Attributes

Nature of contribution by PhD candidate	Conceptualization ,Data Analysis, Writing and Editing
Extent of contribution by PhD candidate (%)	70

CO-AUTHORS

Name	Nature of Contribution
Ali Shokri	Conceptualization and Reviewing
Dave Campbell	Conceptualization and Reviewing

Certification by Co-Authors

The undersigned hereby certify that:

- the above statement correctly reflects the nature and extent of the PhD candidate's contribution to this work, and the nature of the contribution of each of the co-authors; and

Name	Signature	Date
Ali Shokri	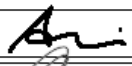	17/10/2023
Dave Campbell		1 Nov 2023

July 2015

References

Abdo, H. G. (2020). Evolving a total-evaluation map of flash flood hazard for hydro-prioritization based on geohydromorphometric parameters and GIS–RS manner in Al-Hussain river basin, Tartous, Syria. *Natural Hazards*, *104*(1), 681–703. https://doi.org/10.1007/s11069-020-04186-3

Adamowski, J., & Sun, K. (2010). Development of a coupled wavelet transform and neural network method for flow forecasting of non-perennial rivers in semi-arid watersheds. *Journal of Hydrology*, *390*(1–2), 85–91. https://doi.org/10.1016/j.jhydrol.2010.06.033

Addison, P. S. (2018). Introduction to redundancy rules: The continuous wavelet transform comes of age. *Philosophical Transactions of the Royal Society A: Mathematical, Physical and Engineering Sciences*, *376*(2126), 20170258. https://doi.org/10.1098/rsta.2017.0258

Ali, R., Silberstein, R., Byrne, J., & Hodgson, G. (2013). Drainage discharge impacts on hydrology and water quality of receiving streams in the wheatbelt of Western Australia. *Environmental Monitoring and Assessment*, *185*(11), 9619–9637. https://doi.org/10.1007/s10661-013-3278-0

Allen, R. G., Pereira, L. S., Howell, T. A., & Jensen, M. E. (2011). Evapotranspiration information reporting: I. Factors governing measurement accuracy. *Agricultural Water Management*, *98*(6), 899–920. https://doi.org/10.1016/j.agwat.2010.12.015

Allen, Richard ; Pereira, L. S. (1991). FAO Irrigation and Drainage Paper No 56. *Applied Ocean Research*. https://doi.org/10.1016/S0141-1187(05)80058-6

Barnard, H. R., Graham, C. B., Van Verseveld, W. J., Brooks, J. R., Bond, B. J., & McDonnell, J. J. (2010). Mechanistic assessment of hillslope transpiration controls of diel subsurface flow: A steady-state irrigation approach. *Ecohydrology*, *3*, 133–142. https://doi.org/10.1002/eco.114

Bibi, T. S., Kara, K. G., Bedada, H. J., & Bededa, R. D. (2023). Application of PCSWMM for assessing the impacts of urbanization and climate changes on the efficiency of stormwater drainage

systems in managing urban flooding in Robe town, Ethiopia. *Journal of Hydrology: Regional Studies*, *45*, 101291. https://doi.org/10.1016/j.ejrh.2022.101291

Blaney, H. F. & others. (1952). *Determining water requirements in irrigated areas from climatological and irrigation data*.

Blume, T., Zehe, E., & Bronstert, A. (2009). Use of soil moisture dynamics and patterns at different spatio-temporal scales for the investigation of subsurface flow processes. *Hydrology and Earth System Sciences*, *13*(7), 1215–1233. https://doi.org/10.5194/hess-13-1215-2009

Bond, B. J., Jones, J. A., Moore, G., Phillips, N., Post, D., & McDonnell, J. J. (2002). The zone of vegetation influence on baseflow revealed by diel patterns of streamflow and vegetation water use in a headwater basin. *Hydrological Processes*, *16*(8), 1671–1677. https://doi.org/10.1002/hyp.5022

Boronina, A., Golubev, S., & Balderer, W. (2005). Estimation of actual evapotranspiration from an alluvial aquifer of the Kouris catchment (Cyprus) using continuous streamflow records. *Hydrological Processes*, *19*(20), 4055–4068. https://doi.org/10.1002/hyp.5871

Bouwer, H. (2002). Artificial recharge of groundwater: Hydrogeology and engineering. *Hydrogeology Journal*, *10*(1), 121–142. https://doi.org/10.1007/s10040-001-0182-4

Bren, L. J. (1997). Effects of slope vegetation removal on the diurnal variations of a small mountain stream. *Water Resources Research*. https://doi.org/10.1029/96WR02648

Briciu, A.-E., Graur, A., Oprea, D. I., & Filote, C. (2019). A Methodology for the Fast Comparison of Streamwater Diurnal Cycles at Two Monitoring Points. *Water*, *11*(12), 2524. https://doi.org/10.3390/w11122524

Burt, T. P. (1979). Diurnal variations in stream discharge and throughflow during a period of low flow. *Journal of Hydrology*, *41*(3–4), 291–301. https://doi.org/10.1016/0022-1694(79)90067-2

Cadol, D., Kampf, S., & Wohl, E. (2012). Effects of evapotranspiration on baseflow in a tropical headwater catchment. *Journal of Hydrology*, *462–463*, 4–14. https://doi.org/10.1016/j.jhydrol.2012.04.060

Caine, N. (1992). Modulation of the diurnal streamflow response by the seasonal snowcover of an alpine basin. *Journal of Hydrology*, *137*(1), 245–260. https://doi.org/10.1016/0022-1694(92)90059-5

Castellini, M., Di Prima, S., Moret-Fernández, D., & Lassabatere, L. (2021). Rapid and accurate measurement methods for determining soil hydraulic properties: A review. *Journal of Hydrology and Hydromechanics*, *69*(2), 121–139. https://doi.org/10.2478/johh-2021-0002

Černohous, V., & Šach, F. (2008). Daily baseflow variations and forest evapotranspiration. *Ekológia (Bratislava)*, *27*(2), 189–195.

Chen, K., Tetzlaff, D., Goldhammer, T., Freymueller, J., Wu, S., Andrew Smith, A., Schmidt, A., Liu, G., Venohr, M., & Soulsby, C. (2023). Synoptic water isotope surveys to understand the hydrology of large intensively managed catchments. *Journal of Hydrology*, *623*, 129817. https://doi.org/10.1016/j.jhydrol.2023.129817

Chen, W.-K. S. and Y. (2020). Modelling of evaporation from free water surface. *Geomechanics and Engineering*, *21*(3), 237–245. https://doi.org/10.12989/GAE.2020.21.3.237

Chiew, F. H. S., Whetton, P. H., McMahon, T. A., & Pittock, A. B. (1995). Simulation of the impacts of climate change on runoff and soil moisture in Australian catchments. *Journal of Hydrology*, *167*(1–4), 121–147. https://doi.org/10.1016/0022-1694(94)02649-V

Chong, K. L., Lai, S. H., & El-Shafie, A. (2019). Wavelet Transform Based Method for River Stream Flow Time Series Frequency Analysis and Assessment in Tropical Environment. *Water Resources Management*, *33*(6), 2015–2032. https://doi.org/10.1007/s11269-019-02226-7

Consoli, S. (2011). Evapotranspiration Estimation Using Micrometeorological Techniques. In G. Gerosa (Ed.), *Evapotranspiration—From Measurements to Agricultural and Environmental Applications*. InTech. https://doi.org/10.5772/17130

Cuevas, J., Calvo, M., Little, C., Pino, M., & Dassori, P. (2010). Are diurnal fluctuations in streamflow real? *Journal of Hydrology and Hydromechanics*, *58*(3). https://doi.org/10.2478/v10098-010-0014-0

Cuevas, J. G., Arumí, J. L., Zúñiga-Feest, A., & Little, C. (2018). An unusual kind of diurnal streamflow variation. *Journal of Hydrology and Hydromechanics*, *66*(1), 32–42. https://doi.org/10.1515/johh-2017-0041

Czikowsky, M. J., & Fitzjarrald, D. R. (2004). Evidence of seasonal changes in evapotranspiration in eastern U.S. hydrological records. *Journal of Hydrometeorology*, *5*(5), 974–988. https://doi.org/10.1175/1525-7541(2004)005<0974:EOSCIE>2.0.CO;2

Daubechies, I. (1988). Orthonormal bases of compactly supported wavelets. *Communications on Pure and Applied Mathematics*, *41*(7), 909–996. https://doi.org/10.1002/cpa.3160410705

Debnath, L., & Shah, F. A. (2017). *Lecture Notes on Wavelet Transforms*. Springer International Publishing. https://doi.org/10.1007/978-3-319-59433-0

Denham, S. O., Barnes, M. L., Chang, Q., Korolev, M., Wood, J. D., Oishi, A. C., Shay, K. O., Stoy, P. C., Chen, J., & Novick, K. A. (2023). The Rate of Canopy Development Modulates the Link Between the Timing of Spring Leaf Emergence and Summer Moisture. *Journal of Geophysical Research: Biogeosciences*, *128*(4), e2022JG007217. https://doi.org/10.1029/2022JG007217

Dolan, T. J., Hermann, A. J., Bayley, S. E., & Zoltek, J. (1984). Evapotranspiration of a Florida, U.S.A., freshwater wetland. *Journal of Hydrology*, *74*(3–4), 355–371. https://doi.org/10.1016/0022-1694(84)90024-6

Ehlers, W. (1991). Leaf area and transpiration efficiency during different growth stages in oats. *The Journal of Agricultural Science*, *116*(2), 183–190. https://doi.org/10.1017/S0021859600077571

Fahle, M., & Dietrich, O. (2014). Estimation of evapotranspiration using diurnal groundwater level fluctuations: Comparison of different approaches with groundwater lysimeter data. *Water Resources Research*, *50*(1), 273–286. https://doi.org/10.1002/2013WR014472

Fenner, W., Dallacort, R., Faria Junior, C. A., Freitas, P. S. L. D., Queiroz, T. M. D., & Santi, A. (2019). Development, calibration and validation of weighing lysimeters for measurement of evapotranspiration of crops. *Revista Brasileira de Engenharia Agrícola e Ambiental*, *23*(4), 297–302. https://doi.org/10.1590/1807-1929/agriambi.v23n4p297-302

Foken, T. (2008). THE ENERGY BALANCE CLOSURE PROBLEM: AN OVERVIEW. *Ecological Applications*, *18*(6), 1351–1367. https://doi.org/10.1890/06-0922.1

Fonley, M., Mantilla, R., Small, S. J., & Curtu, R. (2016). On the propagation of diel signals in river networks using analytic solutions of flow equations. *Hydrology and Earth System Sciences*, *20*(7), 2899–2912. https://doi.org/10.5194/hess-20-2899-2016

Fourati, W., Kammoun, F., & Bouhlel, M. S. (2005). Medical Image Denoising Using Wavelet Thresholding. *Journal of Testing and Evaluation*, *33*(5), 364–369. https://doi.org/10.1520/JTE12481

Gao, H.-Y. (1998). Wavelet Shrinkage Denoising Using the Non-Negative Garrote. *Journal of Computational and Graphical Statistics*, *7*(4), 469–488. https://doi.org/10.1080/10618600.1998.10474789

Geisler, E. T. (2016). *Riparian zone evapotranspiration using streamflow diel signals*. Boise State University.

Gelybó, G., Barcza, Z., Kern, A., & Kljun, N. (2013). Effect of spatial heterogeneity on the validation of remote sensing based GPP estimations. *Agricultural and Forest Meteorology*, *174*, 43–53.

Goodrich, D. C., Scott, R., Qi, J., Goff, B., Unkrich, C. L., Moran, M. S., Williams, D., Schaeffer, S., Snyder, K., MacNish, R., Maddock, T., Pool, D., Chehbouni, A., Cooper, D. I., Eichinger, W. E., Shuttleworth, W. J., Kerr, Y., Marsett, R., & Ni, W. (2000). Seasonal estimates of riparian evapotranspiration using remote and in situ measurements. *Agricultural and Forest Meteorology*, *105*(1–3), 281–309. https://doi.org/10.1016/S0168-1923(00)00197-0

Graham, C. B., Barnard, H. R., Kavanagh, K. L., & Mcnamara, J. P. (2012). *Catchment scale controls the temporal connection of transpiration and diel fl uctuations in stream fl ow*. https://doi.org/10.1002/hyp

Graham, C. B., Barnard, H. R., Kavanagh, K. L., & McNamara, J. P. (2013). Catchment scale controls the temporal connection of transpiration and diel fluctuations in streamflow: TRANSPIRATION AND DIEL FLUCTUATIONS IN STREAMFLOW. *Hydrological Processes*, *27*(18), 2541–2556. https://doi.org/10.1002/hyp.9334

Gribovszki, Z., Kalicz, P., Kucsara, M., Szilágyi, J., & Vig, P. (2008). Evapotranspiration Calculation on the Basis of the Riparian Zone Water Balance. *Acta Silvatica et Lignaria Hungarica*.

Gribovszki, Z., Kalicz, P., Szilágyi, J., & Kucsara, M. (2008). Riparian zone evapotranspiration estimation from diurnal groundwater level fluctuations. *Journal of Hydrology*, *349*(1–2), 6–17. https://doi.org/10.1016/j.jhydrol.2007.10.049

Gribovszki, Z., Szilágyi, J., & Kalicz, P. (2010). Diurnal fluctuations in shallow groundwater levels and streamflow rates and their interpretation—A review. *Journal of Hydrology*, *385*(1–4), 371–383. https://doi.org/10.1016/j.jhydrol.2010.02.001

Grinsted, A., Moore, J. C., & Jevrejeva, S. (2004). *Nonlinear Processes in Geophysics Application of the cross wavelet transform and wavelet coherence to geophysical time series* (Vol. 11, pp. 561–566). http://www.pol.ac.uk/home/research/waveletcoherence/

Hamilton, A. S., & Moore, R. D. (2012). Quantifying Uncertainty in Streamflow Records. *Canadian Water Resources Journal / Revue Canadienne Des Ressources Hydriques*, *37*(1), 3–21. https://doi.org/10.4296/cwrj3701865

Hao, X., Zhang, S., Li, W., Duan, W., Fang, G., Zhang, Y., & Guo, B. (2018). The Uncertainty of Penman-Monteith Method and the Energy Balance Closure Problem. *Journal of Geophysical Research: Atmospheres*, *123*(14), 7433–7443. https://doi.org/10.1029/2018JD028371

Haslinger, K., Koffler, D., Schöner, W., & Laaha, G. (2014). Exploring the link between meteorological drought and streamflow: Effects of climate-catchment interaction. *Water Resources Research*, *50*(3), 2468–2487. https://doi.org/10.1002/2013WR015051

Horner, I., Renard, B., Le Coz, J., Branger, F., McMillan, H. K., & Pierrefeu, G. (2018). Impact of Stage Measurement Errors on Streamflow Uncertainty. *Water Resources Research*, *54*(3), 1952–1976. https://doi.org/10.1002/2017WR022039

Horton, R. E. (1932). Drainage-basin characteristics. *Transactions, American Geophysical Union*, *13*(1), 350. https://doi.org/10.1029/TR013i001p00350

Huang, J., Cao, L., Yu, F., Liu, X., & Wang, L. (2021). Groundwater Drought and Cycles in Xuchang City, China. *Frontiers in Earth Science*, *9*, 736305. https://doi.org/10.3389/feart.2021.736305

Johnson, B., Malama, B., Barrash, W., & Flores, A. N. (2013). Recognizing and modeling variable drawdown due to evapotranspiration in a semiarid riparian zone considering local differences in vegetation and distance from a river source. *Water Resources Research*. https://doi.org/10.1002/wrcr.20122

Johnstone, I. M., & Silverman, B. W. (1997). Wavelet Threshold Estimators for Data with Correlated Noise. *Journal of the Royal Statistical Society. Series B (Methodological)*, *59*(2), 319–351.

Jutebring Sterte, E., Lidman, F., Lindborg, E., Sjöberg, Y., & Laudon, H. (2021). How catchment characteristics influence hydrological pathways and travel times in a boreal landscape. *Hydrology and Earth System Sciences*, *25*(4), 2133–2158. https://doi.org/10.5194/hess-25-2133-2021

Kellogg, D. Q., Gold, A. J., Groffman, P. M., Stolt, M. H., & Addy, K. (2008). Riparian Ground-Water Flow Patterns Using Flownet Analysis: Evapotranspiration-Induced Upwelling and Implications for N Removal 1. *JAWRA Journal of the American Water Resources Association*, *44*(4), 1024–1034. https://doi.org/10.1111/j.1752-1688.2008.00218.x

Khadka, D. (2020). *Effects of scale and spatial variability on streamflows in NZ Alpine catchments.* https://doi.org/10.26021/11371

Khanmohammadi, N., Rezaie, H., Montaseri, M., & Behmanesh, J. (2017). The effect of different meteorological parameters on the temporal variations of reference evapotranspiration. *Environmental Earth Sciences*, *76*(15), 540. https://doi.org/10.1007/s12665-017-6871-7

Kirchner, J. W. (2009). Catchments as simple dynamical systems: Catchment characterization, rainfall-runoff modeling, and doing hydrology backward. *Water Resources Research*, *45*(2). https://doi.org/10.1029/2008WR006912

Kirchner, J. W., Godsey, S. E., Solomon, M., Osterhuber, R., McConnell, J. R., & Penna, D. (2020). The pulse of a montane ecosystem: Coupling between daily cycles in solar flux, snowmelt, transpiration, groundwater, and streamflow at Sagehen Creek and Independence Creek, Sierra Nevada, USA. *Hydrology and Earth System Sciences*, *24*(11), 5095–5123. https://doi.org/10.5194/hess-24-5095-2020

Koch, H., Liersch, S., de Azevedo, J. R. G., Silva, A. L. C., & Hattermann, F. F. (2018). Assessment of observed and simulated low flow indices for a highly managed river basin. *Hydrology Research*, *49*(6), 1831–1846. https://doi.org/10.2166/nh.2018.168

Kovář, P., & Bačinová, H. (2015). Impact of evapotranspiration on diurnal discharge fluctuation determined by the fourier series model in dry periods. *Soil and Water Research*, *10*(4), 210–217. https://doi.org/10.17221/122/2015-SWR

Lascano, R. J., Goebel, T. S., Booker, J., Baker, J. T., & Gitz III, D. C. (2016). The Stem Heat Balance Method to Measure Transpiration: Evaluation of a New Sensor. *Agricultural Sciences*. https://doi.org/10.4236/as.2016.79057

Legarda Garzon, L. F., Johnson, M. F., Mount, N., & Gomez, H. (2023). *Exploring the Effects of Catchment Morphometry on Overland Flow Response to Extreme Rainfall Using a 2d Hydraulic-Hydrological Model (Iber)* (SSRN Scholarly Paper No. 4496628). https://doi.org/10.2139/ssrn.4496628

Liu, Z. (2022). Estimating land evapotranspiration from potential evapotranspiration constrained by soil water at daily scale. *Science of The Total Environment*, *834*, 155327. https://doi.org/10.1016/j.scitotenv.2022.155327

Loheide II, S. P. (2008). A method for estimating subdaily evapotranspiration of shallow groundwater using diurnal water table fluctuations. *Ecohydrology*, *1*(1), 59–66. https://doi.org/10.1002/eco.7

Lu, J., Sun, G., McNulty, S. G., & Amatya, D. M. (2005). A COMPARISON OF SIX POTENTIAL EVAPOTRANSPIRATION METHODS FOR REGIONAL USE IN THE SOUTHEASTERN UNITED STATES. *Journal of the American Water Resources Association*, *41*(3), 621–633. https://doi.org/10.1111/j.1752-1688.2005.tb03759.x

Lukas, V., Novák, J., Neudert, L., Svobodova, I., Rodriguez-Moreno, F., Edrees, M., & Kren, J. (2016). The combination of UAV survey and Landsat imagery for monitoring of crop vigor in precision

agriculture. *International Archives of the Photogrammetry, Remote Sensing and Spatial Information Sciences - ISPRS Archives*, *41*(July), 953–957. https://doi.org/10.5194/isprsarchives-XLI-B8-953-2016

Lundquist, J. D., & Cayan, D. R. (2002). Seasonal and Spatial Patterns in Diurnal Cycles in Streamflow in the Western United States. *Journal of Hydrometeorology*, *3*(5), 591–603. https://doi.org/10.1175/1525-7541(2002)003<0591:saspid>2.0.co;2

Lundquist, J., & Dettinger, M. (2003). Linking diurnal cycles of river flow to interannual variations in climate. *83rd Meeting of the American Meteorological Society. 17th Conference. on Hydrology. Long Beach, California*.

Lyne, V. D., & Hollick, M. (1979). Stochastic time-variable rainfall-runoff modelling. *In Institute of Engineers Australia National Conference*.

Mallat, S. (2009). *A Wavelet Tour of Signal Processing*. Elsevier. https://doi.org/10.1016/B978-0-12-374370-1.X0001-8

Martí, E., Fisher, S. G., Schade, J. D., & Grimm, N. B. (2000). Flood Frequency and Stream–Riparian Linkages in Arid Lands. In *Streams and Ground Waters* (pp. 111–136). Elsevier. https://doi.org/10.1016/B978-012389845-6/50005-3

McGlynn, B. L., McDonnell, J. J., Seibert, J., & Kendall, C. (2004). Scale effects on headwater catchment runoff timing, flow sources, and groundwater-streamflow relations. *Water Resources Research*, *40*(7), 2003WR002494. https://doi.org/10.1029/2003WR002494

McMillan, H. K., Gnann, S. J., & Araki, R. (2022). Large Scale Evaluation of Relationships Between Hydrologic Signatures and Processes. *Water Resources Research*, *58*(6). https://doi.org/10.1029/2021WR031751

McMillan, H., Seibert, J., Petersen-Overleir, A., Lang, M., White, P., Snelder, T., Rutherford, K., Krueger, T., Mason, R., & Kiang, J. (2017). How uncertainty analysis of streamflow data can

reduce costs and promote robust decisions in water management applications. *Water Resources Research*, *53*(7), 5220–5228. https://doi.org/10.1002/2016WR020328

Miller, V. C. (1953). *A quantitative geomorphic study of drainage basin characteristics in the Clinch Mountain area, Virginia and Tennessee* (Vol. 3). Columbia University New York.

Misiti, Michel. (2007). *Wavelets and their applications*. ISTE.

Mlamla, S., Kakembo, V., & Barasa, B. (2022). Hydrologic response to land use/cover changes and *Pteronia incana* shrub invasion in Keiskamma catchment, Eastern Cape Province, South Africa. *Geocarto International*, *37*(25), 10229–10253. https://doi.org/10.1080/10106049.2022.2032395

Monteith, J. L. (1965). Evaporation and environment. *Symposia of the Society for Experimental Biology*, *19*, 205–234.

Morovati, K., Shi, L., Pokhrel, Y., Wu, M., Someth, P., Ly, S., & Tian, F. (2024). *On the Cause of Large Daily River Flow Fluctuations in the Mekong River*. Rivers and Lakes/Modelling approaches. https://doi.org/10.5194/hess-2024-96

Mutzner, R., Weijs, S. V., Tarolli, P., Calaf, M., Oldroyd, H. J., & Parlange, M. B. (2015). Controls on the diurnal streamflow cycles in two subbasins of an alpine headwater catchment. *Water Resources Research*, *51*(5), 3403–3418. https://doi.org/10.1002/2014WR016581

Nachabe, M., Shah, N., Ross, M., & Vomacka, J. (2005). Evapotranspiration of Two Vegetation Covers in a Shallow Water Table Environment. *Soil Science Society of America Journal*, *69*(2), 492. https://doi.org/10.2136/sssaj2005.0492

Nathan, R. J., & McMahon, T. A. (1992). Estimating low flow characteristics in ungauged catchments. *Water Resources Management*, *6*(2), 85–100. https://doi.org/10.1007/BF00872205

Oliveira, P. J. C., Davin, E. L., Levis, S., & Seneviratne, S. I. (2011). Vegetation-mediated impacts of trends in global radiation on land hydrology: A global sensitivity study. *Global Change Biology*, *17*(11), 3453–3467. https://doi.org/10.1111/j.1365-2486.2011.02506.x

Patel, K. F., Fansler, S. J., Campbell, T. P., Bond-Lamberty, B., Smith, A. P., RoyChowdhury, T., McCue, L. A., Varga, T., & Bailey, V. L. (2021). Soil texture and environmental conditions influence the biogeochemical responses of soils to drought and flooding. *Communications Earth & Environment*, *2*(1), 127. https://doi.org/10.1038/s43247-021-00198-4

Peng, L., Zeng, Z., Wei, Z., Chen, A., Wood, E. F., & Sheffield, J. (2019). Determinants of the ratio of actual to potential evapotranspiration. *Global Change Biology*, *25*(4), 1326–1343. https://doi.org/10.1111/gcb.14577

Penman, H. L. (1948). Natural evaporation from open water, bare soil and grass. *Proceedings of the Royal Society of London. Series A. Mathematical and Physical Sciences*, *193*(1032), 120–145.

Percival, D. B. (2008). Analysis of Geophysical Time Series Using Discrete Wavelet Transforms: An Overview. In R. V. Donner & S. M. Barbosa (Eds.), *Nonlinear Time Series Analysis in the Geosciences: Applications in Climatology, Geodynamics and Solar-Terrestrial Physics* (pp. 61–79). Springer. https://doi.org/10.1007/978-3-540-78938-3_4

Pimentel, R., Arheimer, B., Crochemore, L., Andersson, J. C. M., Pechlivanidis, I. G., & Gustafsson, D. (2023). Which Potential Evapotranspiration Formula to Use in Hydrological Modeling World-Wide? *Water Resources Research*, *59*(5), e2022WR033447. https://doi.org/10.1029/2022WR033447

Priestley, C. H. B., & Taylor, R. J. (1972). On the assessment of surface heat flux and evaporation using large-scale parameters. *Monthly Weather Review*, *100*(2), 81–92.

Reigner, I. C. (1966). A method of estimating streamflow loss by evapotranspiration from the riparian zone. *Forest Science*, *12*(2), 130–139. https://doi.org/10.1093/forestscience/12.2.130

Rhif, M., Ben Abbes, A., Farah, I. R., Martínez, B., & Sang, Y. (2019). Wavelet Transform Application for/in Non-Stationary Time-Series Analysis: A Review. *Applied Sciences*, *9*(7), Article 7. https://doi.org/10.3390/app9071345

Rodrigues, A. L. M., Reis, G. B., Dos Santos, M. T., Da Silva, D. D., Dos Santos, V. J., De Siqueira Castro, J., & Calijuri, M. L. (2019). Influence of land use and land cover's change on the hydrological regime at a Brazilian southeast urbanized watershed. *Environmental Earth Sciences*, *78*(20), 595. https://doi.org/10.1007/s12665-019-8601-9

Rugenski, A. T., Minshall, G. W., & Hauer, F. R. (2017). Riparian Processes and Interactions. In *Methods in Stream Ecology* (pp. 83–111). Elsevier. https://doi.org/10.1016/B978-0-12-813047-6.00006-1

Sang, Y.-F. (2012). A Practical Guide to Discrete Wavelet Decomposition of Hydrologic Time Series. *Water Resources Management*, *26*(11), 3345–3365. https://doi.org/10.1007/s11269-012-0075-4

Sang, Y.-F. (2013). A review on the applications of wavelet transform in hydrology time series analysis. *Atmospheric Research*, *122*, 8–15. https://doi.org/10.1016/j.atmosres.2012.11.003

Santos, C. A. G., & de Morais, B. S. (2013). Identification of precipitation zones within São Francisco River basin (Brazil) by global wavelet power spectra. *Hydrological Sciences Journal*, *58*(4), 789–796. https://doi.org/10.1080/02626667.2013.778412

Santos, L. C., Dos Santos, F. N., Morais, R., & Duarte, C. (2021). Potential Non-Invasive Technique for Accessing Plant Water Contents Using a Radar System. *Agronomy*, *11*(2), 279. https://doi.org/10.3390/agronomy11020279

Sarwar, M. W., Campbell, D. I., & Shokri, A. (2022). Riparian zone as a variable source area for the estimation of evapotranspiration through the analysis of daily fluctuations in streamflow. *Hydrological Processes*, *36*(10), e14708. https://doi.org/10.1002/hyp.14708

Satchithanantham, S., Wilson, H. F., & Glenn, A. J. (2017). Contrasting patterns of groundwater evapotranspiration in grass and tree dominated riparian zones of a temperate agricultural catchment. *Journal of Hydrology*. https://doi.org/10.1016/j.jhydrol.2017.04.016

Schilling, K. E., Jindal, P., Basu, N. B., & Helmers, M. J. (2012). Impact of artificial subsurface drainage on groundwater travel times and baseflow discharge in an agricultural watershed, Iowa (USA). *Hydrological Processes*, *26*(20), 3092–3100. https://doi.org/10.1002/hyp.8337

SCHUMM, S. A. (1956). EVOLUTION OF DRAINAGE SYSTEMS AND SLOPES IN BADLANDS AT PERTH AMBOY, NEW JERSEY. *GSA Bulletin*, *67*(5), 597–646. https://doi.org/10.1130/0016-7606(1956)67[597:EODSAS]2.0.CO;2

Schwab, M., Klaus, J., Pfister, L., & Weiler, M. (2016). Diel discharge cycles explained through viscosity fluctuations in riparian inflow. *Water Resources Research*, *52*(11), 8744–8755. https://doi.org/10.1002/2016WR018626

Shiklomanov, I. A. (2000). Appraisal and Assessment of World Water Resources. *Water International*, *25*(1), 11–32. https://doi.org/10.1080/02508060008686794

Shrestha, P. (2021). Clouds and Vegetation Modulate Shallow Groundwater Table Depth. *Journal of Hydrometeorology*, *22*(4), 753–763. https://doi.org/10.1175/JHM-D-20-0171.1

Sinha, S. K., Routh, P. S., Anno, P. D., & Castagna, J. P. (2003). Time-frequency attribute of seismic data using continuous wavelet transform. *SEG Technical Program Expanded Abstracts 2003*, 1481–1484. https://doi.org/10.1190/1.1817573

Smith, L. C., Turcotte, D. L., & Isacks, B. L. (1998). Stream flow characterization and feature detection using a discrete wavelet transform. *Hydrological Processes*, *12*(2), 233–249. https://doi.org/10.1002/(SICI)1099-1085(199802)12:2<233::AID-HYP573>3.0.CO;2-3

Stannard, D. I. (1988). *Use of a hemispherical chamber for measurement of evapotranspiration* (Report Nos. 88–452; Open-File Report). USGS Publications Warehouse. https://doi.org/10.3133/ofr88452

Subramanya, K. (2008). *Engineering hydrology*. McGraw-Hill.

Széles, B., Broer, M., Parajka, J., Hogan, P., Eder, A., Strauss, P., & Blöschl, G. (2018). Separation of Scales in Transpiration Effects on Low Flows: A Spatial Analysis in the Hydrological Open Air Laboratory. *Water Resources Research*, *54*(9), 6168–6188. https://doi.org/10.1029/2017WR022037

Szilagyi, J., Gribovszki, Z., & Kalicz, P. (2007). Estimation of catchment-scale evapotranspiration from baseflow recession data: Numerical model and practical application results. *Journal of Hydrology*, *336*(1–2), 206–217. https://doi.org/10.1016/j.jhydrol.2007.01.004

Szilágyi, J., Gribovszki, Z., Kalicz, P., & Kucsara, M. (2008). On diurnal riparian zone groundwater-level and streamflow fluctuations. *Journal of Hydrology*, *349*(1), 1–5. https://doi.org/10.1016/j.jhydrol.2007.09.014

Tallaksen, L. M. (1995). A review of baseflow recession analysis. *Journal of Hydrology*, *165*(1–4), 349–370. https://doi.org/10.1016/0022-1694(94)02540-R

Torrence, C., & Compo, G. P. (1998). A Practical Guide to Wavelet Analysis. *Bulletin of the American Meteorological Society*, *79*(1), 61–78. https://doi.org/10.1175/1520-0477(1998)079<0061:APGTWA>2.0.CO;2

Troxell, H. C. (1936). The diurnal fluctuation in the ground-water and flow of the santa ana river and its meaning. *Transactions, American Geophysical Union*, *17*(2), 496. https://doi.org/10.1029/TR017i002p00496

Tschinkel, H. M. (1963). Short-term fluctuation in streamflow as related to evaporation and transpiration. *Journal of Geophysical Research*, *68*(24), 6459–6469. https://doi.org/10.1029/JZ068i024p06459

Van Camp, M., De Viron, O., Pajot-Métivier, G., Casenave, F., Watlet, A., Dassargues, A., & Vanclooster, M. (2016). Direct measurement of evapotranspiration from a forest using a superconducting gravimeter. *Geophysical Research Letters*, *43*(19). https://doi.org/10.1002/2016GL070534

Venturini, V., Walker, E., Fonnegra Mora, D. C., & Fagioli, G. (2022). Effect of the net radiation proxies on maize and soya evapotranspiration estimation using machine learning methods. *AgriScientia*, *39*(2), 1–17. https://doi.org/10.31047/1668.298x.v39.n2.37104

Vereecken, H. (2023, May 15). *On the hydrology of soils in the Earth System*. https://doi.org/10.5194/egusphere-egu23-1156

Vetterli, M., & Herley, C. (1992). Wavelets and filter banks: Theory and design. *IEEE Transactions on Signal Processing*, *40*(9), 2207–2232. https://doi.org/10.1109/78.157221

Wagener, T., Sivapalan, M., Troch, P., & Woods, R. (2007). Catchment Classification and Hydrologic Similarity: Catchment classification and hydrologic similarity. *Geography Compass*, *1*(4), 901–931. https://doi.org/10.1111/j.1749-8198.2007.00039.x

Wang, T., Istanbulluoglu, E., Lenters, J., & Scott, D. (2009). On the role of groundwater and soil texture in the regional water balance: An investigation of the Nebraska Sand Hills, USA: ON THE ROLE OF GROUNDWATER AND SOIL TEXT. *Water Resources Research*, *45*(10). https://doi.org/10.1029/2009WR007733

Weisman, R. N. (1977). The effect of evapotranspiration on streamflow recession. *Hydrological Sciences Bulletin*, *22*(3), 371–377. https://doi.org/10.1080/02626667709491731

White, W. N. (1932). A method of estimating ground-water supplies based on discharge by plants and evaporation from soil: Results of investigations in Escalante Valley, Utah. In *Water Supply Paper: Vol. A* (Issue 659). US Geological Survey. https://doi.org/10.3133/wsp659A

Wilcock, R. J., Betteridge, K., Shearman, D., Fowles, C. R., Scarsbrook, M. R., Thorrold, B. S., & Costall, D. (2009). Riparian protection and on-farm best management practices for restoration of a lowland stream in an intensive dairy farming catchment: A case study. *New Zealand Journal of Marine and Freshwater Research*, *43*(3), 803–818. https://doi.org/10.1080/00288330909510042

Woelber, B., Maneta, M. P., Harper, J., Jencso, K. G., Gardner, W. P., Wilcox, A. C., & López-Moreno, I. (2018). The influence of diurnal snowmelt and transpiration on hillslope throughflow and stream response. *Hydrology and Earth System Sciences*, *22*(8), 4295–4310. https://doi.org/10.5194/hess-22-4295-2018

Wondzell, S. M., Gooseff, M. N., & McGlynn, B. L. (2007). Flow velocity and the hydrologic behavior of streams during baseflow. *Geophysical Research Letters*, *34*(24), 63–66. https://doi.org/10.1029/2007gl031256

Wu, X., Zhou, J., Yu, H., Liu, D., Xie, K., Chen, Y., Hu, J., Sun, H., & Xing, F. (2021). The Development of a Hybrid Wavelet-ARIMA-LSTM Model for Precipitation Amounts and Drought Analysis. *Atmosphere*, *12*(1), Article 1. https://doi.org/10.3390/atmos12010074

Xia, L., Bi, R., Song, X., Hu, W., Lyu, C., Xi, X., & Li, H. (2022). Soil moisture response to land use and topography across a semi-arid watershed: Implications for vegetation restoration on the Chinese Loess Plateau. *Journal of Mountain Science*, *19*(1), 103–120. https://doi.org/10.1007/s11629-021-6830-3

Xiang, W., Rong, X., Yan, W., Qi, X., Wang, H., Jin, S., & Ai, J. (2022). Spatial Representativeness of Eddy Covariance Measurements in a Coniferous Plantation Mixed with Cropland in Southeastern China. *Remote Sensing*, *14*(19), Article 19. https://doi.org/10.3390/rs14195022

Xiao, C., Yuan, W., & Yu, R. (2018). Diurnal cycle of rainfall in amount, frequency, intensity, duration, and the seasonality over the UK. *International Journal of Climatology*, *38*(13), 4967–4978. https://doi.org/10.1002/joc.5790

Yan, J., Laflamme, S., Singh, P., Sadhu, A., & Dodson, J. (2020). A Comparison of Time-Frequency Methods for Real-Time Application to High-Rate Dynamic Systems. *Vibration*, *3*(3), Article 3. https://doi.org/10.3390/vibration3030016

Yarami, N., Kamgar-Haghighi, A. A., Sepaskhah, A. R., & Zand-Parsa, Sh. (2011). Determination of the potential evapotranspiration and crop coefficient for saffron using a water-balance lysimeter. *Archives of Agronomy and Soil Science*, *57*(7), 727–740. https://doi.org/10.1080/03650340.2010.485985

Yong, S. L. S., Ng, J. L., Huang, Y. F., & Ang, C. K. (2023). Estimation of Reference Crop Evapotranspiration with Three Different Machine Learning Models and Limited Meteorological Variables. *Agronomy*, *13*(4), 1048. https://doi.org/10.3390/agronomy13041048

Zeshang Yang, Kallergi, M., DeVore, R. A., Lucier, B. J., Wei Qian, Clark, R. A., & Clarke, L. P. (1995). Effect of wavelet bases on compressing digital mammograms. *IEEE Engineering in Medicine and Biology Magazine*, *14*(5), 570–577. https://doi.org/10.1109/51.464773

Zhang, A., Zheng, C., Wang, S., & Yao, Y. (2015). Analysis of streamflow variations in the Heihe River Basin, northwest China: Trends, abrupt changes, driving factors and ecological influences. *Journal of Hydrology: Regional Studies*, *3*, 106–124. https://doi.org/10.1016/j.ejrh.2014.10.005

Zhang, J., Dai, Q., Nanding, N., & Han, D. (2022). Exploring the effect of catchment morphology on streamflow characteristics with virtual experiments. *Journal of Hydrology*, *608*, 127606. https://doi.org/10.1016/j.jhydrol.2022.127606

Zhang, T., Liu, Y., Yang, X., & Wang, X. (2018). An analysis of effect of land use change on river flow variability. *IOP Conference Series: Earth and Environmental Science*, *121*, 052044. https://doi.org/10.1088/1755-1315/121/5/052044